

INFORMATION TO USERS

This manuscript has been reproduced from the microfilm master. UMI films the text directly from the original or copy submitted. Thus, some thesis and dissertation copies are in typewriter face, while others may be from any type of computer printer.

The quality of this reproduction is dependent upon the quality of the copy submitted. Broken or indistinct print, colored or poor quality illustrations and photographs, print bleedthrough, substandard margins, and improper alignment can adversely affect reproduction.

In the unlikely event that the author did not send UMI a complete manuscript and there are missing pages, these will be noted. Also, if unauthorized copyright material had to be removed, a note will indicate the deletion.

Oversize materials (e.g., maps, drawings, charts) are reproduced by sectioning the original, beginning at the upper left-hand corner and continuing from left to right in equal sections with small overlaps. Each original is also photographed in one exposure and is included in reduced form at the back of the book.

Photographs included in the original manuscript have been reproduced xerographically in this copy. Higher quality 6" x 9" black and white photographic prints are available for any photographs or illustrations appearing in this copy for an additional charge. Contact UMI directly to order.

UMI

**A Bell & Howell Information Company
300 North Zeeb Road, Ann Arbor MI 48106-1346 USA
313/761-4700 800/521-0600**

**A THERMAL-INFRARED AND MILLIMETER-WAVE STUDY OF EVOLVED
STARS, AND PROTO-PLANETARY AND PLANETARY NEBULAE**

by
Aditya Dayal

**A Dissertation Submitted to the Faculty of the
DEPARTMENT OF ASTRONOMY
In Partial Fulfillment of the Requirements
For the Degree of
DOCTOR OF PHILOSOPHY
In the Graduate College
THE UNIVERSITY OF ARIZONA**

1 9 9 7

UMI Number: 9806768

UMI Microform 9806768
Copyright 1997, by UMI Company. All rights reserved.

**This microform edition is protected against unauthorized
copying under Title 17, United States Code.**

UMI
300 North Zeeb Road
Ann Arbor, MI 48103

THE UNIVERSITY OF ARIZONA ®
GRADUATE COLLEGE

As members of the Final Examination Committee, we certify that we have
read the dissertation prepared by Aditya Dayal

entitled A Thermal-Infrared and Millimeter-Wave Study of Evolved
Stars, and Proto-Planetary and Planetary Nebulae

and recommend that it be accepted as fulfilling the dissertation
requirement for the Degree of Doctor of Philosophy

<u>John H. Bieging</u>	<u>6/23/97</u>
Dr. John H. Bieging	Date
<u>William F. Hoffmann</u>	<u>6/23/97</u>
Dr. William F. Hoffmann	Date
<u>Christopher K. Walker</u>	<u>6/23/97</u>
Dr. Christopher K. Walker	Date
<u>George H. Rieke</u>	<u>6/23/97</u>
Dr. George H. Rieke	Date
_____	Date

Final approval and acceptance of this dissertation is contingent upon
the candidate's submission of the final copy of the dissertation to the
Graduate College.

I hereby certify that I have read this dissertation prepared under my
direction and recommend that it be accepted as fulfilling the dissertation
requirement.

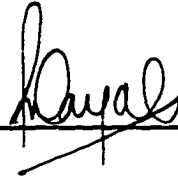
<u>John H. Bieging</u>	<u>6/23/97</u>
Dissertation Director	Date
Dr. John H. Bieging	

STATEMENT BY AUTHOR

This dissertation has been submitted in partial fulfillment of requirements for an advanced degree at The University of Arizona and is deposited in the University Library to be made available to borrowers under rules of the Library.

Brief quotations from this dissertation are allowable without special permission, provided that accurate acknowledgment of source is made. Requests for permission for extended quotation from or reproduction of this manuscript in whole or in part may be granted by the head of the major department or the Dean of the Graduate College when in his or her judgment the proposed use of the material is in the interests of scholarship. In all other instances, however, permission must be obtained from the author.

SIGNED: _____

A handwritten signature in cursive script, appearing to read 'Kaval', is written over a horizontal line.

ACKNOWLEDGMENTS

In looking back at my tenure as a graduate student at Steward Observatory I realize that I owe much to many people.

I would like to express my sincere gratitude to my advisors, John Bieging and Bill Hoffmann, for their ideas and expert guidance during this study. Bill Hoffmann was my thermal-IR advisor: from him I learnt the fundamentals of mid-IR astronomy and as well as the value of hands-on instrumentation work. His scientific insights and critical analyses were invaluable in improving the quality of my work and in setting higher standards for myself. John Bieging introduced me to the fundamentals of radio astronomy. His patience in explaining the basics of aperture synthesis imaging during my second year at Steward, was an important factor that led me to include millimeter studies in my dissertation. John instilled in me the importance of looking at scientific problems with a broad perspective – in terms of the “big picture”. He provided just the right mix of “steering”, and encouragement that I needed from an advisor. I don’t believe that I could have had a better set of advisors than John and Bill.

Fellow members of the MIRAC team and my friends and colleagues, Lynne Deutsch and Joe Hora, were always on hand to answer questions and discuss Mid-IR issues. Special thanks to Lynne for “listening” to my grad school woes and to Joe for writing some very useful MIRAC data reduction programs which I used during my work. Thanks also to Margaret Meixner and Chris Skinner for useful discussions at various times during the past few years, and also for the remote use of Margaret’s Sparc Station to run the dust radiative transfer code. I also thank Murray Campbell and Steve Beckwith for giving me research opportunities early on as an undergraduate, and for inspiring me to get my PhD. in astronomy.

I thank the present and past graduate students for their help and companionship during the past few years, and the faculty and staff for making Steward an enjoyable place to work in. Life in graduate school would not have been the same without the games of tennis and the camping and hiking opportunities that Southern Arizona had to offer. Thanks to all my tennis and squash partners for providing a much needed diversion.

My family was always behind me, throughout this program and it was a tremendous help and encouragement just to know that. I would like to convey a very special Thank You to my wife and best friend Shaheen, for all her support and understanding. I could not have spent such a long time working so hard, without her by my side.

DEDICATION

Dedicated to my parents Prakash and Beena Dayal, and my brother Vikram for their untiring support and encouragement of my studies, and for instilling in me the belief that *nothing* is unattainable.

TABLE OF CONTENTS

	LIST OF FIGURES	8
	LIST OF TABLES	10
	ABSTRACT	11
1	Introduction	13
1.1	Structure and Evolution on the Asymptotic Giant Branch	13
1.2	Mass Loss	16
1.3	Outline of this study	18
2	Millimeter-Wave Spectroscopic Imaging	20
2.1	Overview	20
2.2	Introduction	21
2.3	Modeling of Molecular Lines	26
2.4	A Study of IRC+10216	30
2.5	Detailed study of IRAS 22272+5435 and AFGL 2343	35
2.5.1	Overview of this study	35
2.5.2	Millimeter-wave interferometry: background	35
2.5.3	Observations and Data Reduction	36
2.5.4	Results and Analyses	42
2.6	Single-dish spectroscopy/mapping	58
2.7	Summary of Chapter 2	69
3	Mid-Infrared Imaging of Warm Dust emission	71
3.1	Overview	71
3.2	Introduction	72
3.3	The MIRAC2 Mid-Infrared Camera	75

3.3.1	Detector – A general description	75
3.3.2	Preamplifier	78
3.3.3	Optics	80
3.4	Imaging and Data Reduction	83
3.4.1	Imaging	83
3.4.2	Data Reduction and Calibration	86
3.4.3	Thermal background emission	91
3.5	Analysis and Modeling	93
3.5.1	Temperature, Optical Depth and Feature Maps	93
3.5.2	Geometrical Modeling	95
3.6	Results	99
3.6.1	IRAS 22272+5435 and IRAS 07134+1005	100
3.6.2	M 4-18	101
3.6.3	IC 5117	107
3.6.4	OH 231.8+4.2	116
3.7	Summary of Chapter 3	127
4	Conclusions	129
4.1	Summary of Results	129
4.2	Future Work	134
	REFERENCES	136

LIST OF FIGURES

1.1	Evolution on the H-R diagram	15
2.1	AGB star caricature	24
2.2	Geometry of HCN hyperfine components	28
2.3	Aperture synthesis images of HCN and CN	32
2.4	OVRO <i>UV</i> coverage for IRAS 22272+5435	38
2.5	OVRO <i>UV</i> coverage for AFGL 2343	38
2.6	CO J=1-0 spectrum towards AFGL 2343	41
2.7	CO J=1-0 spectrum towards IRAS 22272+5435	42
2.8	Contour maps of CO emission towards IRAS 22272	44
2.9	CO contour maps towards AFGL 2343	45
2.10	CO spectrum towards center of IRAS 22272+5435	46
2.11	IRAS 22272 model spectra and radial profile fits	49
2.12	CO spectrum towards center of AFGL 2343	51
2.13	AFGL 2343 position velocity diagrams	53
2.14	AFGL 2343 model spectra and radial profile fits	54
2.15	Model CO J=2-1 spectra	57
2.16	12-meter spectra: IRAS 04296 and IRAS 07134	61
2.17	12-meter spectra: HD 161796	62
2.18	CO spectra towards IRAS 06562-0337 and NGC 6302	65
2.19	CO spectra towards Hb12 and Vy2-2	66
2.20	CO spectra towards M 1-78 and M 2-43	67
3.1	Cross-section of a BIB array	77
3.2	Array multiplexer readout scheme	79
3.3	MIRAC2 array output voltage	81

3.4	MIRAC2 cryostat and optical path	82
3.5	Atmospheric transmission in the Mid-IR	84
3.6	Chop-Nod data taking mode	87
3.7	Unprocessed MIRAC2 image	88
3.8	Axially symmetric model schematic	97
3.9	IRAS Low Res. Spectrum of M 4-18	102
3.10	M 4-18 Mid-IR images (8-13 μ m)	104
3.11	Radio continuum map of M 4-18	105
3.12	Deconvolved mid-IR image of M 4-18	106
3.13	IRAS Low Res. Spectrum of IC 5117	107
3.14	IC 5117 mid-IR images (8-13 μ m)	109
3.15	IC 5117 mid-IR images (17-20 μ m)	110
3.16	Radio continuum map IC 5117	111
3.17	IC 5117 Temperature and Optical Depth	113
3.18	IC 5117 feature emission	115
3.19	IRAS Low Res. Spectrum of OH 231.8	118
3.20	Mid-IR spectrum OH 231.8	118
3.21	OH 231.8+4.2 mid-IR images (8-12 μ m)	119
3.22	OH 231.8+4.2 mid-IR images (18-21 μ m)	120
3.23	OH 231.8: near-IR and CO images	121
3.24	OH 231.8+4.2 color temperature maps	124
3.25	OH 231.8+4.2 Silicate emission (9.8 μ m)	125

LIST OF TABLES

2.1	Summary of OVRO observations	39
2.2	Summary of millimeter-wave statistical equilibrium models	56
2.3	Summary of 12-meter CO observations	68
3.1	Detector Characteristics	77
3.2	Summary of MIRAC2 observations	126

ABSTRACT

The evolution of low- and intermediate-mass stars ($1M_{\odot}$ – $8M_{\odot}$) from the Asymptotic Giant Branch (AGB) to the Planetary Nebula (PN) phase is a poorly understood phase of stellar evolution.

We have observed a sample of AGB stars, Proto-Planetary and Planetary Nebulae (PPNe and PNe) at thermal- (or mid-) infrared and millimeter wavelengths. The thermal-infrared emission comes from the warm dust ($T_{\text{dust}} \approx 100\text{--}300$ K) circumstellar shells. Images at these wavelengths provide a unique “close-up” look at the morphology of these sources, and therefore allow us to constrain the geometry and/or mass loss rates on short dynamical timescales. The millimeter-wave observations probe the extended circumstellar molecular envelopes; therefore they provide valuable spatial and kinematical information on the larger scales (and over longer dynamical timescales) than the mid-IR images.

Our results show that the dust shells of all the planetary and proto-planetary nebulae (PPNe and PNe) in our study are not spherical; those that are well-resolved appear to be bipolar and can be modeled with axially symmetric models. These results strongly suggest that the evolution from AGB to PN is often accompanied by higher mass loss rates in the equatorial plane than in the polar regions, as predicted by binary star (common envelope) evolution models, or models involving stellar rotation. At least one bipolar nebula (M 4–18) appears to be a single, low-mass star. From our mid-IR images at feature wavelengths we find that the spatial distribution of the carbonaceous and silicate grains varies over the surface of the nebulae. IC 5117 shows evidence for stratification of carbon- and oxygen-based grains and suggests that some PNe go through temporal changes in

circumstellar chemistry (from oxygen-rich to carbon-rich) as they evolve off the AGB. The molecular envelopes of the sources in our study can be modeled with spherically symmetric models though two sources (IRC+10216 and AFGL 2343) show kinematical and spatial evidence for departures from spherical symmetry. Our millimeter observations of IRC+10216 also provide confirmation that the interstellar UV photons initiate a variety of photochemical reactions in circumstellar envelopes of AGB stars and PNe.

CHAPTER 1

INTRODUCTION

1.1. Structure and Evolution on the Asymptotic Giant Branch

The evolution of a star is determined primarily by the interplay between gravity, which tends to compress/collapse the star and thermal pressure which tends to expand the star. The vast majority of stars like the Sun spend most of their lifetime (or about 5 Gyr) quiescently burning hydrogen to helium in their cores. During this phase (called the main-sequence) the energy generated by thermonuclear burning of hydrogen provides the internal thermal pressure which exactly counter-balances the gravitational force of the star. When the hydrogen in the core is exhausted, the core contracts under gravitational pressure, and begins to get hotter. Hydrogen continues to burn in a shell around the inert He core. The heating-up of the core accelerates hydrogen shell burning; the thermal pressure thus generated, causes a rapid expansion of the outer layers of the star. The star now enters the Red Giant phase, where it is characterized by a high luminosity ($\sim 10^3 L_{\odot}$), low temperature (~ 3000 K) and a large convective envelope with radius of about 100

R_{\odot} . Meanwhile the core, which has been compressed to the point of degeneracy, continues to contract and heat up until the temperature reaches $\sim 10^8$ K. At this point the core He is ignited violently via the triple- α process, the condition of degeneracy is lifted and He begins to burn quiescently into carbon and oxygen in the core. After about 10^6 yr the core He is exhausted.

Low and intermediate mass stars ($1-8 M_{\odot}$) ascend the asymptotic giant branch (AGB) after hydrogen and helium in their core is exhausted. During this evolutionary phase, the star has an electron degenerate carbon-oxygen core surrounded by thin, concentric shells of helium and hydrogen (the “nuclear-active” zone), a convective outer layer and a large distended circumstellar envelope (CSE). The hydrogen and helium shells burn alternately; long periods of quiescent hydrogen burning are interrupted by violent helium flashes which initiate an expansion of the circumstellar envelope (Iben 1990; Iben and Renzini 1983). During this phase the star is said to be in a thermal pulsing phase and usually displays periodic variations in its size (radius) and surface luminosity. AGB stars have high bolometric luminosities ($\sim 10^4 L_{\odot}$), cool (~ 3000 K), distended ($\sim 10^2-10^3 R_{\odot}$) photospheres and large circumstellar envelopes (CSEs), which harbour a wide variety of molecular species and dust grains.

AGB stars lose their envelope mass at a high rate ($10^{-4}-10^{-7} M_{\odot}\text{yr}^{-1}$) in the form of a cool, low velocity ($\sim 5-20$ km s $^{-1}$) wind. This mass loss rate increases steadily as the star ascends the AGB and leads to a gradual obscuration of the central star at optical wavelengths. Eventually, as the star nears the tip of the AGB the mass loss rate may increase to $\geq 10^{-4} M_{\odot} \text{ yr}^{-1}$; this intensive but short-lived period of mass loss, also called the “superwind” (Iben and Renzini 1983), results in the expulsion of the AGB envelope. Though the mechanism of the mass loss

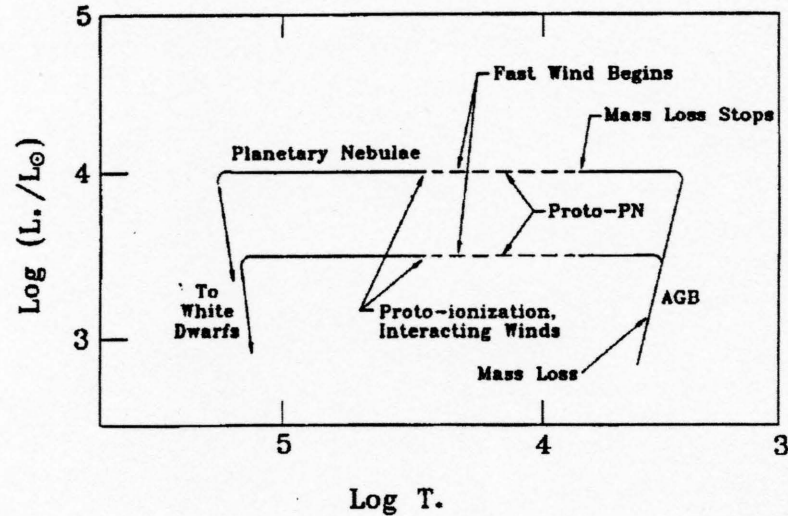


Figure 1.1 The evolutionary tracks of two intermediate mass stars (of different core masses) on the H-R diagram, as they evolve from the AGB, through the PPN and PN phase to eventually become white dwarfs (Kwok 1993).

process is poorly understood, it is generally believed that radiation pressure on dust grains, coupled with radial pulsations which levitate the atmosphere, are the principal drivers of mass loss (Vassiliadis and Wood 1993; Bedijn 1987). When a significant portion of the outer layers of the star have been ejected there is a decrease in the mass loss rate; yet the photospheric temperature of the central star is still not high enough to ionize the circumstellar nebula. During this short period ($\sim 10^3$ yr), prior to the onset of ionization, the circumstellar shell appears detached from the stellar photosphere and the source is called a Proto-Planetary Nebula (PPN). The spectral energy distributions of Proto-Planetary Nebulae (PPNe) are usually double-peaked: a peak in the optical/UV, corresponding to emission from the central star, and a peak in the mid-IR due to thermal emission from the detached dust shell (e.g. Kwok 1993). As the CSE continues to expand and move outwards, the central star that was originally the core of the AGB star

begins to get exposed. UV photons from the star ionize the circumstellar nebula and a hot, fast ($V_e \sim 2,000 \text{ km s}^{-1}$) wind with a significantly lower mass loss rate ($\sim 10^{-8} M_{\odot} \text{ yr}^{-1}$) now turns on. The star moves horizontally across the H-R diagram maintaining a constant luminosity, getting hotter as it continues to contract. When the surface temperature of the star reaches $\sim 30,000 \text{ K}$ the stellar radiation ionizes the nebula around it; the circumstellar nebula now shines brightly at optical wavelengths, particularly in recombination lines (hydrogen, helium) and forbidden lines (nitrogen, oxygen, sulphur), and is now a Planetary Nebula (PN). In some low-mass stars (e.g. high latitude “supergiants”; Kwok, Volk and Hrivnak 1989, Parthasarathy and Pottasch 1986) which appear to show spectral characteristics of PPNe, the nebula may disperse prior to the onset of ionization; since such stars may never become PNe, they are often referred to as post-AGB stars. As the circumstellar nebula continues to expand the dust and gas emission (surface brightness) decreases rapidly due to decreasing temperature and densities, and the nebula merges into the interstellar medium in about 10^4 yr . Now the White Dwarf central star is left behind; with no source of energy it slowly begins to cool down and fades away into the darkness of interstellar space.

1.2. Mass Loss

Ground-based optical, infrared and radio continuum imaging surveys (which trace scattered starlight, dust emission and ionized gas respectively) of Planetary Nebulae (PNe) have shown that a majority ($\geq 80\%$) of PNe are non-spherical (e.g. Corradi and Schwarz 1995; Latter et al. 1995; Aaquist and Kwok 1991; Balick 1987; Zuckerman and Aller 1986). Many are elliptical, bipolar, “butterfly-shaped” and many also show multiple shells or rings and jets. These findings have been amply

confirmed by high resolution HST/WFPC2 (Hubble Space Telescope/Wide-Field Planetary Camera2) observations (Bond et al. 1996; Sahai and Trauger 1996). While the morphological classifications differ somewhat from one study to another, it is clear that the observed shapes of PNe are not consistent with uniform, spherically symmetric expansion from the AGB to the PNe. Some sources can be modeled with axially symmetric structures, while the images of others warrant even more complicated “point-symmetric” models. One of the most successful theories proposed to explain the shapes of PNe has been the Interacting Stellar Winds model (ISW; Icke, Balick and Frank 1992; Soker and Livio 1989; Kahn and West 1985; Kwok, Purton and Fitzgerald 1978). In these models, the PN is shaped by shocks associated with the fast wind, as it ploughs into the slower, higher density AGB wind. ISW models can account for a variety of observed PNe morphologies *if* there is asymmetric mass loss during the AGB phase. These hydrodynamical models show that an equatorial density enhancement (due to preferential mass loss in the equatorial plane) in the AGB wind can create shock fronts with spheroidal, elliptical or “figure-8” shapes. These shapes, together with orientation in the sky, are very effective in explaining the observed morphologies of PNe; however, they do not account for the origin of the asymmetry in the AGB winds. The asymmetry during the AGB phase ($\frac{\dot{M}_{eq}}{\dot{M}_{pole}} > 1$) can be explained via models which invoke mass loss in rotating stars (e.g. Dorfi and Höfner 1996; Livio 1994), binary stars (e.g. Rasio and Livio 1996; Han, Podsiadlowski and Eggleton 1995; Iben and Livio 1993), or constraining of material by magnetic fields (e.g. Chevalier 1994). So far, few PPNe and young PNe have been mapped at mid-IR wavelengths (Meixner et al. 1997, Hora et al. 1996, Hawkins et al. 1995, Skinner et al. 1994); these studies, which probe the morphology of the dust shells on small spatial scales, indicate that most sources exhibit some kind of axial symmetry and provide further evidence

that the mass loss process is inherently asymmetric. They support the idea that deviations from spherical symmetry may appear on or shortly after the star leaves the AGB.

The details of the mass loss process in AGB stars, which have strong implications for stellar evolutionary models, are not very well understood. However, since the structure and morphologies of PPNe and PNe are directly related to the mass loss process, we address some of the following outstanding questions about the mass loss mechanism, by conducting a multiwavelength, millimeter-wave and thermal-IR imaging study of these sources: *(a)* Is the mass loss process spherically symmetric at any point in the evolution from an AGB star to the PN stage? If not, what are the simplest axially symmetric structures that can reproduce the observed morphologies of PPNe and young PNe? *(b)* Does the shape and structure of the warm dust shell resemble that of the molecular envelope? Are the observed shapes consistent with the kinematical structure of the envelopes as inferred from mm-interferometry? *(c)* Do the mid-IR spectral emitters form a distinct population of dust grains separate from the continuum emitters? If so, can their spatial distribution (or excitation) be related to the evolutionary stage of the objects?

1.3. Outline of this study

To answer the above questions we have conducted a study of molecular gas and dust (the primary constituents) in a group of AGB stars, PPNe and young PNe at millimeter and thermal-infrared wavelengths. (In this study thermal-IR and mid-IR are used interchangeably and refer to the wavelength region 5–25 μ m.) The millimeter-wave observations probe emission from molecules via their rotational

lines while the thermal-IR images sample emission from the warm dust shells ($T_{dust} \sim 200\text{K}$) that surround the central star. In Chapter 2 of this study we present millimeter-wave (interferometer and single-dish) observations of a variety of sources, in transition from the AGB to the PN stage. The interferometer observations provide maps of molecular emission at a high spatial ($\theta \sim 5''$) and spectral ($\Delta V \sim 1\text{km s}^{-1}$) resolution. From these observations we are able to infer abundances and physical conditions in the CSEs, using our statistical equilibrium/radiative transfer codes. In Chapter 3, we present mid-IR images of warm dust emission from PPNe and young PNe. These observations are for the most part diffraction limited, ($\theta_d \sim 1\text{--}1.5''$) and provide images of the source morphology on small spatial scales. From our mid-IR observations we also infer the spatial distribution (and abundances) of mid-IR emission line carriers. In Chapter 4 we present a summary of our results and our conclusions.

CHAPTER 2

MILLIMETER–WAVE SPECTROSCOPIC IMAGING

2.1. Overview

In this chapter we present millimeter–wave, single–dish and inteferometer observations of molecular lines in an AGB star (IRC+10216), and a sample of PPNe and young PNe. Our objectives are to: (1) infer abundances and physical conditions (kinetic temperature, density, mass loss rate) in these sources by modeling our observations and (2) to determine the geometrical and kinematical structure of these molecular shells at high spatial– ($\sim 5''$) and spectral– ($\sim 1\text{km s}^{-1}$) resolution and relate these to morphologies seen at other wavelengths, particularly in the mid–IR.

This chapter is divided into the following sections:

Section 2.2 – An introduction to the molecular envelopes of AGB stars.

Section 2.3 – A description of the codes and method of analysis used in

modeling the sources.

Section 2.4 – A study of the abundances of HCN, H^{13}CN , CN and C_4H and the physical structure of the well-known carbon-rich AGB star, IRC+10216, conducted with the BIMA mm-interferometer. Dayal and Bieging (1993, 1995) are papers that came out of this study and are therefore directly related to this section.

Section 2.5 – Interferometry and modeling of CO emission from two PPNe, AFGL 2343 and IRAS 22272+5435, with the OVRO interferometer.

Section 2.6 – Spectroscopy and mapping of CO towards a variety of post-AGB objects, PPNe and PNe, with the NRAO¹ 12-meter telescope. Dayal and Bieging (1996) is a paper directly related to this study.

Section 2.7 – A summary of the main results in Chapter 2.

2.2. Introduction

The evolution of a star along (and following) the Asymptotic Giant Branch (AGB) is determined by mass loss from the surface of the star. During this phase mass loss rates (10^{-7} – $10^{-4} M_{\odot} \text{ yr}^{-1}$) exceed nuclear burning rates in the core ($10^{-7} M_{\odot} \text{ yr}^{-1}$) and therefore the mass loss determines evolutionary timescales (Schönberner 1989, Iben and Renzini 1983). Since the mechanisms, rates and the geometry of mass loss processes are poorly understood (and often described in empirical terms), we are faced with the problem of a fundamentally incomplete

¹The National Radio Astronomy Observatory is operated by Associated Universities, Inc., under a cooperative agreement with the National Science Foundation.

understanding of the formation of proto-planetary and planetary nebulae (PPNe and PNe). Our millimeter-wave studies presented here, based on high spatial and spectral resolution observations, seek to provide a better understanding of the kinematics and spatial distribution of the gas and of the mass loss process.

AGB stars have high bolometric luminosities ($\sim 10^4 L_{\odot}$), cool (~ 3000 K), distended ($\sim 10^2$ – $10^3 R_{\odot}$) photospheres and large circumstellar envelopes (CSEs), which are predominantly molecular in composition (e.g. see recent reviews by Glassgold 1996, Habing 1996; Knapp et al. 1982; Morris 1975). Though the outer boundary of the CSE is determined observationally by the spatial extent of molecular emission lines (typically 10^{17} cm), the inner boundary is not well defined. For modeling purposes the inner radius is assumed to be a factor of 10–100 times larger ($\sim 10^{15}$ cm) than the photospheric radius. (10^{15} cm corresponds to an angular size of $\sim 1''$ at a distance of 100 pc, and is near the resolution limit of modern mm-interferometers). Millimeter-wave line observations trace rotational energy transitions of molecules though H_2 , the most abundant molecule, has no permanent dipole moment and it is not directly observable in electric dipole rotational transitions. H_2 is directly observed in near-infrared (near-IR) vibrational bands but these transitions probe hotter gas ($E/k \sim 1000$ K) and have more uncertain excitation mechanisms. CO, the most abundant molecule after H_2 , is a very good tracer of the molecular envelope for a number of reasons. Unlike molecules like HCN, which are more easily photodissociated, CO is relatively abundant at large radii because of self-shielding from the interstellar UV radiation field (Morris and Jura 1983). Since the lowest rotational transition of CO ($J=1-0$) traces the low kinetic temperatures ($E/k \approx 5$ K), CO observations effectively probe the *entire* CSE. CO also has a relatively small dipole moment therefore a low transition probability (Einstein A coefficient); thus its level populations (and

the excitation temperature) are determined primarily by collisional excitation with H_2 , particularly at large optical depths. Observations of CO, therefore, allow us to constrain the kinetic temperature quite strongly.

The nature of the mass loss process in evolved stars is very intricately tied to the chemistry of their circumstellar envelopes. The cool, low-velocity winds emanating from evolved stars are very conducive for the formation of molecules and dust grains. Since the winds are at least partially driven by radiation pressure on dust grains (Knapp 1986), dust grain formation can affect the mass loss rates, particularly in the inner regions of the CSEs. The winds determine the density of material in the envelopes, and therefore also play a vital role in determining the spatial extent of molecules and atoms. Winds also establish dynamical timescales, which, together with chemical timescales, govern the nature of the chemical reactions in the envelopes. Elemental abundances in the cool winds reflect photospheric abundances at the time the material was ejected; these abundances are, in turn, related to the history of nucleosynthesis and subsequent dredge-up processes.

In the simplest models of CSE chemistry the chemical composition of the envelope is determined chiefly by the C and O abundances at the photosphere. At the photosphere, high densities ensure that the chemical reaction timescales (τ_r) are significantly lower than dynamical timescales (timescales for change in density by a significant amount, τ_d). In this regime, most reactions proceed to completion, and the chemistry is determined under conditions of local thermodynamic equilibrium (LTE; Lafont et al. 1982; Huggins and Glassgold 1982; Tsuji 1973). In carbon stars ($\text{C/O} > 1$) most of the oxygen is tied up in CO. The excess carbon goes into forming other stable molecules such as HCN and C_2H_2 . Therefore strong detections

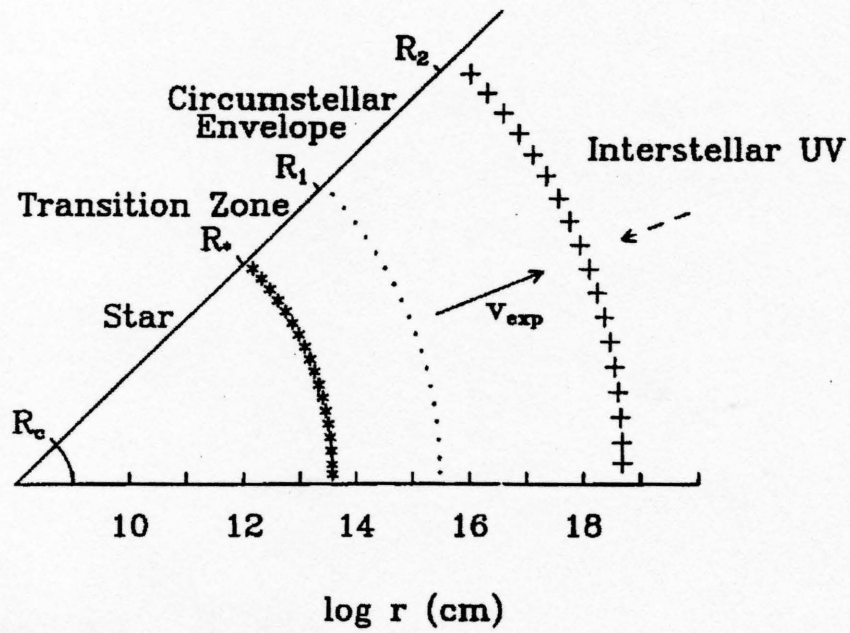


Figure 2.1 A schematic cross-sectional view of an AGB star. R_c is the radius of the core, R_* the dust photospheric radius and R_1 , R_2 mark the inner and outer radii of the circumstellar envelope (Glassgold 1996).

of HCN and C_2H_2 are usually associated with carbon-rich CSEs. In M stars ($C/O < 1$), most of the carbon goes into forming CO. The excess oxygen is used up in H_2O and SiO. Conditions of LTE prevail further out into the CSE until a point where the dynamical timescales become shorter than the reaction timescales. At this point the molecular abundances “freeze out”; i.e. the chemical composition of the wind established near the photosphere is not altered further (except by other processes, which I discuss below). Since the chemical timescales depend strongly on the abundances and other physical conditions, various species will freeze out at different radii. Though LTE chemistry models are adequate to explain the observed abundances of the most stable molecules near the photosphere, they are unable to explain the large abundance of complex organic molecules such as cyanopolyynes, (HC_xN ; Truong-Bach et al. 1996; Bieging and Tafalla 1993) further out in the CSE of evolved stars and Proto-Planetary Nebulae. At large radii ($\geq 10^{16}$ cm) the circumstellar envelope becomes optically thin to the interstellar radiation field. Stable molecules produced near the photosphere are exposed to the interstellar UV field and to energetic cosmic rays. Photodissociation of these molecules by the interstellar radiation leads to the creation of highly reactive ions and radicals and the rapid initiation of ion-molecule and neutral-radical reactions (e.g. Cherchneff et al. 1993; Howe and Millar 1990; Nejad and Millar 1987), which drastically alter the chemical composition of the wind. For example, CN and C_2H , products of photodissociation of HCN and C_2H_2 , are very important in synthesizing long carbon-chain molecules.

In simple terms, photochemical model calculations employ a network of coupled continuity equation, each of which describes the radial (or temporal) rate of change of abundance ($X(s)$) of a species (s) in terms of the production ($P(s)$)

and destruction ($D(s)$) rates (Cherchneff et al. 1993):

$$v \frac{dX(s)}{dr} = P(s) - D(s)X(s)$$

The abundances derived by these codes depend on a number of factors including the initial (assumed) photospheric abundances and the production and destruction rates (reaction rates, pathways). In spite of the uncertainties associated with these variables (including uncertainties in dust optical properties, photo-dissociation rates, strength of the interstellar radiation field), photo-chemical models have generally been successful in qualitative and quantitative (order of magnitude) predictions about circumstellar abundances. Since these processes are important in the outer envelopes ($\sim 10^{16}$ – 10^{17} cm, corresponding to $1''$ – $10''$ at a distance of 1.0 kpc) the models can be directly tested with millimeter-wave interferometry.

2.3. Modeling of Molecular Lines

Modeling the physical structure of evolved stars from millimeter-wave observations of molecular rotational transitions, is a two-step process. The first step requires solving the problem of Statistical Equilibrium (SE), which defines a relationship between the physical conditions (kinetic temperature, density, abundances) in the stellar envelope and the distribution of the molecule among its rotational and vibrational energy levels. The second part – the Radiative Transfer (RT) problem, defines the relationship between the energy level populations and the shape/intensity of the observed emission lines. The level populations are determined by solving the SE (for each level i , $\frac{dn_i}{dt} = 0$) equations, including both radiative processes as well as collisional excitation with H_2 molecules. The rates of the radiative processes depend on the intensity of the radiation at the line frequency, which includes not only the radiation field of the central star, but also

includes the local radiation field. Thus, an accurate solution to the statistical equilibrium equations requires information about the line intensities, which are only obtained by integrating the radiative transfer equations. We make a simplifying assumption (the Sobolev approximation) to decouple the statistical equilibrium equations from the radiative transfer equations.

The SE code assumes a source of infrared radiation at the center of a spherically symmetric circumstellar envelope. This source represents the shell of hot dust which surrounds the central star and is responsible for the intense infrared radiation. The observed excitation of rotational energy levels of molecules in the circumstellar envelope is a consequence of collisions with H_2 , as well as absorption of infrared radiation into excited vibrational states followed by the subsequent decay of the molecule back to rotational levels within the ground vibrational state (Morris 1975). Microwave line photons emitted at any point in the expanding envelope see a velocity gradient in all directions except along radial lines towards and away from the star. Thus the photons emitted in any region of the envelope are red-shifted with respect to molecules in other parts of the envelope, and cannot interact with those molecules. Only photons in the immediate vicinity of a molecule can be absorbed. This velocity gradient justifies use of the Sobolev escape probability scheme for the microwave photons (Castor 1970). The program calculates collisional rates for pure rotational transitions in the ground vibrational state, since the spontaneous radiative emission rates here are low enough for collisions to play a role in populating these states. It also calculates the optical depths of the IR ro-vibrational transitions along radial lines to the central IR source. The output of the program consists of the computed level populations, excitation temperature, optical depths and the relative importance of radiative rates to collisional rates, all as a function of the radius.

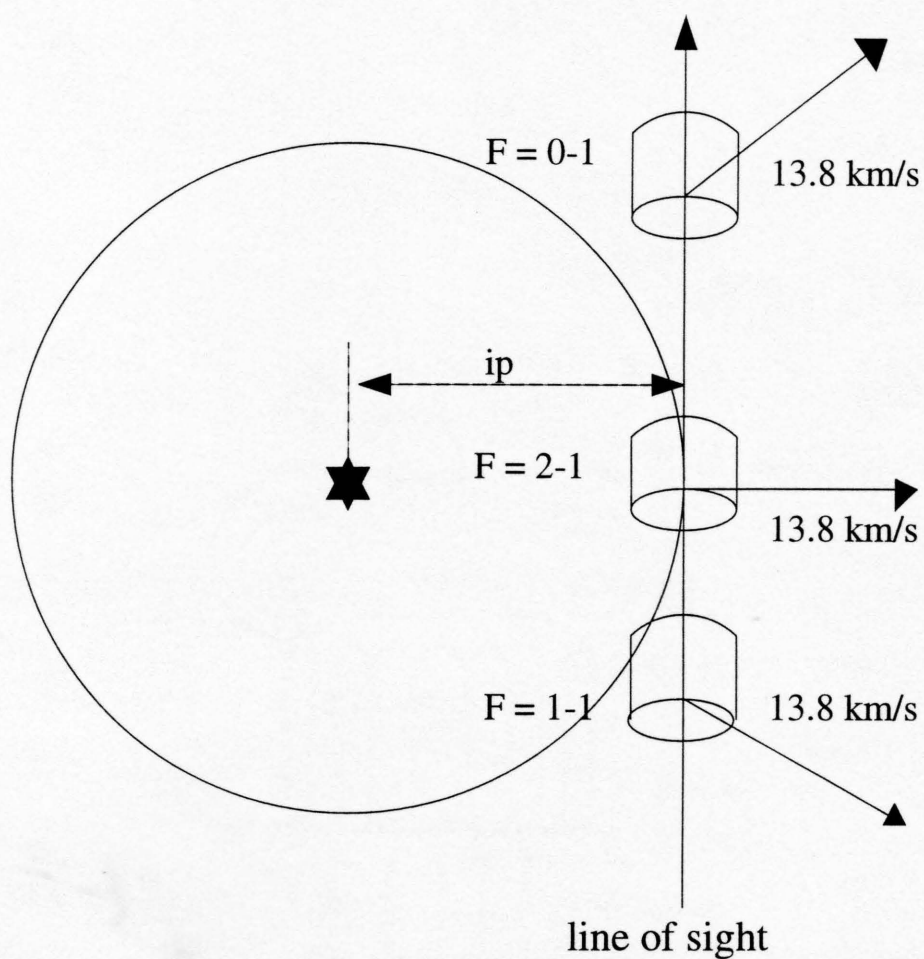


Figure 2.2 A schematic of the radiative interaction between the hyperfine components in the HCN ($J=1-0$) line, for a uniformly expanding CSE. At each impact parameter three volumes of gas emit at the observed frequency which corresponds to the systemic velocity of the star in the central ($F=2-1$) component. (Adapted from Bieging et al. 1984).

Once the excitation of the molecule has been calculated as a function of distance from the star, we integrate the equation of radiative transfer to find the brightness temperature of the emission line as a function of projected radius and radial velocity. The brightness distribution at each velocity is convolved with a gaussian beam to simulate the angular resolution of the observations. From the convolved models, we can extract radial profiles and spectra for comparison with the observations. By successive iterations in the models we can constrain the mass loss rate, expansion velocity, kinetic temperature and abundance of the molecule.

The SE and RT codes I have used for modeling rotational lines were originally written by Bieging and Tafalla (1993). A few small changes were made to the original SE code. The first change allows us to use the level populations from a previous run of the code, as an initial guess to the level populations in the first shell. This simple change is useful in ensuring convergence in the level population calculation, especially in the innermost regions of the envelope where temperature and density change rapidly with radius. The second change allows the user to specify a two-step kinetic temperature gradient in the circumstellar envelope, which is sometimes warranted by observations and approximates theoretical predictions. The radiative transfer code was modified considerably for modeling HCN, H¹³CN and CN, which have hyperfine structure. Since the hyperfine components have frequency separations $\Delta\nu < \nu_0 V/c$, where V is the expansion velocity of the envelope ($\sim 14 \text{ km s}^{-1}$ for the carbon star IRC+10216), along any line of sight there are three (five, for CN) distinct regions that can contribute by emission and absorption of the specific intensity (Figure 2.2). This is because at any observed frequency, emission from the strongest hyperfine component ($F=2-1$) can include blue-shifted emission/absorption from the $F=1-1$ component (which has a lower rest frequency) as well as red-shifted emission from the $F=0-1$ component (which

has a higher rest frequency). To model HCN, H^{13}CN and CN the RT code was re-written to implement this non-local radiative interaction. In this version of the code, emission and/or absorption by the hyperfine components is taken into account explicitly, i.e. as the equation of transfer is integrated along the line of sight at a given frequency and impact parameter, the emission and absorption coefficients are calculated by summing over all the hyperfine levels of the transition. The relative populations of the hyperfine levels, are specified by multiplying their LTE populations by corresponding “departure coefficients”.

Model limitations – Spherically symmetric models, such as those used in our study, have generally been successful in modeling CO emission from evolved stars and PPNe. All the sources to which we apply these models show no *significant* deviations from spherical symmetry. The assumption of any other geometry (e.g. a disk model) would simply introduce more free parameters which are not well constrained. Though our model fits are not necessarily unique, we have explored parameter space by varying the mass loss rate, abundances, and kinetic temperature independently of one another. This process and the implications of our model fits, are described in more detail in specific source modeling sections.

2.4. A Study of IRC+10216

The circumstellar envelope of the carbon star IRC+10216 is the richest known source of molecular species, with ~ 50 species detected thus far (Huggins 1995). This star is also relatively nearby ($d \sim 100\text{--}200\text{pc}$) and well-resolved. Therefore, it provides the strongest observational constraints on CSE photochemical models. During the past few years, the emission from a variety of molecules HCN, CN,

SiS, SiC₂, HC₃N, C₃N, C₄H (Dayal and Bieging 1995; Bieging and Tafalla 1993; Guélin et al. (1993); Dayal and Bieging 1993; Takano et al. 1992) has been spatially resolved with mm-interferometers. These observations have yielded significant constraints on chemical pathways, abundances, photodissociation radii, and condensation radii for the refractory (e.g. Si-bearing) molecules. Most importantly, a number of molecules that have a shell-like distribution have been mapped, leading to a general confirmation of a rich, multi-layered chemistry in CSEs and the importance of the interstellar UV field in modifying the photospheric abundances. In this section we discuss the main results from our observations of IRC+10216 with the BIMA interferometer, and the implications of these data for photochemical models. For a more detailed description of our study, the reader is referred to Dayal and Bieging (1993, 1995).

We observed molecular emission lines of HCN ($J=1-0$ at 88.6 GHz), H¹³CN ($J=1-0$ at 86.3 GHz) and CN ($N=1-0$, $J=3/2-1/2$ at 113.5 GHz) towards IRC+10216. After CO, HCN is the most abundant molecule in carbon-rich AGB stars; CN is also very abundant, with abundances typically $\sim 15-20\%$ that of HCN. The HCN and H¹³CN images both show centrally concentrated distributions and the emission from both molecules falls to zero at a radius of $\sim 30''$. The CN images show a shell distribution, with a peak brightness near a radius of $16''$, and a total radial extent of $\sim 50''$. The spectra of HCN, H¹³CN and CN are rather different due to the differences in their distribution and/or optical depths, but all are complicated by hyperfine structure. We have modeled our observations using the codes described in Section 2.3, to estimate the abundance of HCN and H¹³CN and to infer the kinetic temperature and the mass loss rate in the CSE. For CN we used a simpler, LTE calculation and inferred the abundance assuming optically thin emission. Though our results were qualitatively consistent with photochemical

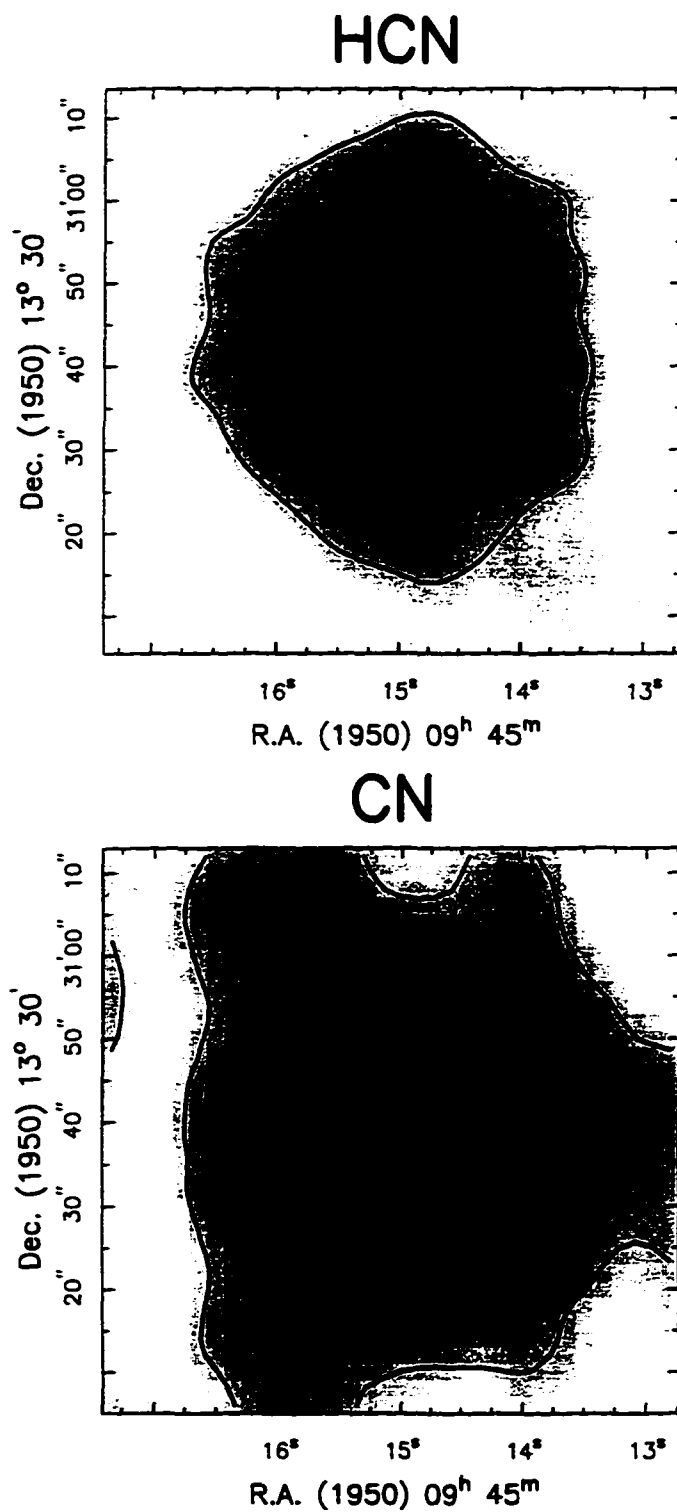


Figure 2.3 HCN and CN emission from IRC+10216 made with the BIMA interferometer. The images illustrate that CN (produced by the photodissociation of HCN) is distributed in a shell, around the centrally concentrated HCN (Dayal and Bieging 1995).

model predictions that CN is formed by the photodissociation of HCN in the outer envelope (e.g. Huggins and Glassgold 1982), they differed significantly from previously published photochemical models in two respects: (1) The size of the CN emission was found to be smaller than that predicted by most models and (2) the CN peak abundance was found to be lower than model estimates. We suggested that these discrepancies could be attributed to various factors including uncertainties in the CN photodissociation rates, or CN reaction pathways. In fact, as shown by Cherchneff and Barker (1992) and Millar and Herbst (1994) previous discrepancies between model predictions and observations of the large abundances of cyanopolynes have been overcome by invoking larger rates for reactions with CN. Recently, Bachiller et al. (1997) have completed a survey of CN in 42 evolved stars and PPNe. They find that lowest CN/HCN ratios are associated with those stars that have higher mass loss rates, while the larger CN/HCN ratios are found in stars with lower mass loss rates. Since the density in the CSE is directly proportional to the mass loss rate, the results of Bachiller et al. (1997) provide further observational confirmation of the model predictions; they also imply that similar photochemical models can be applied to AGB stars as well as PPNe.

Our C₄H observations in the N=9–8 transition (at 85.6 GHz) showed that the molecule lies in a shell with a peak brightness at a radius of $\sim 15''$ (2.3×10^{16} cm for an assumed distance of 100 pc). Using an LTE analysis, we estimated the C₄H abundance (wrt H₂, assuming the H₂ is fully associated) to be $\sim 1.8 \times 10^{-6}$; however, since this calculation assumed a mass loss rate (which defines n_{H_2} , for a constant expansion velocity) and an excitation temperature, there was at least a factor of 2–3 uncertainty in our results. Our observations illustrated that though photochemical models had been able to predict the shell distribution of C₄H, they were unable to account for the large abundance of the molecule.

Shortly after our results were published, Guélin et al. (1993) presented higher spatial resolution and higher sensitivity observations of C_4H (and $MgNC$) with the IRAM Plateau de Bure interferometer. Our results and those of Guélin et al. clearly show that the distribution of C_4H is not smooth, but very clumpy. Though there appears to be no correlation between the azimuthal location of these clumps between our images and theirs, Guélin et al. claim that the clumps represent regions of higher column densities and that the same features/clumps are seen in many other molecules (e.g. $MgNC$, C_3H). The regions of lower densities (or “holes”) appear to be aligned with the major axis of the source (PA 20°) in optical and near-IR images (Dyck et al. (1987); Kastner and Weintraub 1994). Spherically symmetric models have been quite successful in modeling the CSE of IRC+10216 (e.g. this work; Bieging and Tafalla 1993) but there appears to be increasing evidence that the nebula is not spherical, particularly on smaller scales probed by optical and near-IR images. Dyck et al. (1987) show that the asymmetries seen in their speckle interferometry images are consistent with a thick circumstellar envelope with evacuated polar regions (major axis \sim PA 20°), where the photons emitted towards the polar regions have a higher probability of escaping. A similar, but more pronounced, morphology is also seen in a number of PPNe including the classical bipolar PPN, AFGL 2688 (the Egg Nebula; e.g. Latter et al. 1993). Near-IR polarimetric images (Kastner and Weintraub 1994) suggest that the reflection nebula surrounding the central star of IRC+10216 is elongated, also along a PA $\sim 20^\circ$, and that the dust optical depths are highest along the equatorial plane. Thus although there appears to be strong evidence that the dust envelope shows an axially symmetric structure (on spatial scales of $\leq 2''$), the evidence for similar axial symmetry in the molecular envelope is weaker. The distribution of some molecules is consistent with the model inferred from the

dust observations but many other molecules exhibit emission clumps which are rotated with respect to the “equatorial plane” (e.g. SiC₂, CN): still others like HC₃N are more circularly symmetric. The observations of IRC+10216 suggest that non-spherical (or bipolar) structure may be well established *before* a star leaves the AGB to become a PPN/PN.

2.5. Detailed study of IRAS 22272+5435 and AFGL 2343

2.5.1. Overview of this study

We observed IRAS 22272+5435, a carbon-rich proto-planetary nebula (PPN) and AFGL 2343, an oxygen-rich post-AGB (PAGB) object, in the CO J=1-0 line (115.271 GHz) with the Owens Valley Radio Observatory (OVRO) millimeter-interferometer. The interferometer is operated by the California Institute of Technology (Caltech) and is located at Big Pine, California. We have modeled images and spectra of both sources using the statistical equilibrium and radiative transfer codes described previously (Section 2.3), and obtained estimates of the kinetic temperature and the mass loss rates. For this project we collaborated with Per Bergman (formerly at Caltech; now at Onsala Space Observatory, Sweden), who assisted with the data acquisition and calibration.

2.5.2. Millimeter-wave interferometry: background

The diffraction limit of a typical radio telescope ($D \sim 10$ meters) observing in the CO J=1-0 line (λ 2.6 mm) is given by $\theta_d \approx 1.22 \frac{\lambda}{D}$, $\sim 65''$. To obtain spatial resolutions of order $1''$ - $10''$ requires telescopes with considerably larger dish diameters. Interferometers are arrays of (movable) telescopes which achieve resolutions of $1''$ - $10''$ by mimicking large (diameter ~ 100 meter) apertures;

hence the process of imaging is also referred to as aperture-synthesis imaging. Along the essential principles of aperture-synthesis imaging, each baseline (or separation between a pair of antennas) provides a measure of the correlation of the electric field in the radiation emitted by the source (called the spatial coherence function or the complex visibility function; Clark 1988). The antenna spacings are described in UV coordinates; u and v are simply the components of each baseline projected onto a plane normal to the direction to the source. As an interferometer observes a source in the sky, the rotation of the earth causes the u and v components of each baseline to trace out an ellipse (e.g. Figure 2.4); thus the interferometer samples the complex visibility at a large number of points in the UV plane. From the Fourier Transform relationship between the source brightness distribution and the measured complex visibility function (also known as the Van-Cittert-Zernike theorem), the source brightness distribution can be recovered by inverse-transforming the measured visibility function (Thompson, Moran and Swenson 1986). Though the angular resolution of the images ultimately depends on the maximum extent of the sampling in the UV plane, the visibility measurements should be made uniformly over the “aperture”, from the origin to an outer radius. Non-uniform sampling or gaps in the UV plane lead to spatial filtering effects, where brightness information at certain spatial frequencies (which correspond to the size and location of the “hole”) may be lost.

2.5.3. Observations and Data Reduction

The OVRO mm-array consists of six 10.4 m diameter antennas which can be moved to any of several configurations, along a track with an inverted “T” geometry. IRAS 22272+5435 was observed in the Low-Resolution (LR) configuration. AFGL 2343, a lower declination source, was observed in both the Low- and

Equatorial-Resolution (ER) configurations. Since the angular resolution of an interferometer depends on the projected UV coverage, objects at lower declinations ($\delta \leq 40^\circ$) are observed both in the LR configuration, as well as in the larger spacing ER configuration. A summary of the tracks/dates of the OVRO observations is presented in Table 2.1. The UV coverage for both sources is shown in Figures 2.4 and 2.5.

Typical system temperatures (SSB) ranged from 500 K to 700 K during the course of our observations. We used 1749+096 and BL LAC for time-dependent calibrations of the amplitude and phase measurements of AFGL 2343 and IRAS 22272 respectively. Observations were made in approximately 28-minute integration cycles with 22 minutes on the source and 6 minutes on the flux calibrators. The passband calibrations (which correct for frequency or channel dependent correlator gains) were applied from observations of 3 flat-spectrum radio sources: 3C273, 3C454.3 and 3C84. The digital correlator consists of four independent correlator modules which can be run contiguously in series or at independent frequencies in the 1 GHz IF bandpass, with different resolutions. For our observations we used the correlator mode of 3-2-3; this gave us an effective bandwidth of 62 MHz (161 km s^{-1}) and a channel resolution of 0.5 MHz (1.3 km s^{-1}) for IRAS 22272, and a channel resolution of 1 MHz (2.6 km s^{-1}) for AFGL 2343. All the data were calibrated using the *MMA* software package (Scoville et al. 1993). After the UV data were calibrated they were converted to UV-FITS format and transported into MIRIAD (Sault, Teuben and Wright 1995). Detailed information on MIRIAD, the Multichannel Image Reconstruction, Image Analysis, and Display program is available at <http://www.atnf.csr.io.au/ATNF/miriad>.

The visibility datasets were Fourier transformed after natural weighting and

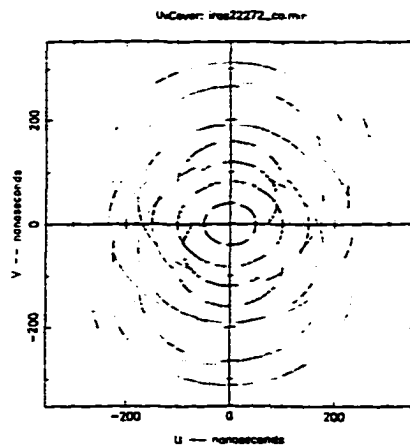


Figure 2.4 *UV* coverage for OVRO observations of IRAS 22272+5435, in the LR configuration. The interferometer samples spatial frequencies in the range 40-330 *lns* (12-100 m).

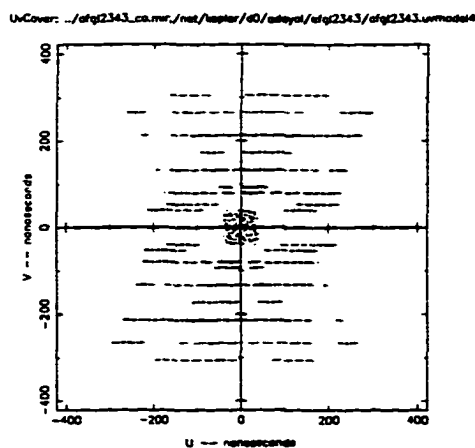


Figure 2.5 *UV* coverage for OVRO observations of AFGL 2343 in the LR/ER configurations and simulated 12-meter visibilities. The interferometer samples spatial frequencies in the range 80-360 *lns* (24-108 m), while the 12-meter visibilities represent sampling from \approx 0-40 *lns* (0-12 m).

Table 2.1. Summary of OVRO observations

Object	Line	Track/config.	Calibrators	Date
AFGL 2343	CO J=1-0	2463ER	1749+096, 3C454.3, Uranus	22 Nov 1995
		2470ER	1749+096, 3C273	25 Nov 1995
		2800LR	1749+096, 3C273, Uranus	15 Apr 1996
IRAS 22272+5435	CO J=1-0	2401LR	BL LAC, 3C84	2 Nov 1995
		2802LR	BL LAC, 3C273, Uranus	16 Apr 1996
		2804LR	BL LAC, 3C273, Uranus	18 Apr 1996

yielded a synthesized beam of $5.0'' \times 4.3''$ (FWHM), $PA = -38^\circ$ for IRAS 22272 and a synthesized beam of $4.6'' \times 3.3''$ (FWHM), $PA = -27^\circ$ for AFGL 2343. Natural weighting is a scheme in which each data point in the UV plane is weighted proportionately to the integration time, and yields the best signal to noise. Since the UV tracks at shorter spacings spend more time per unit area, natural weighting tends to emphasize the shorter spacing data more than the points further out. Due to poor spatial sampling of the innermost regions of the UV plane, the spectra of AFGL 2343 from the OVRO images shows considerable (50%) missing flux (Figure 2.6). The UV coverage (Figure 2.5) shows a hole in the central part of the UV plane and this results in poor sampling of the source visibility function at the lowest spatial frequencies, from 0 to 9,000 kilo-wavelengths. In the case of IRAS 22272, the central hole is smaller (Figure 2.4) and the OVRO data appears to measure only a $\sim 20\%$ lower intensity than the 12-meter spectrum (Figure 2.7). To recover all of the lowest spatial frequency Fourier components of the emission towards AFGL 2343 we need a single dish telescope with a diameter which is ideally at least a factor of 2 larger than the OVRO interferometer antennas (Vogel et al. 1984). However, we have used our 12-meter observations (Section 2.6) to recover some information at the lowest spatial frequencies. The single-dish spectra (3×3 grid with $30''$ spacing) were converted to a 3-dimensional image (right ascension, declination, and LSR velocity) in the MIRIAD format. The images were deconvolved by a $55''$ (HPBW) gaussian, simulating the 12-meter telescope beam. The deconvolved images were then weighted by the primary beam of the OVRO 10.4 meter antennas and converted into units of Jy pixel^{-1} . Finally, the images were Fourier transformed to simulate interferometer observations at 100 randomly determined points, within the inner $40 \text{ } \lambda$ s (12-meter) region of the UV plane. The visibilities were interpolated in velocity to give identical spectral sampling for the

OVRO and NRAO 12-m data. The interferometer and single-dish data were then combined with natural weighting and (inverse) Fourier transformed into maps. The resulting AFGL 2343 images, with OVRO and 12-meter data combined, have a synthesized beam of $5.5'' \times 3.9''$ (FWHM), $PA = -28''$.

After Fourier transformation, the images were deconvolved (to remove the sidelobes of the beam) using the CLEAN algorithm, with a gain factor of 0.05. The maximum number of iterations was set large enough so that the level of CLEANing was limited by a brightness cutoff (set to the rms value in the emission-free channels). The cleaning region, determined from the approximate size of the source in the dirty maps, was taken to be $20''$ square for both sources. Once the images were CLEANed, they were convolved with the “clean” (or side-lobe free) beam, using the RESTOR task in MIRIAD.

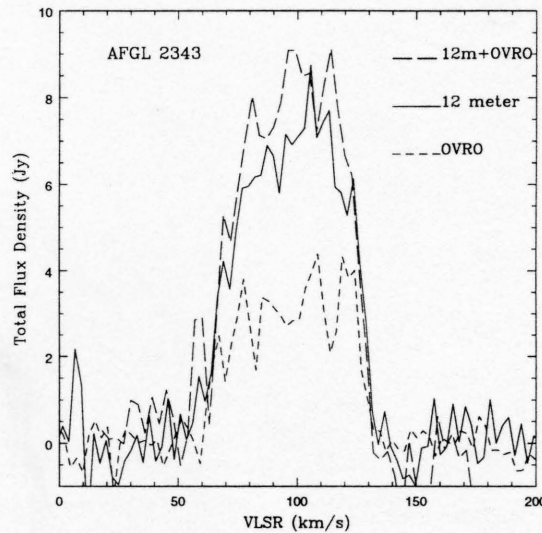


Figure 2.6 CO J=1-0 emission from AFGL 2343. The combined 12-meter and OVRO spectrum (long-dashes), the 12-meter spectrum (solid line), and the OVRO spectrum convolved with a $55''$ beam (short-dashes). The OVRO observations are missing about 50% of the total flux.

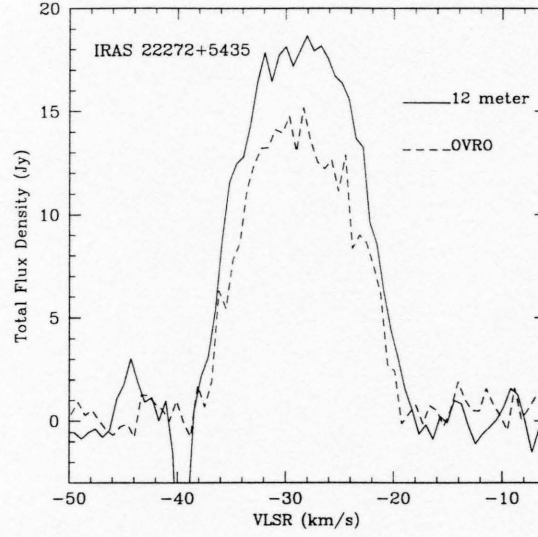


Figure 2.7 CO J=1-0 emission from IRAS 22272+5435. The 12-meter spectrum (solid line) and the OVRO spectrum convolved with a 55'' beam (dashed line).

2.5.4. Results and Analyses

The spectra and maps presented in this section are in units of main beam brightness temperature, T_b (K). These temperatures (which represent the temperature of a black-body which has the same brightness) are related to the intensity (Jy/beam) by the Rayleigh-Jean's Law:

$$I_\nu = \frac{2\nu^2 k}{c^2} T_b \Omega_b$$

where Ω_b is the solid angle (sr) of the beam. This conversion simplifies to: I_ν (Jy/beam) $\approx 8.25 \times 10^{-7} [\nu(\text{GHz})]^2 [\text{HPBW}(\text{arcsec})]^2 T_b(K)$.

The maps of IRAS 22272 (Figure 2.8) and AFGL 2343 (Figure 2.9) show that the CO emission is centrally concentrated, with no *large* departures from spherical symmetry. The velocity panels show that the emission region is largest at or near the systemic velocity, and smallest at the red- and blue-shifted edges of the line. This trend is consistent with line emission from a spherically-symmetric expanding

molecular shell.

We model the CO emission from IRAS 22272 and AFGL 2343 using the statistical equilibrium and radiative transfer codes described in Section 2.3.

IRAS 22272+5435

Images and Spectra – IRAS 22272 has been previously detected in rotational lines of CO, HCN and CS (Woodsworth et al. (1990); Lindqvist et al. 1988; Zuckerman, Dyck and Claussen 1986) which give ample evidence of the carbon-rich nature of this PPNe. More recently, Začs, Klochkova and Panchuk (1995) have derived a C/O ratio of ~ 12 , from high resolution optical spectra of the source. Our maps and spectra are generally consistent with previous observations of CO – a systemic velocity of $\sim -29 \text{ km s}^{-1}$ and a line width of $\sim 20 \text{ km s}^{-1}$. The images of IRAS 22272 (Figure 2.8) show that the CO emission is resolved. It extends out to a radius of about $8\text{--}9''$ ($3\text{--}\sigma$ contour) at the systemic velocity. This angular size corresponds to a radial extent of about $3.5 \times 10^{17} \text{ cm}$, at a distance of 2.7 kpc, our assumed distance to this source. Though the shell is mostly spherical, there is some evidence of an extension towards the SE part of the nebula. The interferometer line shape (Figure 2.10) towards the central pixel appears to be more flat-topped than the distinctly parabolic single-dish spectrum, indicating that the emission is resolved. The emission spans a velocity range of about 19 km s^{-1} , and suggests an expansion velocity of $\sim 9\text{--}10 \text{ km s}^{-1}$.

Model Results – Using the statistical equilibrium and radiative transfer modeling codes we have constructed models of the physical conditions in IRAS 22272. For our models we assume a distance of 2.7 kpc, the same distance as we

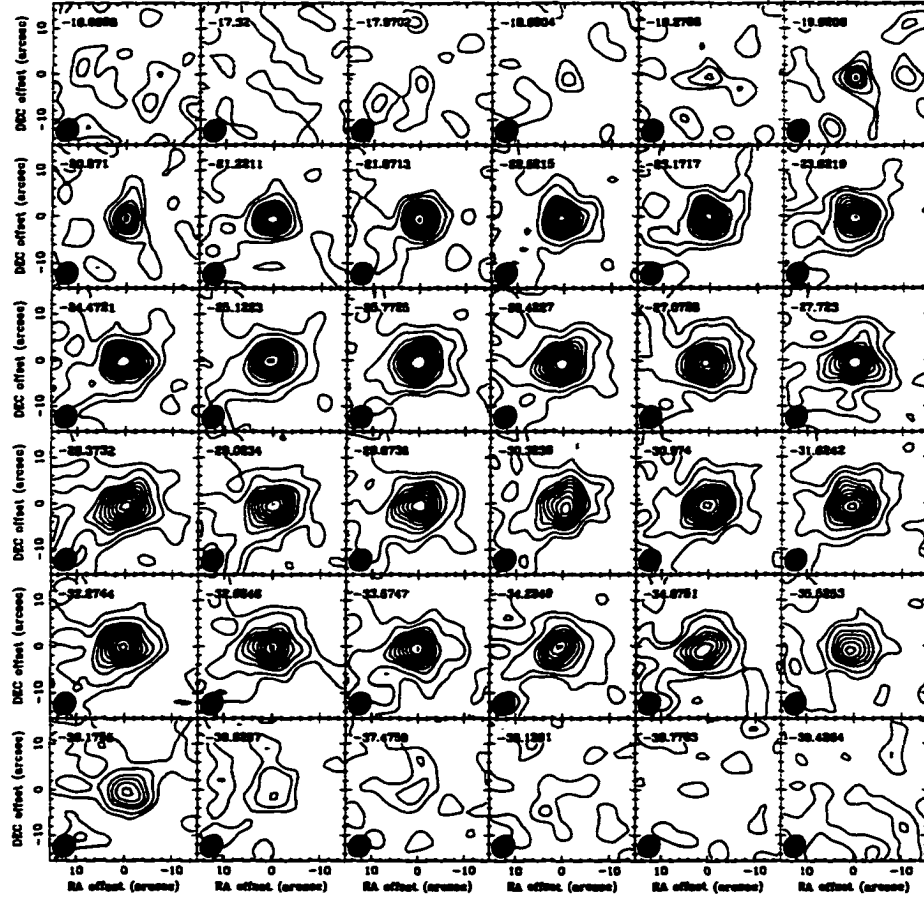


Figure 2.8 Contour maps of CO ($J=1-0$) emission towards IRAS 22272. Each panel is labeled with the LSR Velocity and shows the synthesized beam in the bottom left corner (HPBW $5.0'' \times 4.3''$). The rms noise level is ≈ 0.8 K and the peak is ≈ 16 K. Contour levels are 0.8, 2.4, 4.8, 6.4, 8.0, 9.6, 11.2, 12.8, 14.4, and 16.0 K (T_b).

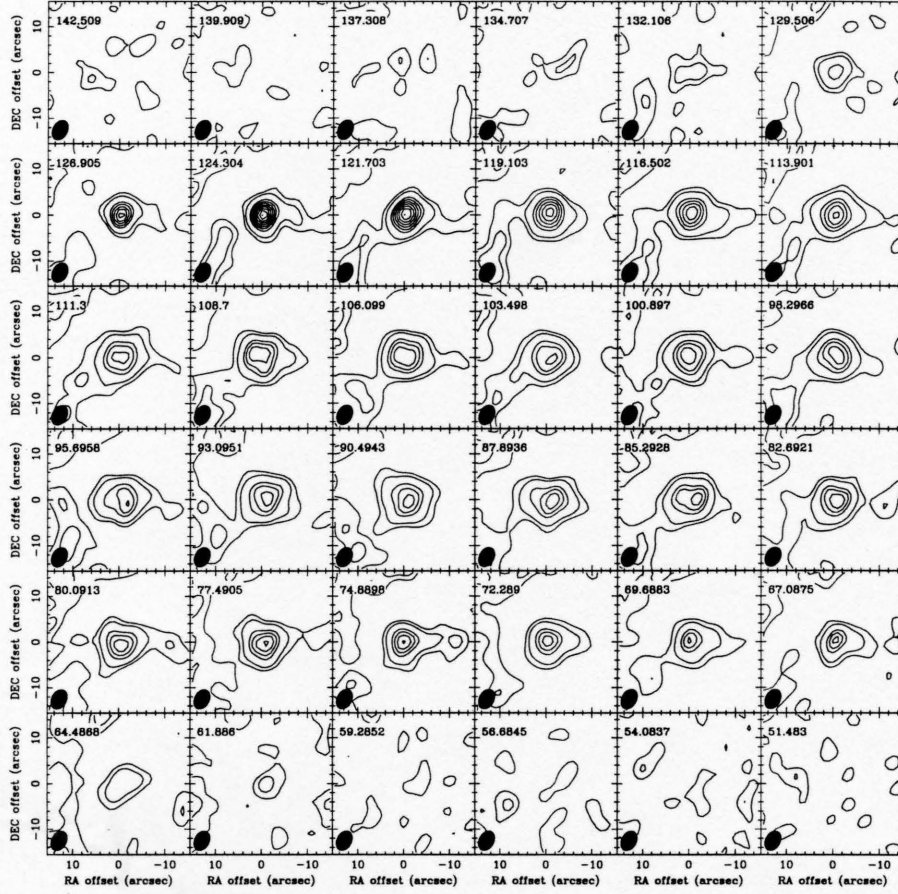


Figure 2.9 Contour maps of CO emission from AFGL 2343. Each panel is labeled with the LSR Velocity and shows the synthesized beam in the bottom left corner (HPBW $4.6'' \times 3.3''$). The rms noise level is ≈ 0.5 K and the peak is ≈ 14 K at the red-shifted edge of the line. Contour levels are 0.5, 1.5, 4.2, 5.6, 7.0, 8.4, 9.8, 11.2, 12.6 and 14.0 K (T_b).

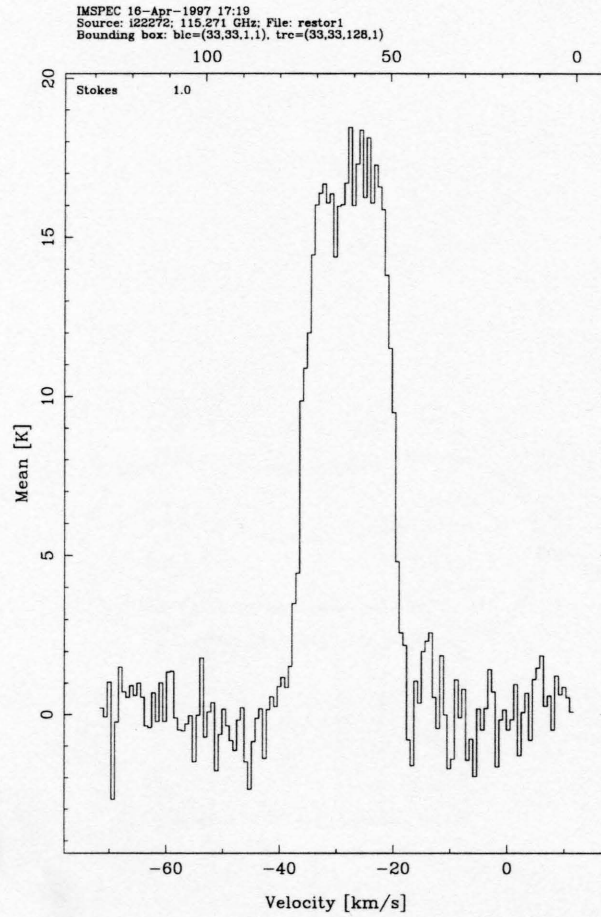


Figure 2.10 CO J=1-0 spectrum towards IRAS 22272 from the OVRO aperture synthesis image (HPBW $5.0'' \times 4.3''$), at the map center. The line intensity is given in units of main beam brightness temperature (T_b K). The velocity resolution is $\sim 1.3 \text{ km s}^{-1}$.

assume for our mid-IR models (refer to Dayal et al. 1997). In a carbon-rich star the CO abundance is determined by the oxygen abundance, while in an oxygen-rich star the CO abundance depends on the carbon abundance. In the case of IRAS 22272 we adopt a peak CO abundance to match the oxygen abundance measured by Začs, Klochkova and Panchuk (1995), who measure $O/H \approx 4 \times 10^{-4}$. Their value agrees with previously measured (average) carbon and oxygen abundances in PNe (e.g. Pasquali and Perinotto 1993; Zuckerman and Aller 1986). Here, we implicitly assume that all the CO is fully associated. We specify the radial abundance of CO (with respect to H_2) as a gaussian with a peak of 8×10^{-4} and an e-folding radius of 2×10^{17} cm. The radial extent of CO is constrained by the observed radial profiles; increasing the e-folding radius leads to a more resolved (flatter) line profile. The spatial extent of CO is related to the mass loss parameters and the abundance by the following equation (Mamon et al. 1988):

$$R_{ph}(CO) = 5 \times 10^{16} \left(\frac{\dot{M}}{10^{-6} M_{\odot} \text{yr}^{-1}} \right)^{0.6} \left(\frac{f_{CO}}{4 \times 10^{-4}} \right)^{0.5} \left(\frac{15 \text{ km s}^{-1}}{v_e} \right)^{0.5} \text{ cm} \quad (2.1)$$

$R_{ph}(CO)$ is the radius at which CO is significantly photodissociated by the interstellar UV field. It is a function of the number density of CO (since $n_{CO} \approx f_{CO} \times \frac{\dot{M}}{v_e r^2}$ for a spherical, uniformly expanding CSE) and is derived after including self-, H_2 and dust shielding from the ambient interstellar UV field. Using the above equation, and our “best-fit” \dot{M} of $5 \times 10^{-5} M_{\odot} \text{yr}^{-1}$, we derive $R_{ph}(CO) \sim 8 \times 10^{17}$ cm. Though this value is larger than the CO e-folding radius based on our model fit, we believe that our observations and models constrain the angular extent of the CO very well and the discrepancy could easily be a result of uncertainties in the distance to IRAS 22272 and/or the simple assumption about a constant mass loss rate in Equation 2.1. Our models show that the CO is predominantly collisionally excited and the emission therefore depends strongly on the assumed mass loss rate, or density since $n_{H_2} \sim \frac{\dot{M}}{V_e r^2}$. The excitation temperature

(T_{ex}) which is calculated by the program, tracks the kinetic temperature (T_{kin}) for $r \leq 2 \times 10^{17}$ cm, where $n_{H_2} \sim 2000 \text{ cm}^{-3}$. At larger radii the CO is sub-thermally excited and probably contributes little to the observed emission: this potentially provides yet another explanation for the discrepancy between the observed CO extent and the predicted photodissociation radius.

Our models reproduce the observed images and spectra, to within the noise level in our maps (see Figure 2.11). We also calculate the J=2-1 spectrum for comparison with the SEST spectrum of Woodsworth et al. (1990) (Figure 2.15) and find that our model profile matches the parabolic line profile observed by Woodsworth et al. (1990), both in line shape and peak intensity ($\sim 3 \text{ K} \cdot T_{mb}$). Fitting multiple CO transitions allows us to constrain T_{kin} , since $T_{kin} \approx T_{ex}$ for most part. We find that a rather flat kinetic temperature law ($T_{kin} \sim R^{-0.2}$), which gives a kinetic temperature of $\sim 25 \text{ K}$ at $4 \times 10^{16} \text{ cm}$ ($\sim 1''$) from the center, provides a good fit to the line intensities. Since the J=2-1 transition of CO probes regions of higher densities and temperatures (i.e. closer in to the dust photosphere) than the J=1-0 transition, and a single model provides good fits to both line profiles, we conclude that (to within our resolution) we do not detect evidence for spatial (or temporal) changes in the mass loss rate.

AFGL 2343

Images and Spectra – AFGL 2343 has previously been detected in rotational lines of CO, ^{13}CO , SiO (Bujarrabal et al. 1992; Likkell et al. 1987; Zuckerman and Aller 1986) and also weakly detected in H_2S (Omont et al. 1993). The detection of OH masers at 1612 and 1667 MHz by Likkell (1989) (as well as SiO) and the non-detection of HCN (Bujarrabal et al. 1992) strongly suggest an oxygen-rich

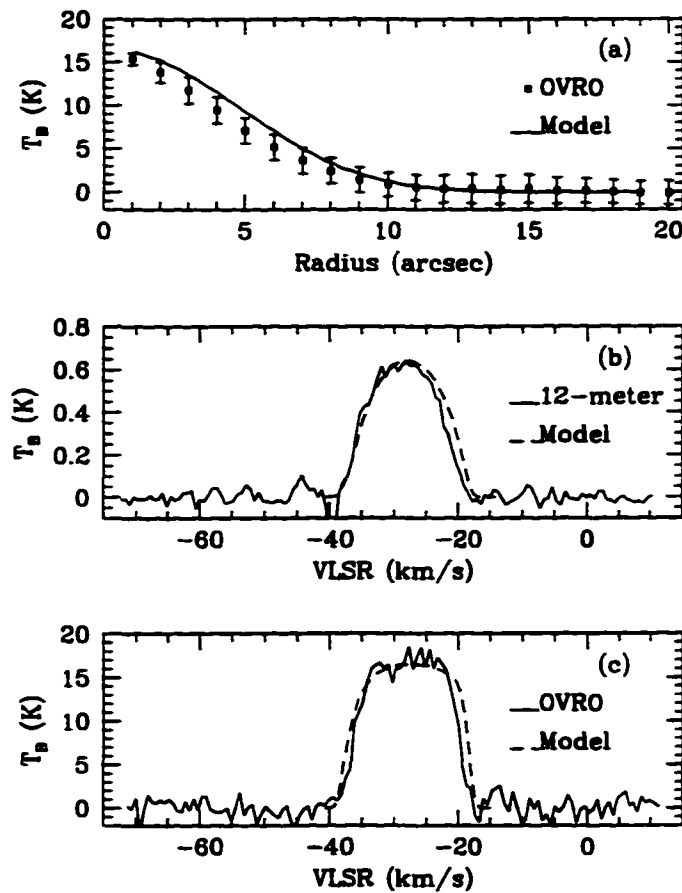


Figure 2.11 IRAS 22272: Observed spectra and radial profiles, compared with model fits. (a) Observed average radial brightness profile for the CO $J=1-0$ transition derived from a 2.6 km s^{-1} wide map centered at the systemic velocity (*filled squares*); and model radial brightness profile (*solid line*). (b) Comparison of spectrum from the NRAO 12-meter telescope (*solid line*) with model spectrum convolved with a 55'' beam (*dashed line*). (c) Comparison of OVRO spectrum from aperture synthesis image (*solid line*) with model spectrum convolved with a 5'' beam (*dashed line*).

circumstellar environment. The spectrum of AFGL 2343 resembles a G5 supergiant (Kwok, Volk and Hrivnak 1989); a supergiant classification is also supported by the observed high expansion velocity and derived mass loss rate (Hawkins et al. 1995). Our interferometer images (Figure 2.9) show that the source is centrally peaked and compact, but resolved. The emission is considerably more compact towards the red-shifted edge of the line, than towards the systemic velocity or the blue-shifted edge. The emission appears to extend out to a radius of $\sim 6''$ at the systemic velocity. While the emission is resolved, we do *not* see evidence for an NE–SW elongation as seen by Bujarrabal et al. (1992) in their ^{12}CO J=2–1 maps. This is very surprising as our observations have a better spatial resolution than Bujarrabal et al. (1992) and the J=1–0 line generally probes a more extended region than the J=2–1 line. Also, we see no obvious correlation between our maps and the bright lobes seen in the mid-IR images of dust emission (Hawkins et al. 1995).

Figure 2.12 shows the emission line towards the center of the source. The line width and line center velocities are consistent with previous millimeter-wave observations. The emission extends over a velocity range of approximately 75 km s^{-1} , from $+60 \text{ km s}^{-1}$ to $+135 \text{ km s}^{-1}$ (V_{lsr}). The systemic velocity lies near $+98 \text{ km s}^{-1}$. The spectra and images show that the emission line is “U-shaped” but very asymmetric. The red-shifted line peak, near $+125 \text{ km s}^{-1}$ is significantly stronger than the corresponding blue-shifted peak near 70 km s^{-1} . The “U-shaped” line profile indicates that the emission is optically thin and well-resolved. The asymmetry in the blue and red peaks has at least two possible interpretations: (i) The CSE is spherically symmetric but there is a strong temperature gradient along radial lines outwards from the central star. This would result in considerable self-absorption of the blue-shifted emission, by cooler (foreground) gas, leading to

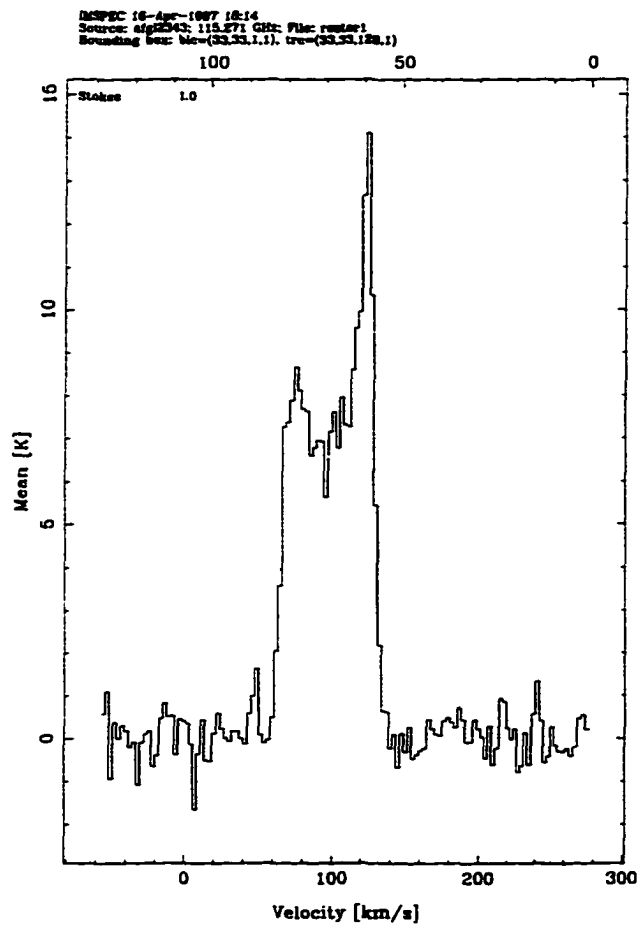


Figure 2.12 CO J=1-0 spectrum towards AFGL 2343 from OVRO aperture synthesis image (HPBW $4.6'' \times 3.3''$), at the map center. The line intensity is in units of main beam brightness temperature (T_b K). The velocity resolution is 2.6 km s^{-1} .

a lower blue-shifted peak. (ii) The CSE has a bipolar structure and most of the CO resides in two clumps. The red-shifted clump has more molecular gas and/or higher excitation temperatures than the blue-shifted component. From our images, there is no evidence for a resolved bipolar-type structure. However the large degree of asymmetry in the line peaks appears to support the second interpretation. Such an asymmetry was also seen by Likkell (1989) in OH maser lines towards this source. To further examine the kinematics of the CSE, we have constructed position-velocity maps from our interferometer data cubes (Figure 2.13). These maps are useful diagnostics of spatial differences in the positions (relative RA, DEC) of the red- and blue-shifted peaks of the emission line. We find that the line peaks are spatially co-incident to within our resolution. If the source is indeed bipolar then the axis of the outflow probably lies almost parallel to our line-of-sight to the source.

Models – Estimates for the distance to AFGL 2343 range from ~ 1 kpc (Van der Veen et al. 1989) to 6 kpc (Hawkins et al. 1995; Zuckerman and Dyck 1986). Studies that assume (or calculate) the larger value for the distance propose that AFGL 2343 is a true supergiant with a luminosity of $\geq 10^5 L_{\odot}$ and a massive dust envelope, $M_d \approx 6 M_{\odot}$ (e.g. Hawkins et al. 1995; Kastner and Weintraub 1994). For our models of AFGL 2343 we also assume the kinematical distance of 6.0 kpc. The peak CO abundance was initially assumed to be 2×10^{-3} w.r.t. H_2 , in accordance with the carbon abundance calculated by Zács (1996). Since AFGL 2343 is oxygen rich, the CO abundance is determined by the abundance of carbon. However, such a high CO abundance yields a parabolic line profile representative of an optically thick circumstellar envelope, and is completely inconsistent with our observed spectrum. After repeated iterations (varying the mass loss rate also) the peak

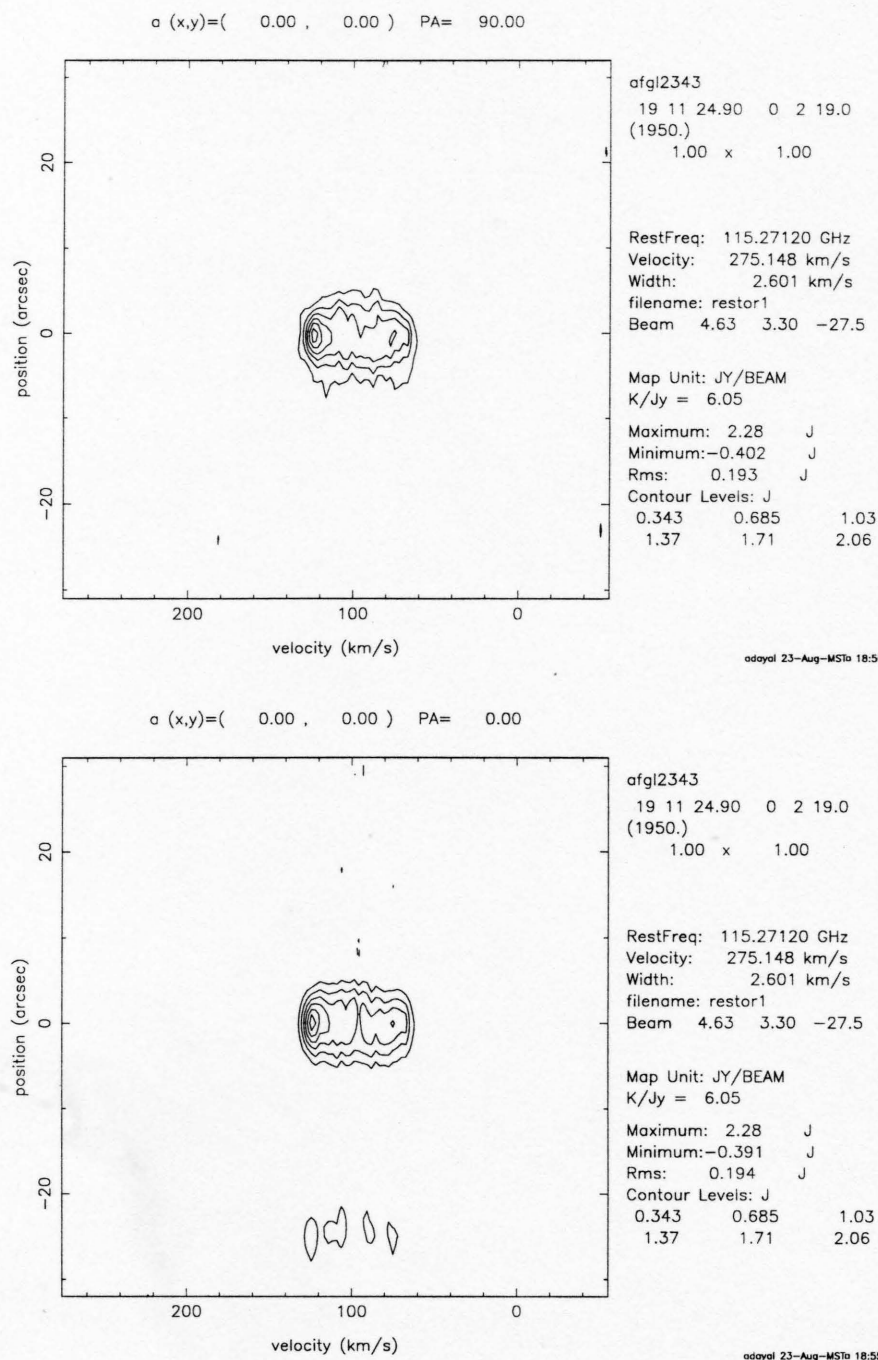


Figure 2.13 Position-Velocity diagrams for AFGL 2343. The contours show the change in flux density in the (*top*) R.A. Vs VEL plane, at zero relative DEC and (*bottom*) DEC. Vs VEL plane, at zero relative R.A. Both line peaks appear to be at the same spatial location,

abundance is found to be $\sim 7 \times 10^{-4}$. The e-folding radius of the CO is constrained by the extent of CO as well as the line profile. If the CO e-folding radius is too small, the shell appears unresolved and the model line profile appears flatter than the data. The “best-fit” e-folding radius of the gaussian representing the CO abundance is $\sim 2 \times 10^{18}$ cm. Using equation 2.1 we calculate a CO photodissociation radius of 1.2×10^{18} cm.

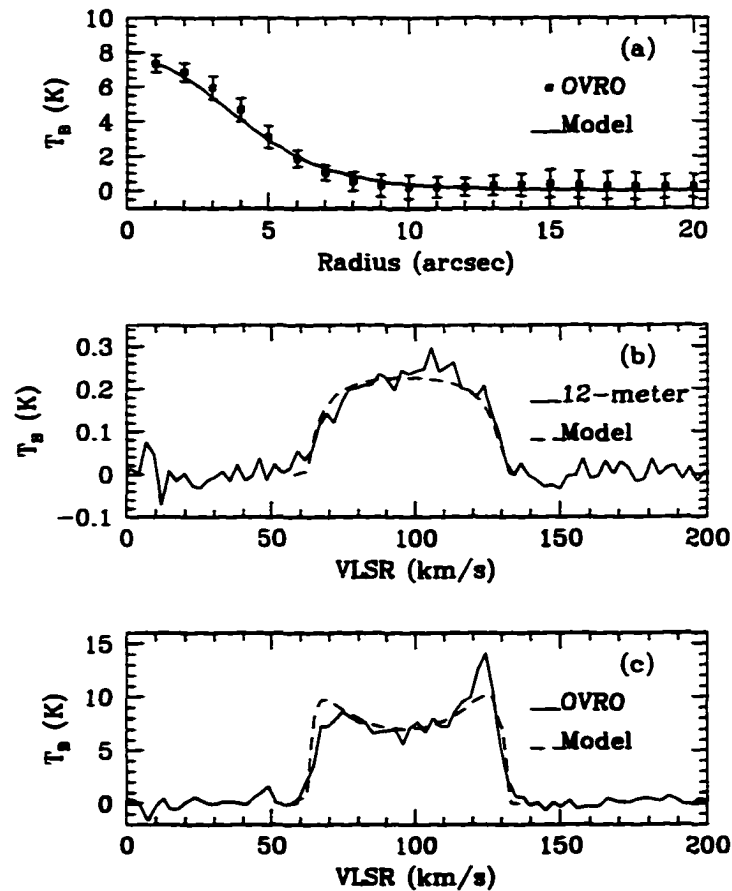


Figure 2.14 AFGL 2343: Observed spectra and radial profiles, compared with model fits. (a) Observed average radial brightness profile for the CO J=1-0 transition derived from a 3 km s^{-1} wide map centered at the systemic velocity (*filled squares*); and model radial brightness profile (*solid line*). (b) Comparison of spectrum from the NRAO 12-meter telescope (*solid line*) with model spectrum convolved with a $55''$ beam (*dashed line*). (c) Comparison of OVRO spectrum from aperture synthesis image (*solid line*) with model spectrum convolved with a $5''$ beam (*dashed line*).

At the large of 6 kpc, our models require a rather high mass loss rate. $\dot{M} \sim 3 \times 10^{-4} M_{\odot} \text{ yr}^{-1}$, to match the observed line intensities. As in the case of IRAS 22272, our models show that the CO is thermalized and that excitation of the CO molecules is predominantly via collisions. However the millimeter optical depths are lower than in IRAS 22272 and the excitation temperature is lower than the kinetic temperature for $R \geq 1.5 \times 10^{17} \text{ cm}$. Our models (Figure 2.14) suggest that the radial profile and spectra fits are generally quite good. We also calculate the line profile for the J=2–1 transition (Figure 2.15) and find that it agrees very well with the observations of Omont et al. (1993), after convolving to the 13'' resolution of the IRAM telescope beam. However the model does not reproduce the rather large asymmetry in the red- and blue-shifted peaks of the interferometer spectrum. This shortfall may be an indication that the kinematical structure of AFGL 2343 is more complicated than our assumption about a spherically symmetric envelope.

The “best-fit” model parameters are summarized in Table 2.2.

Table 2.2. Summary of Millimeter-wave statistical equilibrium models

<i>Object</i>	R_{in} (cm)	R_{out} (cm)	T_{kin} (K)	\dot{M} ($M_{\odot} \text{ yr}^{-1}$)	X(CO) (wrt H_2)	d (kpc)
IRAS 22272	3.4×10^{16}	8.0×10^{17}	$25 \times [r/4 \times 10^{16} \text{ cm}]^{-0.2}$	4.5×10^{-5}	8×10^{-4}	2.7
AFGL 2343	8.0×10^{16}	1.8×10^{18}	$50 \times [r/1 \times 10^{17} \text{ cm}]^{-1.0}$	2.5×10^{-4}	7×10^{-4}	6.0

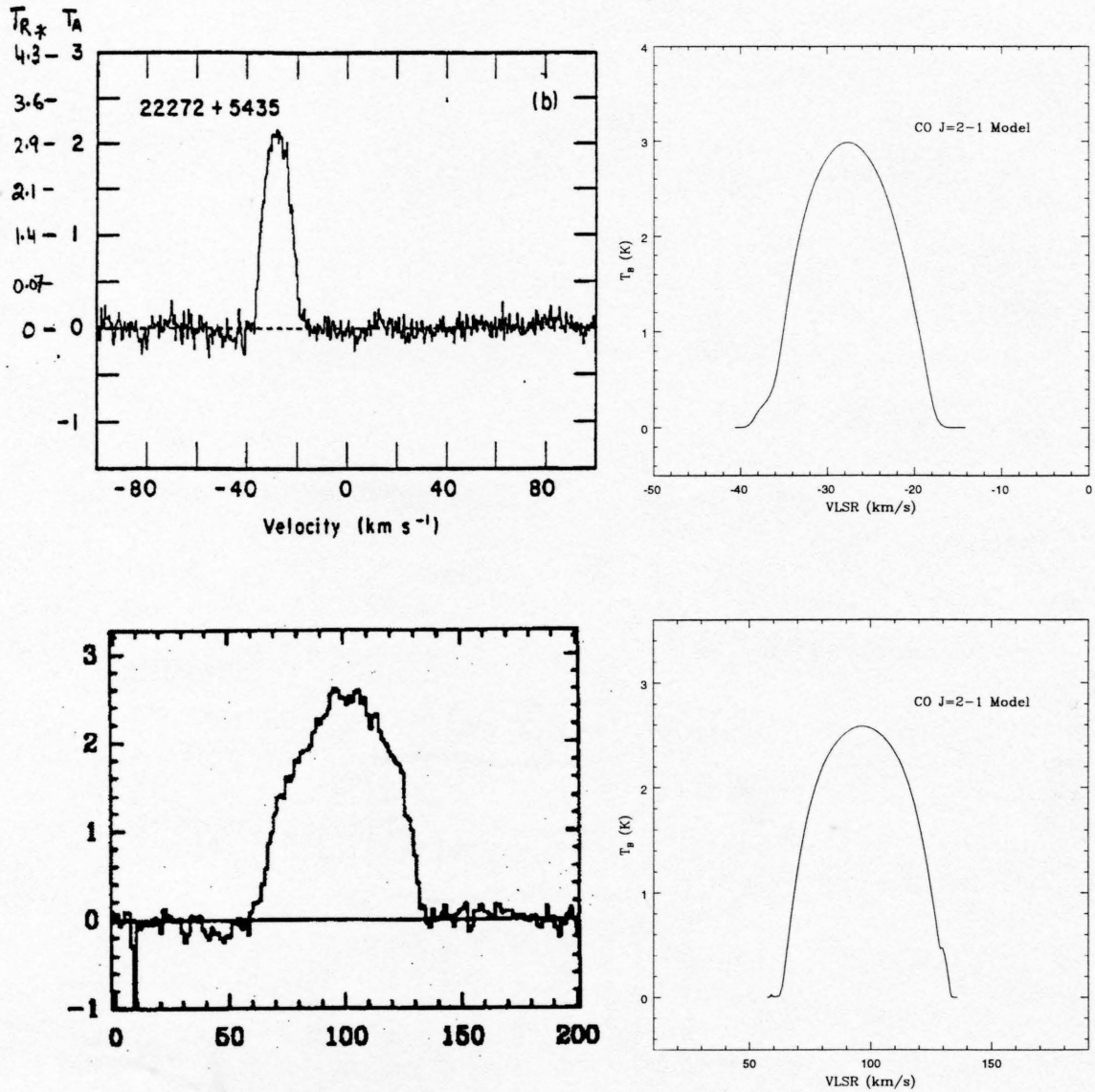


Figure 2.15 *Top:* IRAS 22272 – Best fit model J=2–1 spectrum (right) and observed J=2–1 spectrum (left) from Woodsworth et al. (1990). Model is convolved with a 22'' gaussian to simulate the resolution of the SEST 15-m telescope. *Bottom:* AFGL 2343 – Best fit model J=2–1 spectrum (right) and observed J=2–1 spectrum (left) from Omont et al. 1993. Model is convolved with a 13'' gaussian to simulate the resolution of the IRAM 30-m telescope. Both spectra have the same units – T_b (K) (main beam brightness temperature).

2.6. Single-dish spectroscopy/mapping

As AGB stars evolve, the outer layers of the central star are ejected, exposing the hotter inner core. This mass ejection leads to a hardening of the stellar radiation field towards the UV and as a consequence, photodissociation of molecular material and ionization of atomic material. The photodissociation of molecules, which also depends on the mass loss rate (or density) in the envelope and the ambient interstellar UV field, increases as the nebula evolves. The detection/non-detection of molecular emission from PPNe and PNe is therefore an important clue to the evolutionary state of these objects. In the first comprehensive survey of 100 PNe in CO $J=2-1$, Huggins and Healy (1989) detected CO in only 20% of the sources. From their results, they established that the detected PNe generally showed a bipolar morphology and suggested that PNe with substantial molecular envelopes are generally higher mass, younger disk population objects, with higher mass loss rates. Corradi and Schwarz (1995) have imaged ~ 400 PNe; they find the bipolar PNe have significantly lower z heights above the Galactic plane and significantly hotter central stars than elliptical nebulae. They suggest that bipolar PNe are therefore produced by more massive progenitors than other morphological types. A similar correlation between molecular gas and morphology (or mass) is also found from near-IR observations of H_2 emission (e.g. Kastner et al. 1996; Latter et al. 1995; Zuckerman and Gatley 1988). Since the initial CO survey many more PNe and PPNe have been detected and/or mapped in one or more transitions of CO (Huggins et al. 1996; Dayal and Bieging 1996; Bachiller et al. 1993; Bujarrabal et al. 1992; Forveille and Huggins 1991; Bieging et al. 1991; Shibata et al. 1989). The observations show that the emission lines towards PPNe and PNe have a wide variety of profiles. Some sources (mostly post-AGB objects and PPNe) show parabolic line shapes (like most AGB stars) indicating that their CSEs are compact

(unresolved) and optically thick. More extended PPNe often show “U-shaped” line profiles (e.g. NGC 2440), indicative of optically thin expanding molecular shells. Other objects show remarkably narrow line profiles (e.g. AFGL 915), suggesting that the CO emission emanates from isolated molecular condensations within the telescope beam.

We have observed 18 objects in various phases of transition from the AGB to the PN phase in the CO J=1–0 (115.271 GHz) and CO J=2–1 (230.538 GHz) lines, with the NRAO 12-meter telescope on Kitt Peak. The objectives of this study were to: (a) estimate (or obtain limits to) the total amount of molecular mass, (b) identify candidates that were bright enough for follow-up high resolution interferometry in the CO J=1–0 line, and (c) recover lowest spatial frequency information to supplement our interferometer observations. Since this study was conducted concurrently with the mid-IR observations, *most* of the objects that were selected were known to have thick, dusty envelopes and a high $10\mu\text{m}$ flux density, $F_{10} \geq 4$ Jy. The initial results of our observations of CO towards six young PNe were published earlier (Dayal and Bieging 1996). Here, we present results on individual sources which were not included in that paper.

The observations presented here were made in standard beam-switching mode (“chopping” the subreflector), with a 4-arcmin throw in azimuth; however the throw was changed often and sometimes position-switching (“nodding” the telescope) was used to avoid contamination from interstellar CO. Calibration was by the chopper vane method (Kutner and Ulich 1981), producing spectra in units of T_R^* . Typical SSB system temperatures during these observations were about 600 K. Spectra were obtained with both the filterbank and the hybrid spectrometer, in both senses of circular polarization, and the two polarizations were averaged

together. Temperatures presented in T_R^* can be converted into units of main beam brightness temperature (T_b) by dividing by the corrected beam efficiency, η^* which is 0.83 at 115 GHz and 0.51 at 230 GHz.

IRAS 07134+1005 and IRAS 04296+3429 - These C-rich PPNe which (like IRAS 22272+5435) show the prominent $21\mu\text{m}$ emission feature, were observed in CO J=2-1 by Woodsworth et al. (1990) and also by Omont et al. (1993). IRAS 07134 was observed by Bujarrabal et al. (1992) in CO, ^{13}CO and HCN. Both sources have large radial velocities (Table 2.3), but our 12-meter J=1-0 spectra line profiles appear (Figure 2.16) to suggest compact, optically thick molecular envelopes; however, the spectrum towards IRAS 04296 shows a somewhat flatter line profile, which suggests that the mass loss rate (hence optical depths) are lower than in IRAS 07134. We have constructed maps from a $30''$ spacing 3×3 grid of spectra for IRAS 07134. Our maps indicate that the emission is unresolved in the $55''$ 12-meter beam.

HD 161796 - This high latitude object with a supergiant-like optical spectrum was originally classified as post-AGB by Parthasarathy and Pottasch (1986) on the basis of its large infrared excess. Optical and infrared photometry by Hrivnak et al. (1989) together with the IRAS measurements clearly show the double-peaked spectrum that is characteristic of PPNe. CO emission towards HD 161796 was first reported by Likkell et al. (1991), and later also observed by Bujarrabal et al. 1992. We have observed the J=2-1 and J=1-0 lines of CO with a high spectral resolution (0.65 km s^{-1}). Our spectra (Figure 2.17) confirm previous measurements of the radial velocity and the expansion velocity ($\sim 15 \text{ km s}^{-1}$). Both lines are somewhat asymmetric, falling off more sharply towards the red-shifted edge, but the J=2-1

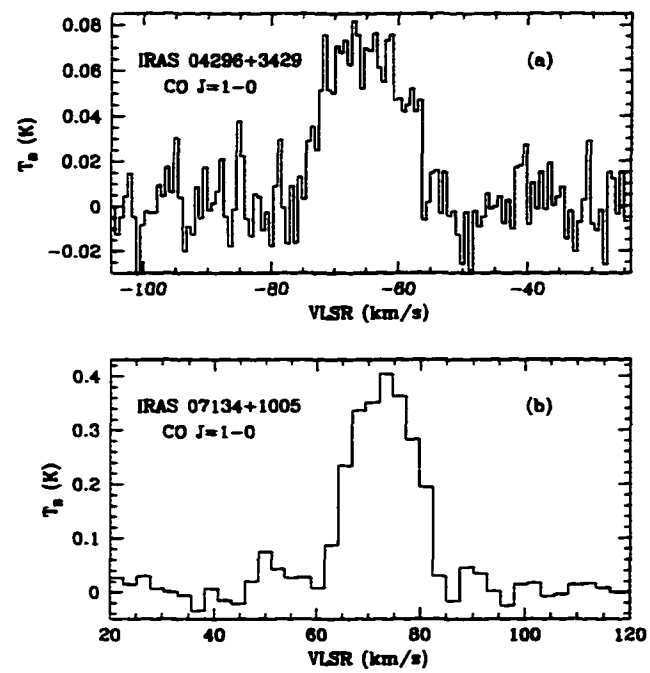


Figure 2.16 12-meter CO J=1-0 spectra towards (a) IRAS 04296+3429. Channel resolution is 250 kHz, or 0.65 km s^{-1} and (b) IRAS 07134+1005. Channel resolution is 1 MHz or 2.6 km s^{-1} .

line clearly shows pronounced wings and a somewhat larger line-width than the $J=1-0$ line. These results suggest that the higher excitation ($2-1$) line is probing a faster, more asymmetrical molecular outflow, than that traced by the $J=1-0$ line. Furthermore, the wings (as opposed to a sharp cut-off in intensity, with velocity) suggest a velocity gradient of the form $V(r) \sim V_o(r/r_o)^\alpha$ (Cabrit and Bertout 1986). Similar (though more pronounced) line wings have been observed in the well known PPN AFGL 2688 by (Jaminet et al. 1992), who suggested that their submillimeter lines showed emission from two distinct components of the envelope: a cooler, circularly symmetric dense slow (red-giant) wind and a faster, optically thin bipolar wind.

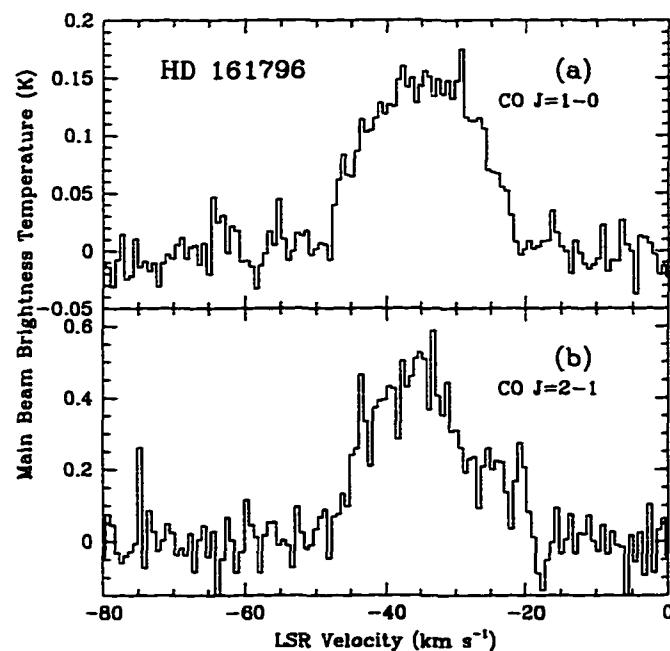


Figure 2.17 12-meter CO spectra towards HD 161796 For both lines velocity resolution is 0.65 km s^{-1} , corresponding to a channel resolution of 250 kHz and 500 kHz, for $J=1-0$ and $J=2-1$ respectively.

IRAS 06562-0337 and NGC 6302 - IRAS 06562 is an object that is possibly on the tip of the AGB (Garcia-Lario et al. 1993). The appearance and subsequent disappearance of forbidden lines indicate (together with the changing nature of the H-alpha lines) that this is an effect of the episodic nature of the mass loss mechanism, preceding the formation of a PN. We see no evidence for an emission feature of circumstellar origin. There is a strong (narrow) interstellar feature at $\sim 50 \text{ km s}^{-1}$. There is a tentative detection of the J=1-0 line towards NGC 6302 for which the spectrum were obtained during poor atmospheric conditions ($T_{\text{sys}} \sim 1000 \text{ K}$). The J=2-1 line towards NGC 6302 is bright and has previously been detected by Huggins and Healy (1989).

Hb 12 and Vy 2-2 Our observations towards both these young, oxygen-rich PNe were contaminated by bright interstellar emission lines in our bandpass, both towards the source and in the off-source beams. There appears to be no clear evidence for circumstellar CO emission; however a few narrow emission lines are seen towards both objects, in the velocity range $8\text{--}20 \text{ km s}^{-1}$ for Vy 2-2, and near 40 km s^{-1} towards Hb 12.

M 1-78 and M 2-43 Both these sources appear to have high excitation, carbon rich circumstellar environments; they both show bright hydrocarbon emission features as well as fine-structure lines in the mid-IR (Zavagno, Cox and Baluteau 1992). We did not detect any CO emission towards M 2-43. However, there is a bright, narrow ($\leq 10 \text{ km s}^{-1}$ FWHM) emission line at $\sim -65 \text{ km s}^{-1}$ towards M 1-78. This line coincides with the J=2-1 line observed by Huggins et al. (1996), which showed broad emission wings. Based on the line strength and profile, Huggins et al. suggest that M 1-78 is a compact H II region misclassified as a PN.

Our CO $J=1-0$ line profile (intensity and width), which is atypical of CO emission lines from PPNe and PNe, also supports this argument.

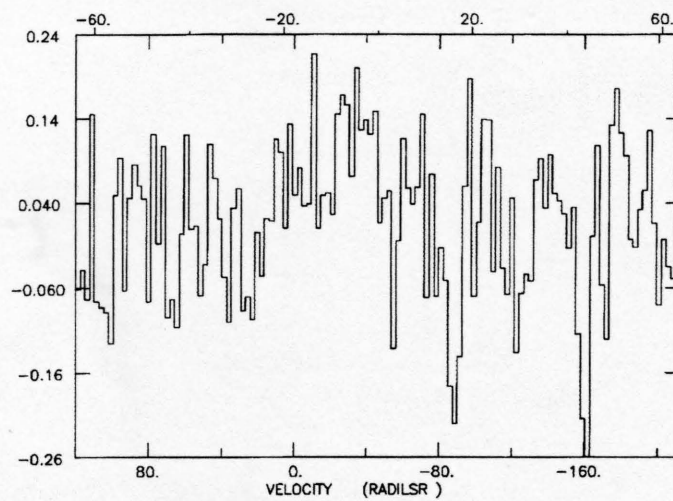
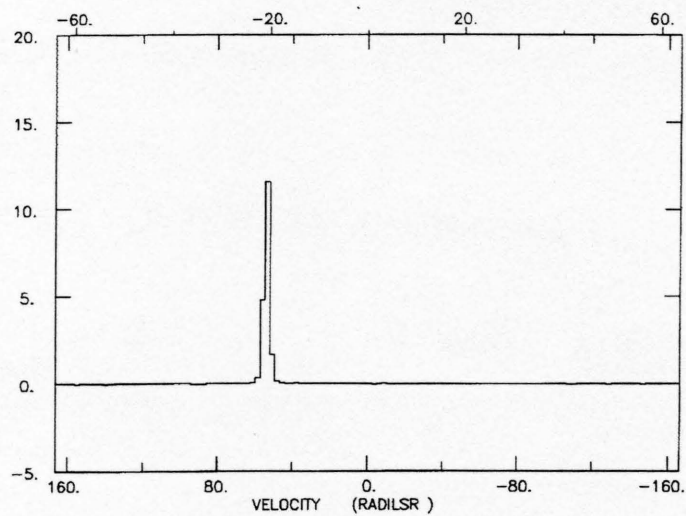


Figure 2.18 12-meter observations of CO J=1-0 emission towards IRAS 06562-0337 (top) and NGC 6302 (bottom). Units of intensity are T_R^* .

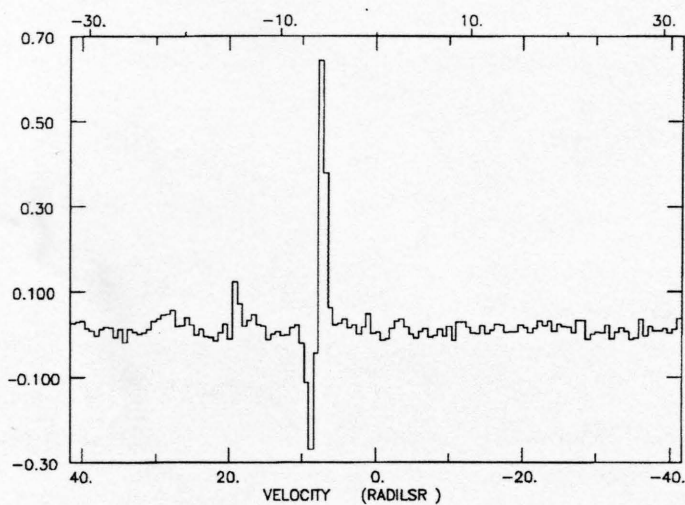
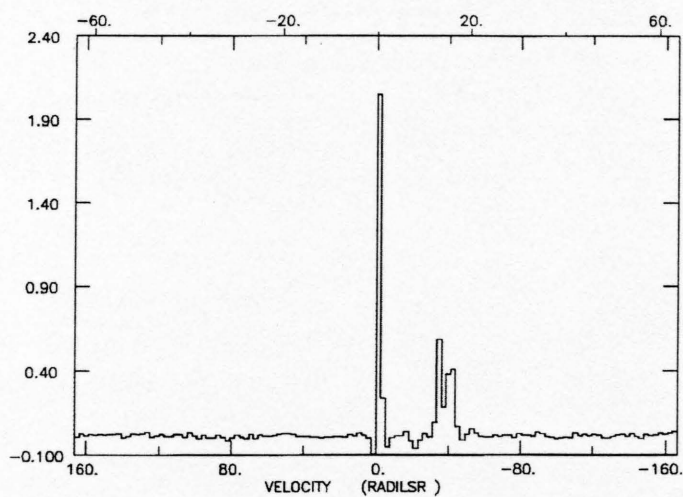


Figure 2.19 12-meter observations of CO J=1-0 towards Hb 12 (top) and Vy 2-2 (bottom). Units of intensity are T_R^* .

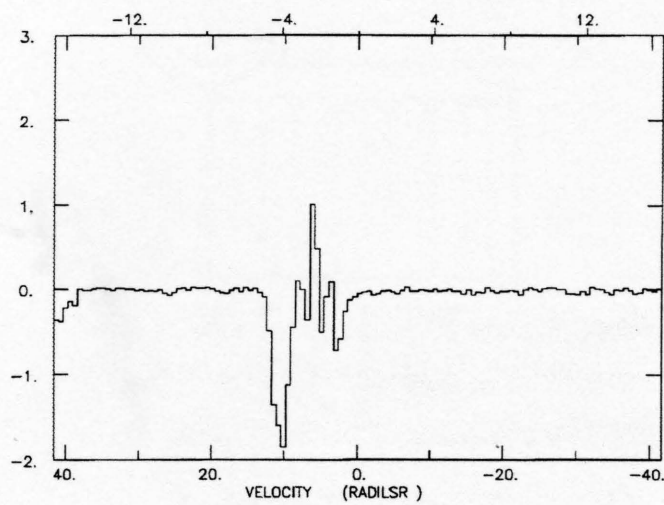
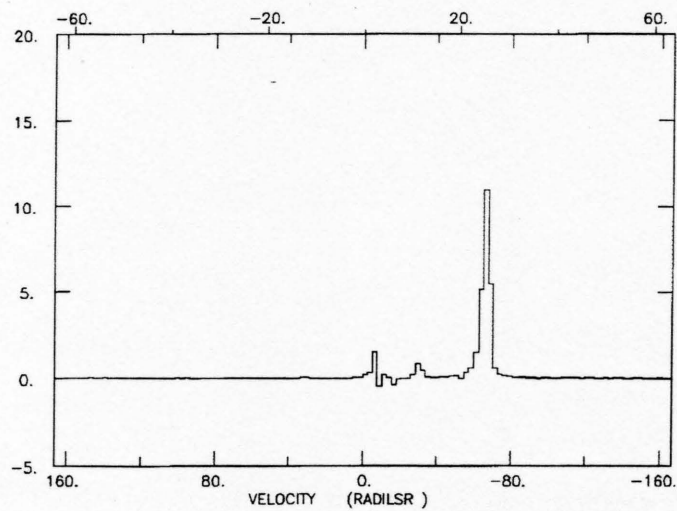


Figure 2.20 12-meter observations of CO $J=1-0$ emission towards M 1-78 (top) and M 2-43 (bottom). Units of intensity are T_R^* .

Table 2.3. Summary of 12-meter CO observations

Object	Type	RA, DEC (1950)	Lines	V_{sys} (km s ⁻¹)	V_{exp} (km s ⁻¹)	$\int T_{mb} dV$ (K km s ⁻¹)	RMS (K)
M 4-18	PN	04:21:32	1-0	0.21	0.007
		+60:00:24	2-1	0.48	0.016
IRAS 04296	PPN	04:29:40	1-0	-66	10.4	1.06	0.014
		+34:29:53					
IC 418	PN	05:25:10	1-0/H38 α	+38	25	1.13	0.008
		-12:44:15	2-1	0.8	0.016
AFGL 915	PN	06:17:37	1-0	+1	11	0.41	0.009
		-10:36:52	2-1	-1	11	1.36	0.018
IRAS 06562	PPN?	06:56:15	1-0	0.025
		-03:37:03					
IRAS 07134	PPN	07:13:25	1-0	+72	10.5	5.93	0.019
		+10:05:09					
NGC 2440	PN	07:39:41	1-0	+42	29	0.83	0.006
		-18:05:26	2-1	+41	29	3.24	0.024
BS 4049	PPN	10:15:50	1-0	0.018
		-28:44:29					
NGC 6302	PN	17:10:21	1-0	+30?	30?	...	0.104
		-37:02:38					
HD 161796	PPN	17:43:41	1-0	-34	13	2.89	0.016
		+50:03:49	2-1	-35	15	8.39	0.065
M 2-43	PN	18:24:03	1-0	0.012
		-02:44:49					
AFGL 2343	PPN	19:11:25	1-0	+99	35	13.7	0.018
		+00:02:19					
VY 2-2	PN	19:21:59	1-0	0.024
		+09:48:00					
K 3-35	PN	19:25:35	1-0	0.009
		+21:23:54	2-1	+25	16	1.17	0.013
M 1-78	PN?	21:19:06	1-0	0.012
		+51:40:39					
IC 5117	PN	21:30:37	1-0	-10	17	1.93	0.016
		+44:22:29	2-1	-9	17	7.00	0.015
IRAS 22272	PPN	22:27:13	1-0	-31	9.5	8.38	0.045
		+54:35:44					
HB 12	PN	23:23:57	1-0	0.012
		+57:54:24					

2.7. Summary of Chapter 2

We present millimeter-wave interferometry of molecular emission from the AGB star IRC+10216 and two PPNe, IRAS 22272+5435 and AFGL 2343. We also present single-dish observations of CO in a number of PPNe and PNe. From the interferometer observations we construct statistical equilibrium and radiative transfer models, to infer abundances and physical conditions in the CSEs. From the single dish data we calculate (or derive limits to) total molecular masses, under assumptions of LTE.

1. Our maps of HCN, CN and C₄H show that the interstellar UV field initiates a variety of photochemical reactions in the outer envelope, and that CN is produced by the photodissociation of HCN. Our results also suggest that photochemical models generally need to incorporate more reaction pathways for CN. CN appears to be lower in abundance (relative to HCN) than the models predict.

2. Millimeter-interferometry of IRAS 22272+5435 shows no pronounced deviations from spherical symmetry. Our observations and model results indicate that the CO emission is optically thick but resolved. We derive an expansion velocity of $\sim 10 \text{ km s}^{-1}$, a mass loss rate of $\sim 5 \times 10^{-5} M_{\odot} \text{ yr}^{-1}$ and a relatively flat kinetic temperature law ($T_k \sim R^{-0.2}$).

3. Interferometry of AFGL 2343 also indicates no direct spatial evidence for strong deviations from spherical symmetry. The emission line appears to be optically thin, very broad ($\sim 70 \text{ km s}^{-1}$) and asymmetric, and suggests that there may be a significantly higher amount of red-shifted gas than blue-shifted gas, and points to a bipolar outflow. However, there appear to be no spatial differences between the positions of the red and blue-shifted peaks. We derive a very high mass loss rate of $\sim 3 \times 10^{-4} M_{\odot} \text{ yr}^{-1}$, and a steep kinetic temperature law ($T_k \sim$

R^{-1}).

4. From our single-dish observations of young PNe we derive excitation temperatures, column densities and estimates for the total mass of molecular gas. By comparing the molecular mass to mass of ionized gas we can place our sources in an evolutionary sequence. We find that NGC 2440 is the most evolved PNe in our millimeter study, $M_{mol}/M_i \approx 0.04$ while IC 5117 appears to be the youngest $M_{mol}/M_i \approx 6$ (Dayal and Bieging 1996). IC 418 and M 4-18 show evidence for evolution from low-mass progenitor stars.

CHAPTER 3

MID-INFRARED IMAGING OF WARM DUST EMISSION

3.1. Overview

We present mid-IR ($8\text{--}21\mu\text{m}$) images of a small sample of PPNe and young PNe at wavelengths which sample continuum emission as well as dust feature emission. The objectives of our mid-IR study are to: (1) infer the structure and morphology of the dust shells, and to relate these to the morphologies of the molecular envelopes. (2) map the dust shells at multiple wavelengths including various spectral features, so as to determine spatial variations in the distribution of spectrally distinct emitters, and obtain abundance estimates in some cases. (3) infer the temperature and density variations across the nebula from maps of the color temperature and optical depth constructed from our images.

This chapter is divided into the following sections:

Section 3.2 – An introduction to the mid-IR spectra of PNe and PPNe.

Section 3.3 – A description of the MIRAC2 camera that was used in this study.

Section 3.4 – The imaging technique and data reduction process.

Section 3.5 – The method of data analysis and modeling.

Section 3.6 – Our results on IRAS 22272+5435, IRAS 07134+1005, M 4–18, IC 5117 and OH 231.8+4.2. Dayal et al. (1997) provides a detailed study of IRAS 22272+5435 and IRAS 07134.

Section 3.7 – A summary of the main results from Chapter 3.

3.2. Introduction

The cool, dense circumstellar envelopes of AGB stars are very efficient centers for condensation of gas phase carbon, silicon and oxygen (and less abundant species like Fe, Mg, Ca) into solid grains. The condensed elements form grain nuclei; then, facilitated by the large densities in the envelope, grain growth occurs by accretion onto the nuclei. As the star evolves towards higher luminosities and mass loss rates, the increased dust formation eventually leads to the obscuration of the central star at optical wavelengths, and the star now appears as a bright infrared source. Dust plays a very important role in the physical and chemical evolution of an AGB star: Radiation pressure on dust grains (coupled with thermal pulses which levitate the atmosphere) drives the mass loss rate (Lafon and Berruyer 1991; Sedlmayr 1989; Knapp 1986). Dust grains act as catalysts and support a variety of grain-surface reactions (e.g. $2\text{H} \rightarrow \text{H}_2$; Tielens and Allamandola (1987)), and also play an important role in shielding molecules in the CSE from the interstellar and/or stellar radiation fields (e.g. Glassgold 1996). Furthermore dust is largely responsible for heating the gas in CSEs by exerting a viscous drag

on the gas molecules (Goldreich and Scoville 1976). The visible and/or UV stellar photons are scattered and absorbed by the dust and re-radiated in the infrared. As a star evolves on the AGB, the expansion of the photosphere causes a gradual dispersal and cooling of the dust shell. Thus, while the dust shells of AGB stars are characterized by color temperatures of 300–1000 K, the dust temperatures of PPNe and young PNe are generally lower, about 100–300 K (Kwok 1993; Zhang and Kwok 1990). At these temperatures, the continuum emission from the dust peaks in the mid-infrared (5–25 μ m). Imaging at mid-IR wavelengths is therefore a very effective means of tracing the warm dust shells around evolved stars at a high spatial resolution ($\leq 1''$). Our mid-IR images of dust continuum emission from a sample of PPNe and PNe provide detailed information on the structure and morphology of these objects (which is intricately related to the mass loss process). They allow us to estimate sizes and timescales (from the distance and the expansion velocity) and thereby place constraints on the evolutionary status of each object.

In addition to the strong continuum emission, there are also a number of spectral emission/absorption features associated with the dust at mid-IR wavelengths. Dust features are typically characteristic of vibrational transitions between atoms in the grains ($E_{vib} \sim 0.01$ – 0.1 eV), and therefore occur at wavelengths 10–100 μ m. In the gas phase, vibrational energy levels are split into rotational-vibrational bands; in solids however, rotation is suppressed and the characteristic P and R branches of the gas phase spectrum are replaced by broad, continuous solid state features (Whittet 1993). The observed features and their intensities depend on the composition and abundance of the dust and the excitation conditions in the CSE. The composition of the dust itself depends on the chemistry of the circumstellar envelope. The spectra of oxygen-rich stars ($C/O < 1$) are characterized by the 9.8 μ m and 18 μ m silicate features. The 9.8 μ m feature is seen

in emission in early AGB stars and appears as an absorption feature in the more evolved oxygen rich (OH/IR) stars and PPNe. The transition of this spectral feature, from emission to absorption, is due to an increased population of cooler, more extended silicate grains, and can be modeled by an increasing mass loss rate as the star ascends the AGB (Volk and Kwok 1988). The $18\mu\text{m}$ emission feature has been seen in the IRAS low resolution spectra (LRS) of many young PNe as well (Zhang and Kwok 1990). Mid-IR spectra of dust shells around carbon-rich ($\text{C/O} > 1$) evolved stars show evidence for amorphous carbon, graphite, SiC and larger hydrocarbons. Many evolved stars, PPNe and PNe show the SiC emission feature at $11.3\mu\text{m}$ (Chan and Kwok 1990; Aitken and Roche 1982). Also, there is the traditional family of infrared features called the UIR (unidentified infrared) features at 3.3, 6.6, 7.7, 8.6, 11.3 and $12.5\mu\text{m}$ which are seen in young PNe. There is strong evidence that these features are produced by UV-excited polycyclic aromatic hydrocarbons (PAHs), containing tens to hundreds of carbon atoms (Allamandola et al. 1989; Léger and Puget 1984; Duley and Williams 1981). Hrivnak et al. (1989) examined the IRAS LRS of PPNe candidates and discovered four sources with strong emission features at $21\mu\text{m}$. Subsequently, more sources have been found to have this $21\mu\text{m}$ feature (Kwok 1993). These “ $21\mu\text{m}$ ” sources do not show traditional PAH bands, but show several emission features between $7\text{--}13\mu\text{m}$ and $19\text{--}23\mu\text{m}$. The low-excitation central stars of these sources (F-K type) and the strengths of these features strongly suggest that their excitation is through visible photons (Buss et al. 1990). Though the carriers of these features have not been identified, their strength and association with carbon-rich environments (Guillois et al. 1996; Hrivnak 1995) strongly suggest that they originate from carbonaceous material. From our images of two such sources (IRAS 07134 and IRAS 22272) we are able to spatially isolate feature emission and get *estimates* for the abundances

of the feature carriers, under assumptions about their structure and composition (see Dayal et al. 1997).

3.3. The MIRAC2 Mid-Infrared Camera

MIRAC was the original mid-infrared camera for astronomy developed as a collaborative effort between the University of Arizona (U/A), the Smithsonian Astrophysical Observatory (SAO) and the Naval Research Laboratory (NRL). The camera used a Hughes 20×64 Si:As IBC focal plane array: it is described in detail elsewhere (Hoffmann et al. 1993, Hora 1991). In 1994, MIRAC was modified and the Hughes detector was replaced by a 128×128 Rockwell Si:As BIB array. The upgraded camera, with a significantly enhanced capability for astronomical observations, is called MIRAC2. MIRAC2 was developed, and is supported and operated by the MIRAC2 camera team: Dr. W. F. Hoffmann (U/A), Dr. J. L. Hora (University of Hawaii), Dr. G. G. Fazio (SAO), Dr. L. K. Deutsch (Boston University) and Aditya Dayal (U/A). I participated in various aspects of the camera upgrade with Dr. W. F. Hoffmann. I redesigned the camera optics to accommodate the Rockwell array and assisted with the installation and alignment of the optics in the dewar. I modified parts of the camera electronics, including the bias and preamplifier circuits and the controller board. I participated in the initial testing phase of the new detector and later in testing and debugging of the camera electronics.

3.3.1. Detector – A general description

MIRAC2 uses an arsenic-doped silicon (Si:As) Blocked Impurity Band (BIB) 128×128 , Hybrid Focal Plane Array (HFPA), serial number A9-38. The array was

developed by Rockwell International Corporation in Anaheim, CA. A summary of the camera parameters are presented in Table 3.1.

The principle of operation of BIB (or IBC) detectors is described by Szmulowicz and Madarsz (1987) and a more specific description of the Rockwell 128×128 array is given by Noel (1992). A BIB detector consists of a degenerately doped (conducting) Si substrate, a heavily doped infrared active layer (IRAL), an intrinsic Si blocking layer and a transparent electrical contact implant. (Figure 3.1). Each pixel is covered with an insulating layer of metal oxide, then a layer of aluminium metalization. A hole is etched in the oxide and indium "columns" are deposited to make electrical and mechanical connections between the contact implant, the aluminium and the multiplexer. The IRAL has a high concentration (N_d) of an n-type impurity like As and a smaller concentration (N_a) of a p-type dopant. The electron acceptors are fully compensated by the donors and are completely ionized; since $N_d \gg N_a$, however, there remain a considerable number of neutral donor atoms which have electrons associated with them. Due to the heavy concentration of impurity atoms electron "hopping" can occur within the impurity band, via vacant N_d^+ sites (which can be regarded as "holes"). When an electric field or bias is applied to the contacts (blocking layer positive relative to the conducting substrate) the impurity band electrons in the IRAL travel up to the blocking layer and the "holes" move in the opposite direction. The intrinsic blocking layer blocks conduction in the impurity band and prevents a large dark current from flowing through the detector in the absence of an incident flux on the detector. However, when a photon of sufficient energy (~ 0.1 eV) is absorbed in the IRAL, the electrons here are raised to the conduction bands. The electric field now drives them freely through the IRAL and the blocking layer to the top (positive) contact where they can be collected.

Table 3.1. Detector Characteristics

Material	Si:As
Wavelength Range	2–26 μm
Array Size	128 \times 128 pixels
Pixel Size	75 μm
Readout	16 parallel lines
Peak QE (λ)	0.42 (22 μm)
Well Depth	$3 \times 10^7 \text{ e}^-$

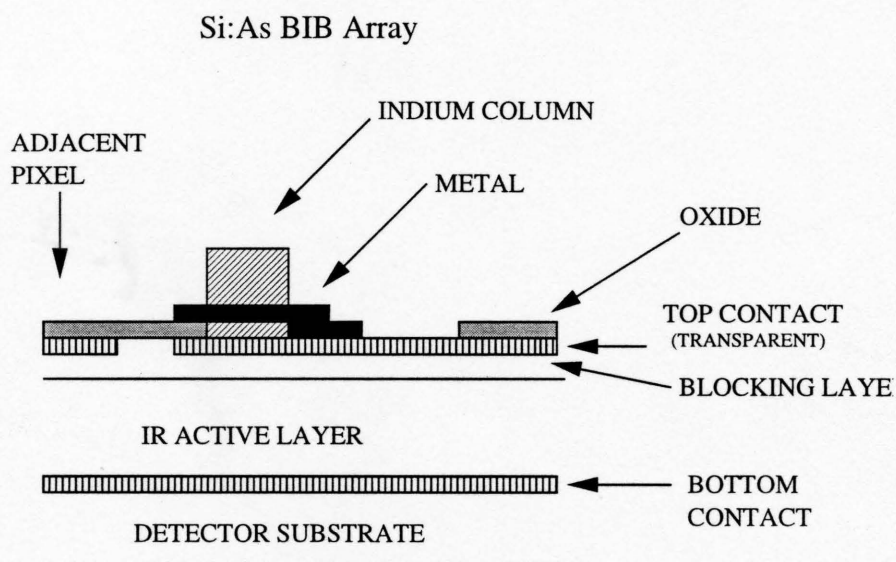


Figure 3.1 A schematic showing the cross-section of a arsenic-doped silicon blocked impurity band (BIB) array (adapted from Noel (1992), Rieke 1994).

The multiplexed readout mode of the array is shown in Figure 3.2. Pixels are grouped together in 2×8 blocks. The pixels of each block are read out simultaneously via 16 parallel readout lines. Blocks 1–16 form the left-most two columns of the array, blocks 17–32 the next two columns, and so forth. The blocks are read out sequentially, block 1 is read first and block 1024 is read out last. An important consequence of this multiplexer scheme is that a failure in any one of the readout channels does not eliminate a contiguous (1/16) region of the image. Instead, it appears as a “picket-fence” like pattern with the bad pixels spread out uniformly over the image.

3.3.2. Preamplifier

The preamplifier acts as the first stage in amplification for the signal coming from the detector. It consists of 5 IC boards, each of which has four identical circuits. (Only 16 of the 20 preamp circuits are used). There are 16 coaxial cables which connect the detector output (from the top of the dewar) to the preamplifier box situated at the top of the electronics box, adjacent to the dewar. The signal from the detector goes through two feedback op-amps. The first has a gain of 1 and simply acts as a buffer. The second op-amp has a gain of -4 . This gain is selected to provide a finer digitization of the array output (small Volts per Analog-to-Digital Unit, or V/ADU) and lower the digitization (toggle) noise. The mean detector response voltage is shown in Figure 3.3. The output voltage ranges from ~ 4.5 V at zero incident flux, to ~ 2 V at saturation. The linear maximum occurs when the output voltage is near 2.75 V. At higher flux levels, the detector pixels begin to get saturated. The output from the detector is sampled by a 12-bit A/D converter which has an input range of ± 2.5 V. With a high gain we are unable to sample the entire detector output range since the A/Ds sample only a

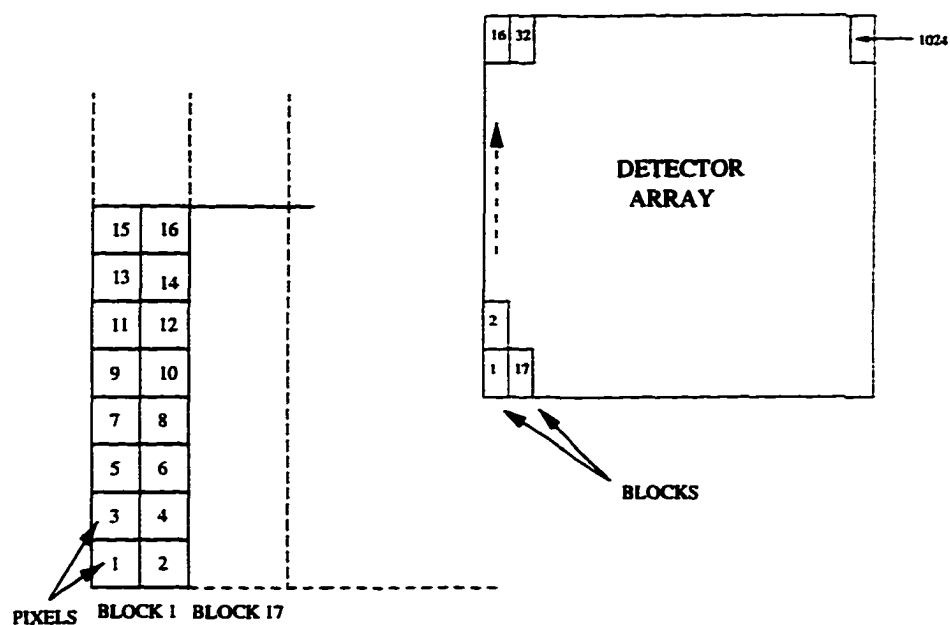


Figure 3.2 Readout scheme used by the Rockwell array multiplexer. Each block contains 16 pixels corresponding to the 16 parallel readout channels. In the above figure (left) each pixel in the block is labelled with the readout channel number. The block locations on the array are also shown in the figure (right). During each frame, the blocks are read out sequentially, from 1 to 1024.

range of 1.25 V on the detector: however our observations show that a range of 1.25 V covers most ($\geq 99.9\%$) of the pixels under normal illumination conditions. (Only about one dozen pixels out of 16,384 have a high dark current.) We have implemented a scheme that allows us to sample the detector output effectively, even under low-background flux levels (such as at $2.2\mu\text{m}$ – $4.8\mu\text{m}$) and very high background levels (e.g. when looking at the telescope dome for test purposes involving detector saturation). The preamp is designed so that the A/D samples a specified range of detector output, depending on the incident flux on the detector. The “level-of-flux” is specified in the MIRAC software program as High, Medium or Low. This information is encoded in two bits and sent to a preamplifier offset selector board. The output voltage from the preamplifier offset board is sent to the summing junction of the second amplifier. With an appropriate choice of series resistors, the mean output voltage from the array is kept centered in the A/D input range for a given level-of-flux. The Medium level provides background shot noise limited images over our usual ($\geq 8\mu\text{m}$) range of observations.

3.3.3. Optics

MIRAC2 uses the same optical design as MIRAC. The primary optical elements consist of a gold-coated flat mirror and a tilted, off-axis ellipsoid mirror. The beam from the telescope is deflected into the MIRAC2 dewar by a dichroic in the guider box (see Figure 3.4). The principal ray first strikes the flat mirror (tilted $\sim 35^\circ$ measured from a surface orthogonal to the incident beam) and is reflected towards the ellipsoid. It strikes the ellipsoid (off-axis) and gets reflected straight up. After passing through the pupil and the filter wheels it strikes the center of the array normal to its surface. The array is mounted on a moving stage which allows a continuous zoom magnification of 0.28 to 0.56. At the focus of the

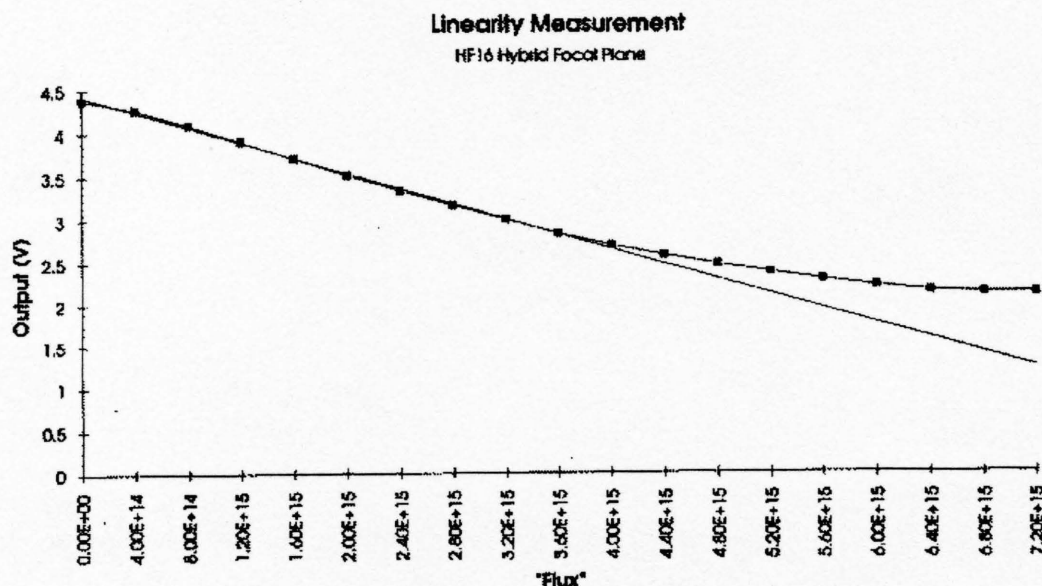


Figure 3.3 MIRAC2 array output voltage as a function of incident flux (courtesy Rockwell). The output voltage ranges from 4.5 V at zero flux to 2 V at saturation. Maximum linear voltage is ~ 2.5 V.

IRTF ($1.86''/\text{mm}$), this range of magnification yields a pixel scale of $0.5''/\text{pixel}$ – $0.25''/\text{pixel}$. The magnification is nominally set to yield a scale of $0.34''/\text{pixel}$, to allow for Nyquist sampling ($\lambda/2D$) of the diffraction-limited point spread function (PSF) at $10\mu\text{m}$. This gives a field-of-view of $44'' \times 44''$.

Due to the larger size of the new array in MIRAC2 we re-evaluated the optical design/elements of MIRAC and found that the same optical design, with slightly larger optical elements, could be used in MIRAC2. The larger mirrors (fabricated by Dick Sumner) were required to avoid vignetting of the field by the mirrors. A larger off-axis tilt was required to avoid the beam from the ellipsoid from hitting the flat. A new configuration requiring a more off-axis beam incidence on the ellipsoid, was found iteratively by changing the position/tilt of the flat, and pitch angle of the ellipsoid. The new configuration was constrained by the need to have: (a) the principal ray normal to the detector and (b) an unchanged linear separation

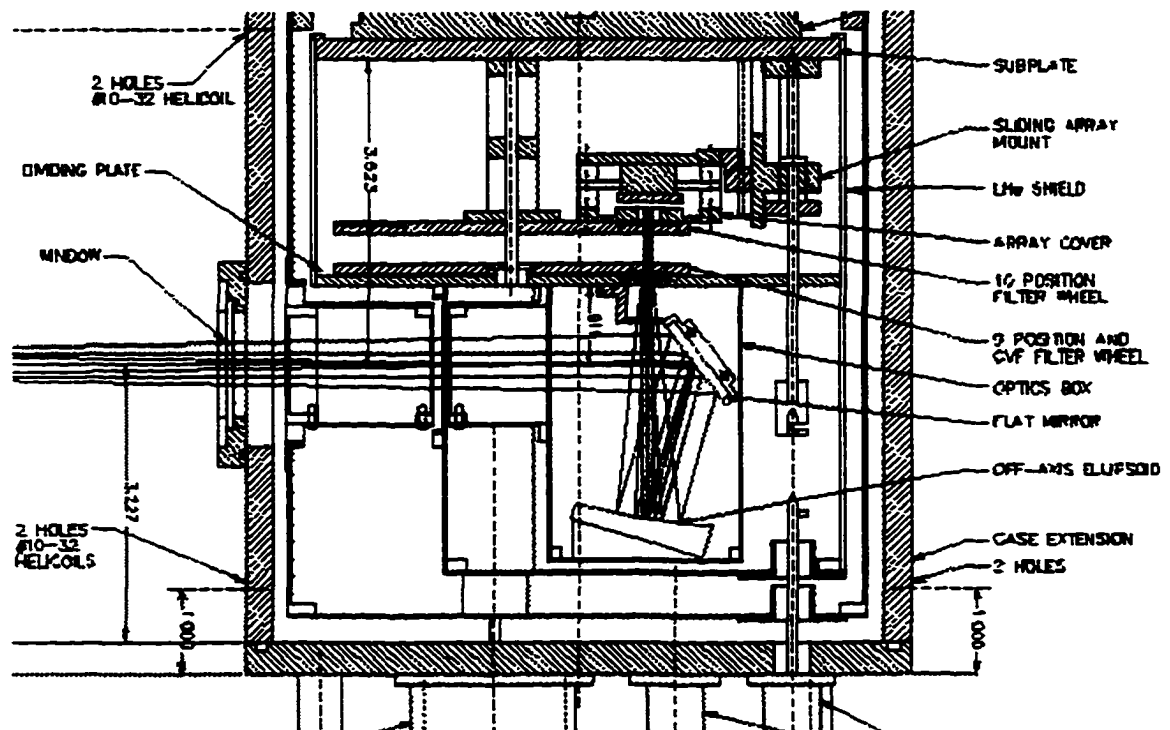


Figure 3.4 A schematic of part of the MIRAC/MIRAC2 cryostat, showing the optical path, the position of the flat and ellipsoid mirrors and the detector (Hora 1991).

between the detector and the ellipsoid–principal ray contact point (unchanged magnification). The ray–traced design was optimized to produce a minimum spot size (blur) at the edges of the array at the $f/37$ IRTF.

A more detailed description of MIRAC2, including current sensitivity estimates, filters, and the MIRAC camera PC programs can be found in the MIRAC2 users manual or on the MIRAC home page at: <http://www.ifa.hawaii.edu/~hora/mirac.html>.

3.4. Imaging and Data Reduction

3.4.1. Imaging

Ground–based astronomical observations at mid-IR wavelengths face a number of unique problems: (1) The mid-IR ($10\ \mu\text{m}$) corresponds to the wavelength of peak emission of a radiator at 300 K. Since this is very close to the equilibrium temperature of the earth’s surface (and the lower troposphere) mid-IR detectors are swamped with “background” radiation from the sky and the ground (including the telescope). Generally the background radiation is 10^3 – 10^5 times higher than the radiation from astronomical sources (see Section 3.4.3). (2) Some principal constituents of the atmosphere: CO_2 , Ozone, and H_2O have a number of strong absorption features between $1\ \mu\text{m}$ and $25\ \mu\text{m}$. The atmospheric transmission in these features is either very low or zero (Figure 3.5). Therefore a number of compromises must be made between scientific interests and feasibility. Generally filter sets have to be selected carefully, to avoid atmospheric features yet maximize the scientific returns. Since much of atmospheric attenuation is due to H_2O , the atmospheric transmission is considerably higher at dry and high–elevation sites like Mauna Kea.

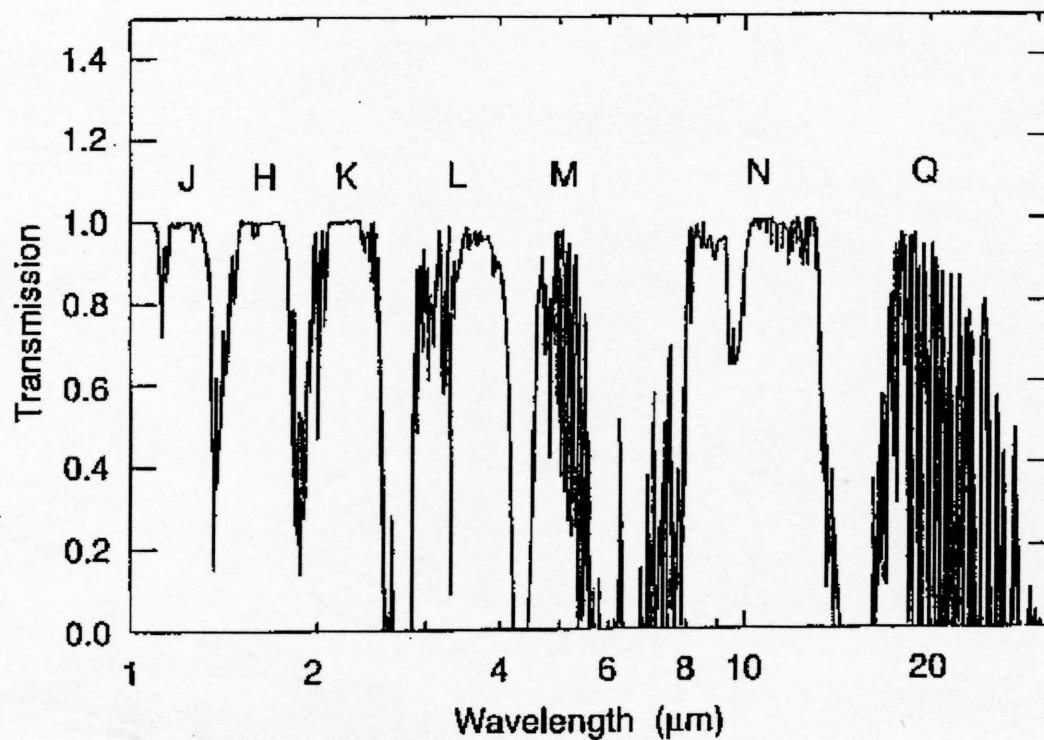


Figure 3.5 Atmospheric transmission curve from $1\mu\text{m}$ – $30\mu\text{m}$ (from Hanner and Tokunaga 1991). The absorption features are primarily due to atmospheric H_2O , CO_2 , O_3 and N_2O . Narrow absorption bands dominate the atmospheric opacity for $\lambda \geq 18\mu\text{m}$.

Since the mid-IR emission from the sky and telescope usually overwhelm the source signal, the sensitivity of our observations depend on the accuracy with which this background emission (which may be non-uniform over the array or temporally variable) can be removed. The background is removed by chopping the secondary mirror of the telescope at a frequency (typically 3–10 Hz) that is higher than the frequency of sky and detector fluctuations and moving the telescope (nodding) at a slower rate. During chopping, images of the source and images of blank sky are acquired in quick succession. A difference between the two sets of images removes most of the background emission, but leaves some residual (non-uniform) background emission which is the result of two different optical paths in the two chop beams. This residual background is removed by nodding the telescope once every ~ 10 s from the source to an off-source, blank sky position. This mode of observing is illustrated in Figure 3.6. Usually the nod direction is chosen to be orthogonal to the direction of chopping. At the end of each MIRAC2 “observation” four images are obtained and stored as a single image file: one chop pair for each of the two nod beams, with the source *usually* in one beam. The final background-subtracted image (that is displayed) is obtained by subtracting the off-source images from the on-source images, $I_{obs} = (I_1 - I_2) - (I_3 - I_4)$. Though the chop-nod mode subtracts out the background emission from the sky and telescope effectively, there is a large overhead ($\sim 75\%$) associated with this method since about three quarters of the total integration time is spent on blank sky. For observing the compact sources ($\sim 3\text{--}8''$) presented in this study we used smaller ($\sim 20''$) chop and nod throws, ensuring that the source was on the array in all four beams. In this mode we improve the signal to noise in our images by a factor of 2, in the same total integration time. Figure 3.7 shows an example of such an image. The source was first positioned in the N-W (top-right) quadrant

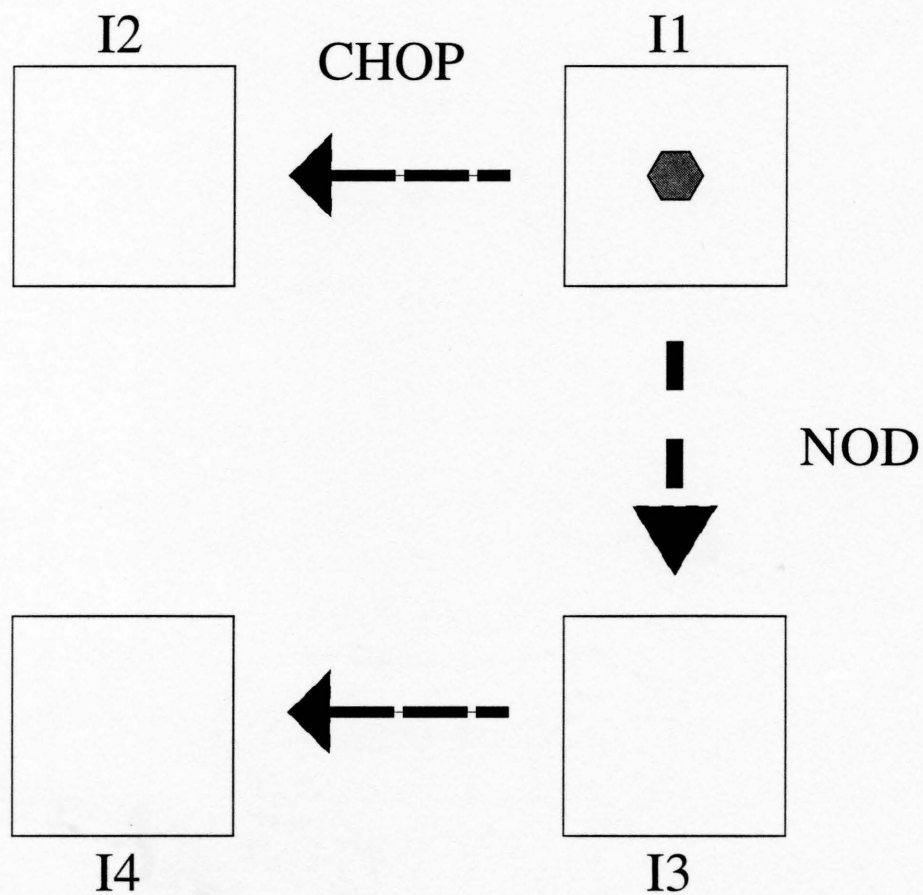
of the array. With a chop throw of 20" West and a nod of 20" North the source appeared in the N-E, S-W and S-E quadrants, in beams I_2 , I_3 and I_4 respectively. The subtraction of the off-source beams from the on-source beam produced the two "positive" sources and two "negative" sources that are seen in the final image, I_{obs} . This observational mode was used for all the sources (and standard stars) presented in this study.

3.4.2. Data Reduction and Calibration

Most of the observations presented here were made at the NASA Infrared Telescope Facility (IRTF), on Mauna Kea, Hawaii. Observations of IRAS 07134+1005 were made at the United Kingdom Infrared Telescope (UKIRT). The observations of each source were interspersed with frequent (every half hour or so) observations of a bright standard star in a nearby region of the sky, with the same observing parameters. The images, obtained in the MIRAC camera format, were converted into FITS and IRAF¹ during the data reduction process. During each night we obtained images of the dome and blank sky at various wavelengths. From these images we derived gain matrices for "flat-fielding" the images.

The individual pixels of an array are not identical. Each pixel has a slightly different offset level and a unique response or gain. These variations introduce a fixed-pattern noise on the array. The offsets are due to differences in DC voltage levels between pixels and between channel amplifier gains, and also due to

¹Image Reduction and Analysis Facility (IRAF) is distributed by the National Optical Astronomy Observatories which is operated by the Association of Universities for Research in Astronomy, Inc., under contract to the National Science Foundation.



$$I_{\text{obs}} = (I1 - I2) - (I3 - I4)$$

Figure 3.6 Chop-Nod data taking mode. The source is in beam I1. Here the chop is E-W and Nod is N-S.

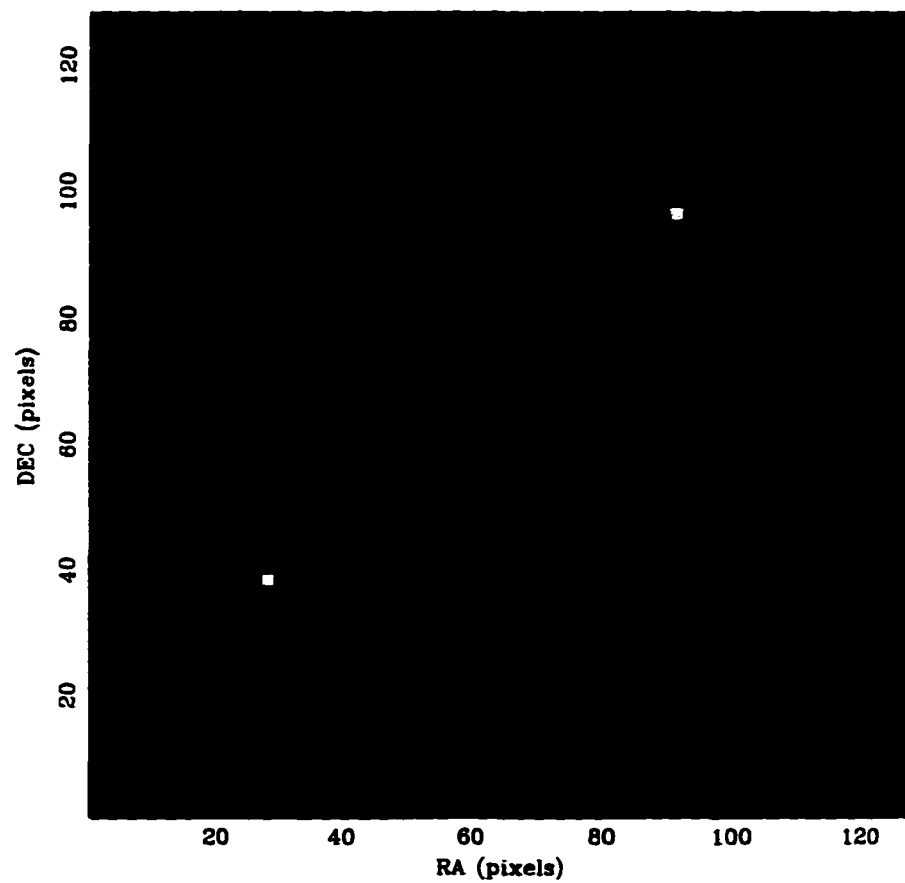


Figure 3.7 An unprocessed MIRAC2 image of the mid-IR standard star α -CMa taken at the IRTF with a 20" W Chop, and a 20" N Nod. The bright sources correspond to beams I_1 and I_4 , dark sources to beams I_2 and I_3 (see text). The array field-of-view is 44" \times 44".

differences in the dark current associated with each pixel. While the electronics offsets are independent of observing parameters, the charge associated with dark current is proportional to the frame time. The response variations may occur due to detector imperfections such as non-uniform doping etc. For obtaining useful images it is necessary to eliminate the fixed-pattern noise. The pixel offsets are removed during chopping and nodding, but chopping and nodding does not compensate for pixel-to-pixel gain variations across the array. To remove these variations we construct a multiplicative gain matrix. This gain matrix is typically made from 5-s “grabs” (images taken without chopping or nodding) at two different flux levels. (We explored a variety of alternatives to get two different illumination levels, but finally settled on a procedure where we observe blank sky at 1 airmass for the low flux level, and observe the inside of the dome for the higher flux level). A difference map between these two flux levels, is divided by the mean of the difference map (i.e. normalized to unity) and then inverted to get the gain matrix. This gain matrix is then applied to (multiplied by) the images. Our gain matrices show that all but about a dozen of the 16,384 pixels show gain variations $\leq \pm 10\%$ over the array.

Following application of the gain matrix and mask (to eliminate the ~ 12 high dark current pixels) the data are corrected for atmospheric extinction. The extinction factor (EF; magnitudes of extinction per airmass) can be related to the observed intensity of a source at a given airmass, $m_\lambda(A)$ and the intensity at zenith, ($m_\lambda(1)$) by the relation:

$$\begin{aligned} EF \times (A - 1) &= m_\lambda(A) - m_\lambda(1) \\ &= -2.5 \log I_\lambda(A) + 2.5 \log I_\lambda(1) \end{aligned}$$

$$\Rightarrow I_{\lambda}(1) = I_{\lambda}(A) 10^{\frac{BF \times (A-1)}{2.5}}$$

where $I_{\lambda}(A)$ is the observed image (in digital units) and $I_{\lambda}(1)$ is the airmass-corrected image. The extinction factor can be calculated from observations of a standard star over a large range in airmass, if the atmosphere is stable over the course of the observations. During most of the nights spent on these observations we did not observe any standard star over a large-enough airmass range. Furthermore the weather conditions (humidity and/or clouds) were generally quite variable on time-scales of 3–4 hrs during each night. Therefore rather than derive extinction factors from our data, we used the median extinction values from the UKIRT manual (Krisciunas et al. 1987). Our observations of the standard star were made frequently and generally with the standard star and source in close proximity ($\Delta \text{Airmass} \leq 0.3$). Hence our choice of extinction factors does not have a large effect on the calibration.

After airmass corrections, we used a cross-correlation routine (written by Dr. Joseph Hora) and standard IRAF routines to shift and coadd our images. Simply cross-correlating on one of the four sources in each image did not work very well. The chop and nod throws change by small amounts over time; thus each of the four “sources” on the array have slightly different shifts. We cross-correlated our images four times, each time optimizing it for one of the four beams. This method yielded four coadded images of the source, one for each beam. From each of these four images we extracted one optimized source image. Finally, we shifted and added these four source images to obtain our final image. The same procedure was followed for reducing images of the standard star. Having obtained final images of the source and the standard star, we calculated the total emission from the

standard star (in digital units, ADUs) and derived standard star flux densities (Jy) using magnitudes from Cohen et al. (1995), and the revised zero-magnitude flux densities of Cohen et al. 1992. The Jy/ADU factor that we obtained in this manner is defined as the *relative calibration*. It relates top-of-the-atmosphere flux densities to detector output. From this factor, $\left(\frac{Jy}{ADU}\right)_{rel}$, we calculated the flux-density of our sources and then compared our calibration to the IRAS 12 μ m flux density and/or the IRAS low resolution spectra (LRS). Our results generally agree with the IRAS values to within $\sim 10\%$.

3.4.3. Thermal background emission

In this section we compare the background emission from the sky and the telescope at 11.7 μ m and 20.6 μ m. First we calculate the expected intensities for the sky and the telescope (assuming T=273 K) and then compare them to our observed background intensities, to get estimates for the telescope and sky emissivity at the two wavelengths.

The specific intensity (or spectral radiance) of a black-body at temperature T in $W\ m^{-2}\ \mu m^{-1}\ sr^{-1}$ is given by Planck's Law:

$$I_{\lambda}(T) = \frac{C1}{\pi \lambda^5 (e^{\frac{C2}{\lambda T}} - 1)} \quad (3.1)$$

where $C1 = 3.74 \times 10^8\ W\ m^{-2}\ \mu m^4$, $C2 = 1.44 \times 10^4\ \mu m\ K$, λ is the wavelength in microns. The specific intensity can be converted into Jy arcsec $^{-2}$ (I_{ν}), using $I_{\nu} \approx I_{\lambda}(T) \times 7.83\ \lambda^2$, where λ is in microns. From Equation 3.1 we can calculate the thermal background emission ($I_{\nu,back}$) from the telescope and the sky (assuming T $\sim 273\ K$ for both) at 11.7 μ m and 20.6 μ m, and compare these with the observed background:

$$I_{\nu,back} \approx \epsilon_{tel} I_{tel} + \epsilon_{sky} I_{sky} \quad (3.2)$$

where ϵ_{tel} and ϵ_{sky} are the telescope and sky emissivities. Our data provide background counts (obtained by looking at blank sky) in digital units (ADUs) per pixel. These counts can be converted to Jy (at the detector) if the absolute sensitivity $\left(\frac{Jy}{ADU}\right)_{abs}$ is known. The absolute sensitivity can be calculated from the relative sensitivity, $\left(\frac{Jy}{ADU}\right)_{rel}$ (Section 3.4.2) and an estimate of the vertical optical depth of the atmosphere, τ , assuming that the atmosphere is homogeneous and isotropic:

$$\left(\frac{Jy}{ADU}\right)_{abs} \approx \left(\frac{Jy}{ADU}\right)_{rel} e^{-\tau}$$

where the optical depth is related to the extinction factor EF (Section 3.4.2) by the relation $\tau = \ln(10^{EF/2.5})$. We calculate $\tau_{11.7} \approx 0.1$, $\tau_{20.6} \approx 0.4$, assuming the extinction factors of Krisciunas et al. 1987 for the broad-band N and Q filters. At $11.7\mu m$ the atmospheric transmission is considerably better than the average transmission over the N band, for this broad band includes the broad telluric ozone feature. Thus $\tau_{11.7}$ is probably significantly lower than 0.1. Using Equation 3.1, for a blackbody at $T = 273$ K we calculate an intensity of $6500 \text{ Jy arcsec}^{-2}$ at $11.7\mu m$ and $8900 \text{ Jy arcsec}^{-2}$ at $20.6\mu m$.

From our data we measure a total background intensity of $1871 \text{ Jy arcsec}^{-2}$ at $11.7\mu m$ and $7400 \text{ Jy arcsec}^{-2}$ at $20.6\mu m$. The sky transmission at $11.7\mu m$ is ≥ 0.9 , therefore the sky emissivity ≤ 0.1 . Assuming that $\epsilon_{sky} \sim 0.1$ (which is almost certainly an upper limit), we derive (from Equation 3.2) that the emissivity of the telescope is ≈ 0.19 at $11.7\mu m$. (This estimate includes the emissivity of various MIRAC components as well, including the dichroic mirror and the dewar window. However, these components have significantly lower emissivities than the telescope). If we assume that the emissivity of the sky is much lower, say 0.01, then we obtain a telescope emissivity of 0.27. At $20.6\mu m$, we measure a significantly higher background of $\sim 7400 \text{ Jy arcsec}^{-2}$. If the emissivity of the telescope ϵ_{tel} $_{20.6}$

$= \epsilon_{tel\ 11.7} \sim 0.2$, then the telescope emission ($I_{tel} \epsilon_{tel}$) is ~ 1700 Jy arcsec $^{-2}$. The sky emissivity is then ≈ 0.64 (Equation 3.2).

Though the analysis presented here is based on a small part of our data (taken during one night), our results illustrate two basic aspects about mid-IR observing: (1) The sky emissivity is significantly higher at $20.6\mu\text{m}$, hence our longer wavelength data ($17\text{--}20\mu\text{m}$) are considerably more susceptible to poor atmospheric conditions than the $8\text{--}13\mu\text{m}$ data. (2) The background intensities (sky+telescope) are typically about $10^3\text{--}10^4$ times higher than the peak intensities of our sources (see Section 3.6).

3.5. Analysis and Modeling

3.5.1. Temperature, Optical Depth and Feature Maps

Once the source and standard star images have been reduced and calibrated, we can calculate the temperature from any two continuum images, after making an assumption about the spectral emissivity of the dust grains. Distinguishing between continuum and feature emission is, however, difficult due to the large number of spectral features in the mid-IR spectra of PPN and PN. We selected the continuum wavelengths by examining available mid-IR spectra of our sources and avoiding obvious spectral features.

The temperature of warm dust is calculated by relating the ratio of observed intensities ($I_{\nu 1}$, $I_{\nu 2}$) to the corresponding intensities derived in Jy arcsec $^{-2}$ from the Planck function (Equation 3.1) modified by the dust emissivity:

$$\frac{I_{\nu 1}}{I_{\nu 2}} = \frac{\exp(\frac{C_2}{\lambda_2 T}) - 1}{\exp(\frac{C_1}{\lambda_1 T}) - 1} \left(\frac{\lambda_2}{\lambda_1} \right)^{n+3} \quad (3.3)$$

The dust emissivity is assumed to follow a power law, λ^{-n} (Mathis 1990; Tielens

and Allamandola 1987; Hildebrand 1983) and $I_{\nu 1}$, $I_{\nu 2}$ are the image intensities in Jy arcsec^{-2} . Note that if there are regions of cooler dust surrounding the warm dust shell then the observed intensity ratio (left side of Equation 3.3) will be different from actual (emitted) intensity ratio, and Equation 3.3 will be modified by the optical depths of the cold dust, $\tau_{\lambda 1, cold}$, $\tau_{\lambda 2, cold}$:

$$\frac{I_{\nu 1}}{I_{\nu 2}} = \frac{\exp(\frac{C_2}{\lambda_2 T}) - 1}{\exp(\frac{C_1}{\lambda_1 T}) - 1} \left(\frac{\lambda_2}{\lambda_1} \right)^{n+3} \frac{e^{-\tau_{\lambda 1, cold}}}{e^{-\tau_{\lambda 2, cold}}} \quad (3.4)$$

In our analysis we assume that the optical depths of the cold dust at $10\mu\text{m}$ – $20\mu\text{m}$ are small, and can be ignored. Given the uncertainty in the dust composition (hence the spectral index of grain emissivity) and the distribution of the cold dust (which we do not see in the mid-IR) we believe this assumption is justified. Since the dust temperatures of PPNe and young PNe are $\leq 300 \text{ K}$, $C_2/\lambda T \gg 1$. Equation 3.3 can be re-written more simply as:

$$T \approx \frac{1.44 \times 10^4 \left[\frac{1}{\lambda_2} - \frac{1}{\lambda_1} \right]}{\ln \left[\left(\frac{I_{\nu 1}}{I_{\nu 2}} \right) \left(\frac{\lambda_1}{\lambda_2} \right)^{n+3} \right]} K \quad (3.5)$$

If the optical depth of the cold dust is non-negligible (and the cold grains have a similar power law emissivity as the warm grains) our average temperature will be somewhat lower than the actual temperature; nevertheless it would still be an accurate representation of the relative location of hotter and cooler regions in the nebula.

Once we have obtained the temperature map we can calculate a map of the optical depth, assuming that the nebula is isothermal and that the grain properties are the same at each point along any line of sight. The observed specific intensity I_ν of such a nebula is related to the temperature of the dust (T), optical depth of warm dust (τ_{warm}) and optical depth of cooler, foreground dust (τ_{cold}) by the

equation:

$$I_\nu = (1 - e^{-\tau_{warm}}) B_\nu(T) e^{-\tau_{cold}} \quad (3.6)$$

Since absorption by dust grains is the dominant mechanism for extinction of starlight in the 10–20 μ m region, $\tau \propto Q$, the absorption efficiency. By using the Planck function and the temperature derived from Equation 3.5. and rearranging Equation 3.6, we can calculate the optical depth (τ_{warm}) at λ_3 from:

$$\tau_{\lambda_3} = -\ln \left(1 - \frac{I_{\nu 3}}{B_\nu(T)} \right) \quad (3.7)$$

where $I_{\nu 3}$ is the observed intensity (Jy arcsec⁻²) at λ_3 . Once again this calculation assumes negligible extinction by cold dust along the line of sight to the nebula.

The temperature map can also be used, along with a continuum image, to derive a map of the continuum intensity at another wavelength which has an emission feature. Next, we can subtract the continuum map from the observed (feature+continuum emission) image and then divide the subtracted image by the continuum map to obtain a map of the feature-to-continuum ratio. We have constructed such ratio maps for IRAS 22272 and IRAS 07134, and used them to derive abundance estimates for the carriers of the 11.7 μ m and 20.6 μ m features (see Dayal et al. 1997). All the calculations described in this section were carried out with scripts utilizing IRAF tasks, after the (calibrated) images had been registered (using a cross-correlation routine) and convolved to the same resolution.

3.5.2. Geometrical Modeling

Mid-IR images of most PNe and PPNe show that their morphologies are inconsistent with the simplest expected structure: a spherical, uniformly expanding dust photosphere surrounding the central star. Our mid-IR images of IRAS 07134 suggest a resolved bipolar morphology. The images of IRAS 22272 show that at

8.8 μ m and 11.7 μ m the inner core is elliptical; at the same time the outer contours are somewhat rectangular and show definite deviations from circular symmetry. The morphologies of both objects suggest that the dust distribution resembles a cylindrical or toroidal shell surrounding the central star; the bipolar lobes are created by higher column densities of dust along the walls of the cylindrical shell. This increased equatorial emission may represent a higher equatorial temperature and/or dust density. Using these observations as our motivation, we have constructed geometrically simple, optically thin axially symmetric models which fit the observed mid-infrared morphology, as well as the mid- and far-infrared flux densities of the two PPNe. We believe that similar models can also be applied to OH 231.8, M 4-18 and IC 5117 (Section 3.6). A detailed study and application of this model to IRAS 07134 and IRAS 22272 is presented in Dayal et al. (1997).

For our models, we assume that the central star is surrounded by two dust components: a warm dust component represented by a cylindrical shell, which is responsible for most of the observed mid-IR emission; and a cooler, more extended spherical dust shell which produces most of the far-infrared luminosity. A schematic of the model geometry is shown in Figure 3.8. The cylindrical shell is specified in terms of an inner and outer radius (R_1 , R_2) and height (H). The extent of the spherical shell is defined by the inner radius, R_{in} and the outer radius, R_{out} . For our earliest models we have assumed that $R_1 = R_{in}$, i.e. there is an inner, dust-free cavity devoid of warm or cold dust. A three dimensional model of the nebula is constructed in cartesian coordinates using a grid size of 32^3 cells, where each cell represents the pixel size (in arcseconds) of the observations. The inner and outer radii (and height) of the shells are specified in arcseconds. The nebula consists of dust grains that are identical in size and emissivity. The number density of the dust grains in each cell follows a power law of the form, $\rho(r) = \rho_0 \left(\frac{r_0}{r}\right)^d$ (where

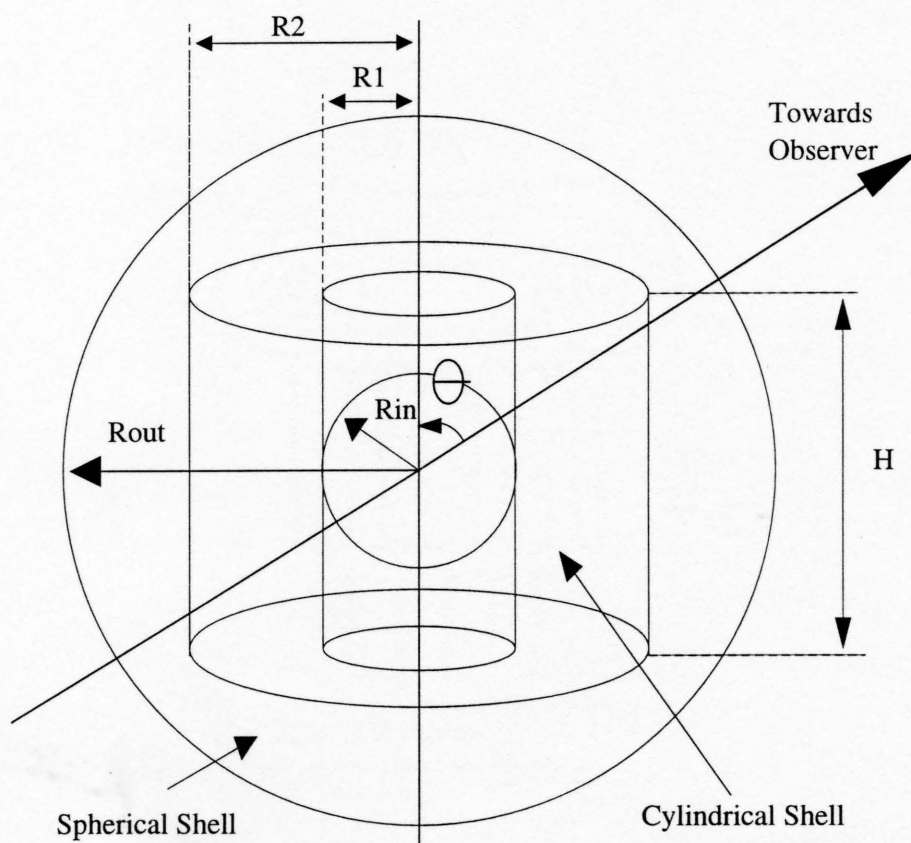


Figure 3.8 A schematic of the optically thin model geometry. Warm dust (that dominates the mid-IR emission) lies in a cylindrical shell. Cooler dust lies in a spherical, more spatially extended shell. See text for details.

$1 \leq d \leq 2$). The density at the innermost radius is a function of the total mass and extent of the nebula and can be calculated separately for the spherical and cylindrical dust components (ρ_{0s} and ρ_{0c}):

$$\rho_{0s} = \frac{N_{sph}}{4\pi r_0^d \int_{R_1}^{R_2} \frac{r^2}{r^d} dr} (sphere)$$

$$\rho_{0c} = \frac{N_{cyl}}{2\pi H r_0^d \int_{R_1}^{R_2} \frac{r}{r^d} dr} (cylinder)$$

Here, N_{sph} and N_{cyl} are the total number of grains in each of the two dust components, specified by the ratio of the total mass in each component to the mass of an individual grain. The emission from each grain at a given wavelength, $I_{gr} \approx \epsilon_{gr} B_\nu(T) \Omega_{gr}$, where ϵ_{gr} is the grain emissivity, $B_\nu(T)$ is the Planck function and Ω_{gr} is the solid angle subtended by the grain. The total emission from each cell is obtained by summing ϵ_{gr} over both dust components. Our calculation is identical to the method proposed by Hildebrand 1983, to infer the masses of optically thin dust clouds from submillimeter observations. Our model allows for changing the orientation of the source both *in* the plane of the sky by an angle α , and *out* of the plane of the sky towards the observer by an angle θ . Under these two rotations, a point in the rotated frame $P'(x', y', z')$ is related to a point in the un-rotated frame $P(x, y, z)$ (where the $+y$ axis points north, $+z$ points towards observer) by the transformation:

$$\begin{pmatrix} x' \\ y' \\ z' \end{pmatrix} = \begin{pmatrix} \cos\alpha & -\sin\alpha & 0 \\ \sin\alpha \cos\theta & \cos\alpha \cos\theta & -\sin\theta \\ \sin\alpha \sin\theta & \sin\theta \cos\alpha & \cos\theta \end{pmatrix} \begin{pmatrix} x \\ y \\ z \end{pmatrix}$$

If the emission is optically thin (as shown by our results, Section 3.6), the model surface brightness is calculated by summing the emission at each cell in the $x - y$ plane along the line of sight (z -axis), $B(x, y) = \sum_z I(x', y', z')$, where $I(x', y', z')$ is the intensity of emission per cell. The model images obtained in this way are then convolved with a gaussian PSF representing the FWHM (full-width at half-maximum) of the standard star. The inclination of the cylindrical shell towards the observer (θ) determines the ellipticity of the nebula, and limb brightening along lines of sight through the walls of the cylinder create bipolar emission lobes. The inner and outer radii (R_{in} and R_{out}) of the cylinder determine the width and separation of the lobes. Though the model images allow us to determine the geometry of the sources, model spectra (derived by integrating fluxes over the images, at multiple wavelengths) are more useful as diagnostics for constraining the temperatures and relative masses of the dust shells. For details of the model as applied to IRAS 07134 and IRAS 22272, the reader is referred to Dayal et al. (1997).

3.6. Results

In the last few years rapid improvements in mid-IR detector technology, leading to larger format arrays with smaller pixels, have allowed (near) diffraction limited imaging of a number of PPNe and PNe. However, so far still a relatively small number (\sim few tens) of PPNe and young PNe have been directly resolved at mid-IR wavelengths (e.g. Hora et al. 1996, 1993, 1991; Meixner et al. 1997; Meixner 1993). One reason for this is that many PPNe and young PNe (except the sources that are close-by, ≤ 1 kpc) are generally compact and not more than $1-2''$ (FWHM). The images presented here cover the wavelength range of $8-21\mu\text{m}$;

they have high sensitivity and spatial resolution ($\leq 1''$ at $10\mu\text{m}$) but also provide Nyquist sampling of the diffraction point spread function (PSF). Adequate spatial sampling is important for preserving spatial information while shifting/adding images, during convolution/deconvolution of the PSF and in constructing accurate maps of temperature, optical depth and for isolating feature emission. All the images presented here were obtained with the MIRAC2 camera in the observing mode described earlier (Section 3.4.2).

3.6.1. IRAS 22272+5435 and IRAS 07134+1005

In Dayal et al. (1997) we present mid-infrared images of 2 carbon-rich ($\text{C/O} > 1$) PPNe, IRAS 07134+1005 and IRAS 22272+5435, which were identified by Kwok, Volk & Hrivnak (1989) as having a prominent $21\mu\text{m}$ emission feature in their IRAS Low Resolution Spectra (LRS). Their mid-IR spectra (Justtanont et al. 1996, Buss et al. 1990) show that both of these sources have several emission features between $7\text{--}13\mu\text{m}$, superposed on broad emission plateaus. These features differ from the traditional unidentified (UIR) features ascribed to polycyclic aromatic hydrocarbons (PAHs; Léger and Puget 1984, Allamandola et al. 1989). These emission bands can, however, be fit by laboratory spectra of various carbonaceous compounds, including simple PAH molecules (Justtanont et al. 1996) and coal grains (Guillois et al. 1996). Our $11.7\mu\text{m}$ image samples emission from the $11.5\mu\text{m}$ and $12.2\mu\text{m}$ emission bands, as well as the $11\text{--}13\mu\text{m}$ emission plateau. IRAS 22272 and IRAS 07134 also show the broad, unidentified “ $21\mu\text{m}$ feature”. Though the carrier of this feature has not been identified, there is ample evidence for the carbon-rich nature of these sources (Bakker et al. 1996, Hrivnak 1995), and it is reasonable to assume that carbonaceous material may also be responsible for the $21\mu\text{m}$ emission feature. The $20.6\mu\text{m}$ broad-band image samples emission from

this broad $21\mu\text{m}$ feature. We use our $11.7\mu\text{m}$ and $20.6\mu\text{m}$ images and others, which sample the dust continuum, to obtain temperature and optical depth maps, as well as maps of the feature-to-continuum ratio. From these “ratio” maps we estimate carrier abundances, under the assumption that they are PAH-like molecules containing ~ 100 carbon atoms. We find that the feature emitters are not distributed uniformly over the nebula. In the case of both IRAS 22272 and IRAS 07134 our ratio maps show significant variations over the surface of the nebula and show that the peak emission is displaced from the center of the nebula. This result suggests that the feature emitters are preferentially destroyed by the stellar radiation field at the nebula center. A similar paucity of feature emitters towards the center of the nebula is seen in the $11.2\mu\text{m}$ UIR feature maps of the young PN AFGL 915 (Hora et al. 1996).

We also model both sources using the axially symmetric code described in Section 3.5.2, using emissivities for spherical graphite grains (Draine and Lee 1984). We find that cylindrical shells of warm ($T \approx 190\text{K}$) dust provide good fits to our images. However, an additional component of cooler dust containing about 80% to 90% of the total dust mass is required to fit the mid- and far-infrared spectra of both sources. A detailed description of the model parameters and results is presented in Dayal et al. (1997).

3.6.2. M 4-18

Images and analysis

This is a young, low excitation temperature PNe ($T_e \approx 5600$). The optical spectrum shows lines of C^{2+} and C^{3+} (Goodrich and Dahari (1985)); the IRAS LRS of M 4-18 (Figure 3.9) shows a flat spectrum with a possible weak $11.3\mu\text{m}$

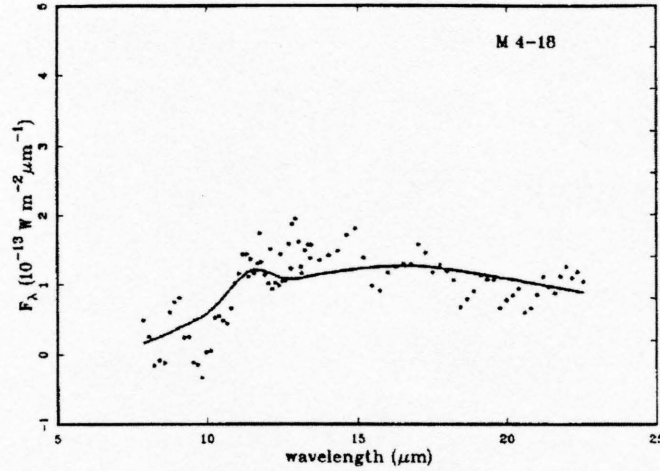


Figure 3.9 IRAS Low Resolution Spectra of M 4-18 – The dots represent IRAS measurements. The solid line is a model fit from Zhang and Kwok 1990.

SiC feature (Zhang and Kwok 1990). Both suggest that the source is carbon-rich. Zhang and Kwok fit the mid- and far-IR spectrum of M 4-18 with a model that includes graphite and SiC grains, and calculate a dust temperature of 229 K. Our mid-IR images show an extended, elliptical warm dust shell with bipolar (east-west) lobes. The shell is $\sim 5.5'' \times 4''$ (full-width) at the 10% contour level at $11.7\mu\text{m}$. Both the $11.7\mu\text{m}$ and the $12.5\mu\text{m}$ images clearly show a central cavity where, presumably, the grains have been destroyed by the stellar radiation field. The $8.8\mu\text{m}$ image does not show evidence for a central minimum; instead there appears to be an emission peak which corresponds closely with the central minimum in the $11.7\mu\text{m}$ and $12.5\mu\text{m}$ images. The emission peak suggests a possible contribution from the central star. In fact, for a central star with a temperature of 2.2×10^4 K (Surendiranath and Rao 1995; Goodrich and Dahari (1985)), the ratio of specific intensities (in Jy arcsec^{-2}), $\frac{I_{s8.8}}{I_{s11.7}} \approx \frac{11.7^2}{8.8^2} \approx 1.8$. Furthermore, the ratio of specific intensities of warm ($T \approx 200$ K) dust, yield $\frac{I_{d8.8}}{I_{d11.7}} \approx 0.6$. Therefore at $8.8\mu\text{m}$, the central star is roughly 3 times stronger relative to the warm dust

continuum, than at $11.7\mu\text{m}$. However, the S/N in the $8.8\mu\text{m}$ image is considerably lower than the $11.7\mu\text{m}$ and $12.5\mu\text{m}$ images, so the $8.8\mu\text{m}$ image should be treated with caution. From the integrated flux densities in our $8.8\mu\text{m}$ and $12.5\mu\text{m}$ images (both of which sample dust continuum emission) we derive a dust temperature of ~ 215 K, for a λ^{-1} emissivity law. Since the signal-to-noise in the $8.8\mu\text{m}$ and $9.8\mu\text{m}$ images is quite low, we do not derive a temperature map here. From the inner radius of the dust shell ($R_{\text{in}} \approx 0.25''$) and assuming a typical AGB expansion velocity of $\sim 10\text{km s}^{-1}$, we estimate a dynamical age of $\sim 4,000$ yr for an assumed distance of 3.5 kpc (Goodrich and Dahari (1985)).

Discussion

In the radio continuum at 5 GHz, which traces free-free emission from ionized gas, M 4-18 appears to be a compact, low surface-brightness, bipolar nebula (Aaquist and Kwok 1990). The nebula is almost spherical but the emission peaks in the north and south lobes (Figure 3.11); thus the bipolar lobes in the continuum maps delineate regions of highest electron density ($S_\nu \sim n_e^2$), if the emission at 5 GHz is optically thin (Garay, Gathier and Rodriguez 1989). A comparison with the warm dust emission then suggests a simple model for the source morphology, that is very similar to the model adopted for the PPNe IRAS 07134 and IRAS 22272: The warm dust is concentrated in the equatorial plane, marked by the major axis of the elliptical dust shell. The bright lobes (see Figure 3.12) represent regions of high dust column densities along the walls of the toroidal (or cylindrical) dust shell. The Lyman continuum photons escape preferentially along the lower density polar regions and create the lobes of ionized gas seen in the radio continuum images.

Previous attempts to detect CO in M 4-18 have been unsuccessful (Dayal

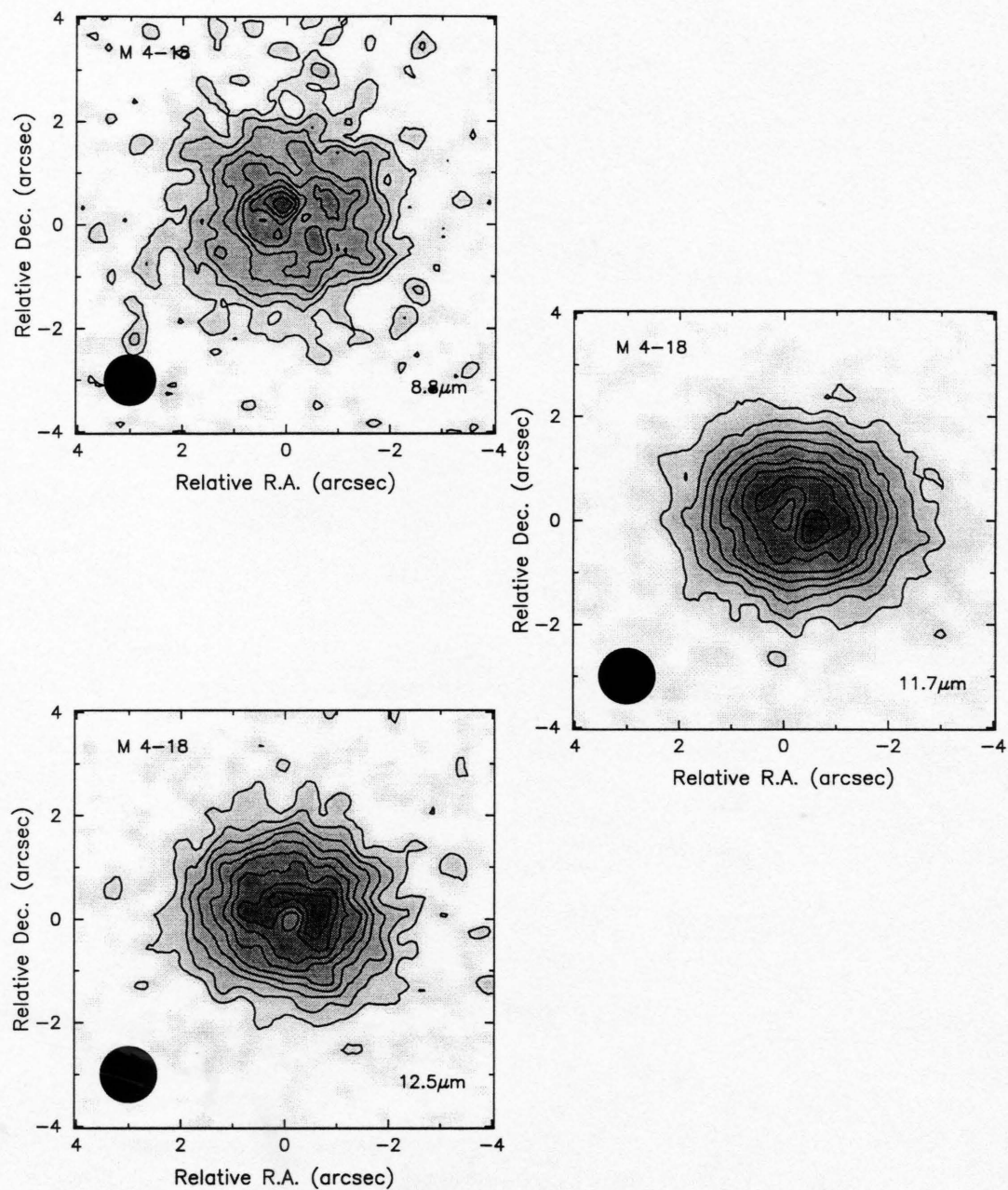


Figure 3.10 M 4-18 MIRAC2 Images taken at the IRTF. The contour interval is 10% of the peak. Peak emission is $0.32 \text{ Jy arcsec}^{-2}$ at $8.8 \mu\text{m}$, $0.6 \text{ Jy arcsec}^{-2}$ at $11.7 \mu\text{m}$ and $0.67 \text{ Jy arcsec}^{-2}$ at $12.5 \mu\text{m}$.

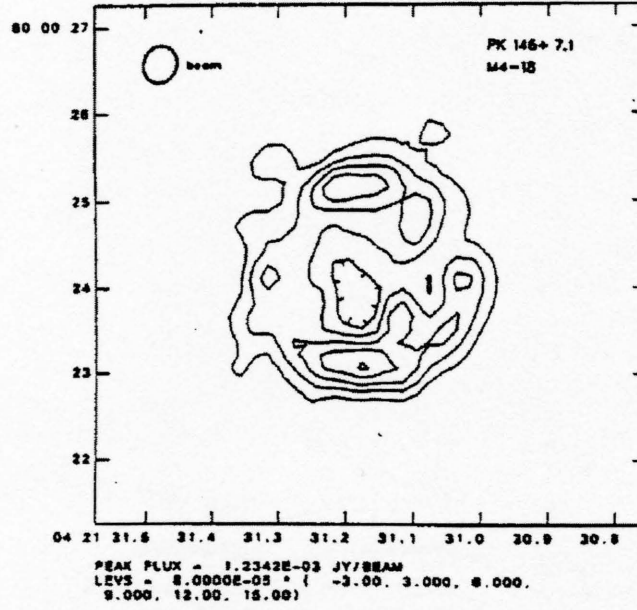


Figure 3.11 VLA 5 GHz radio continuum map of M-18 (Aaquist and Kwok 1990).

and Bieging 1996; Huggins and Healy (1989)). From our 12-meter observations (Dayal and Bieging 1996) we obtained an upper limit to the total molecular mass, $M_{mol} \leq 1.2 \times 10^{-3} M_{\odot}$ (at 3.5 kpc). The absence of molecular gas (in spite of a substantial dust envelope) suggests that the evolution of the central star is relatively slow, i.e. the timescale for evolution of the central star (τ_{ev}) is larger than the CO photodissociation timescale (τ_{ph}). Both, large τ_{ev} and a small τ_{ph} , indicate that the progenitor of M 4-18 is a low-mass star ($\leq 1 M_{\odot}$). We calculate the total dust mass of M 4-18 using the IRAS $60\mu\text{m}$ flux density, $F_{60}=3.5$ Jy (Zhang and Kwok 1990), and our derived dust temperature, T_d , from the formula given by Hildebrand 1983:

$$M_d = \frac{4apd^2 F_{\nu}}{3QB_{\nu}(T_d)} \quad (3.8)$$

where Q is the absorption efficiency, a is the grain radius and ρ is the grain density. We assume that $a\rho/Q \sim 0.013 \text{ gm cm}^{-2}$, which is consistent with a

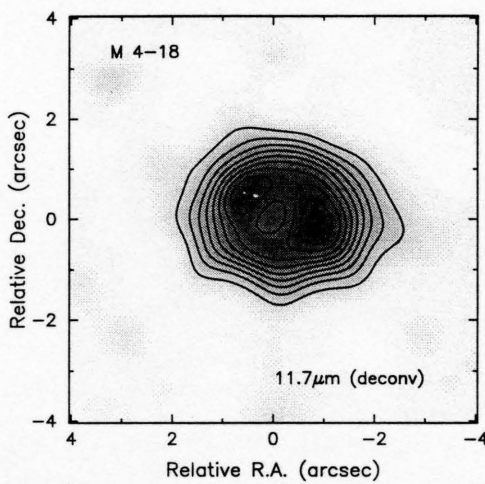


Figure 3.12 M 4-18 11.7 μ m images deconvolved using the Lucy-Richardson algorithm. The image shows the E-W bipolar lobes more clearly.

graphite composition (Draine and Lee 1984), and calculate a total dust mass of $\sim 4 \times 10^{-5} M_{\odot}$ for an assumed distance of 3.5 kpc. Though this simple calculation only provides an estimate for the total mass (as it assumes an isothermal nebula and a uniform dust composition), it does indicate that M 4-18 has a low mass circumstellar dust shell that is consistent with the non-detection of molecular gas. It is worth noting that though nebulae with bipolar or clumpy circumstellar envelopes are generally associated with larger condensations of molecular gas (e.g. Huggins et al. 1996), M 4-18 does not have a substantial molecular envelope. The slow evolutionary timescale (or low mass) also suggests that the cause of bipolarity in M 4-18 is probably not due to binary (common envelope) evolution. Here, the bipolar lobes may have been created by a low mass, rotating central star.

3.6.3. IC 5117

Images and analysis

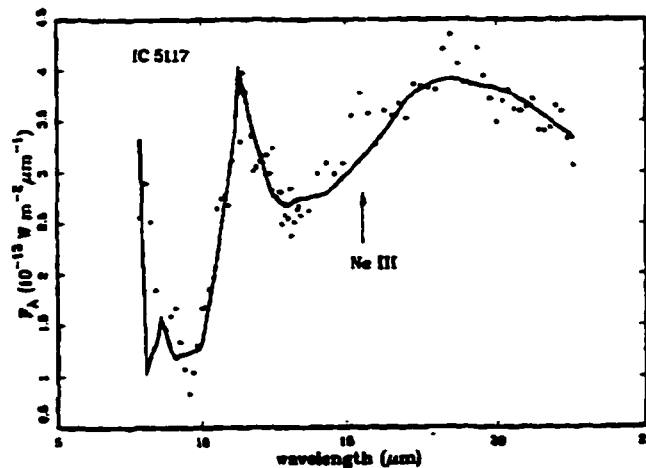


Figure 3.13 IRAS low resolution spectrum (LRS) of IC 5117. The solid line shows a dust model fit of Zhang and Kwok 1990. The model requires a SiC/UIR composition as well as a population of cool silicate grains to match the $11.3\mu\text{m}$ features and the $18\mu\text{m}$ “bump”.

IC 5117 is a bright mid- and far-infrared source; its IRAS LRS (Figure 3.13) shows a strong emission feature between 11–12 μm and a broader feature that peaks between 18–20 μm . There is also a weaker emission feature at 8.6 μm . Zhang and Kwok (1991) find that the spectrum can be fit with a composition that includes silicates, SiC as well as PAH-like carriers which produce the 8.6 μm and 11.3 μm UIR emission bands. Silicates reproduce the 18 μm bump in the spectrum, while SiC is needed to match the width and peak intensity of the broad 11–12 μm feature. Their results suggest that IC 5117 has a mixed carbon-oxygen chemistry and a dust temperature of 189 K. Our images show an elliptical shape, $\sim 2.5'' \times 3.5''$. The warmest dust, traced by the 8.8 μm image, appears to be somewhat more strongly confined along the major axis than at 11.7 μm or 12.5 μm . The 17.8 μm and 20.6 μm images show a somewhat more extended emission, with more circular inner intensity contours. However, this difference may be due to the larger PSF (point spread function) at these wavelengths. From the LRS spectrum it is difficult to estimate the continuum emission level for $\lambda > 13\mu\text{m}$; however, we assume that our 20.6 μm image samples mostly continuum emission while the 17.8 μm image contains silicate emission. Using the 20.6 μm and the 8.8 μm images, we construct a map of the dust temperature and an optical depth map at 11.7 μm (refer to Figure 3.17). The temperature map shows that the peak temperature is about 225 K (assuming a grain emissivity, $\epsilon \sim \lambda^{-1}$) and the distribution of the peaks is bipolar, along the major axis of the nebula. It is interesting to note that ratioing either the 8.8 μm or the 11.7 μm images with those at 17.8 μm or 20.6 μm yields color temperature maps that show bipolar temperature peaks, separated by about $2''$ along the major axis of the nebula.

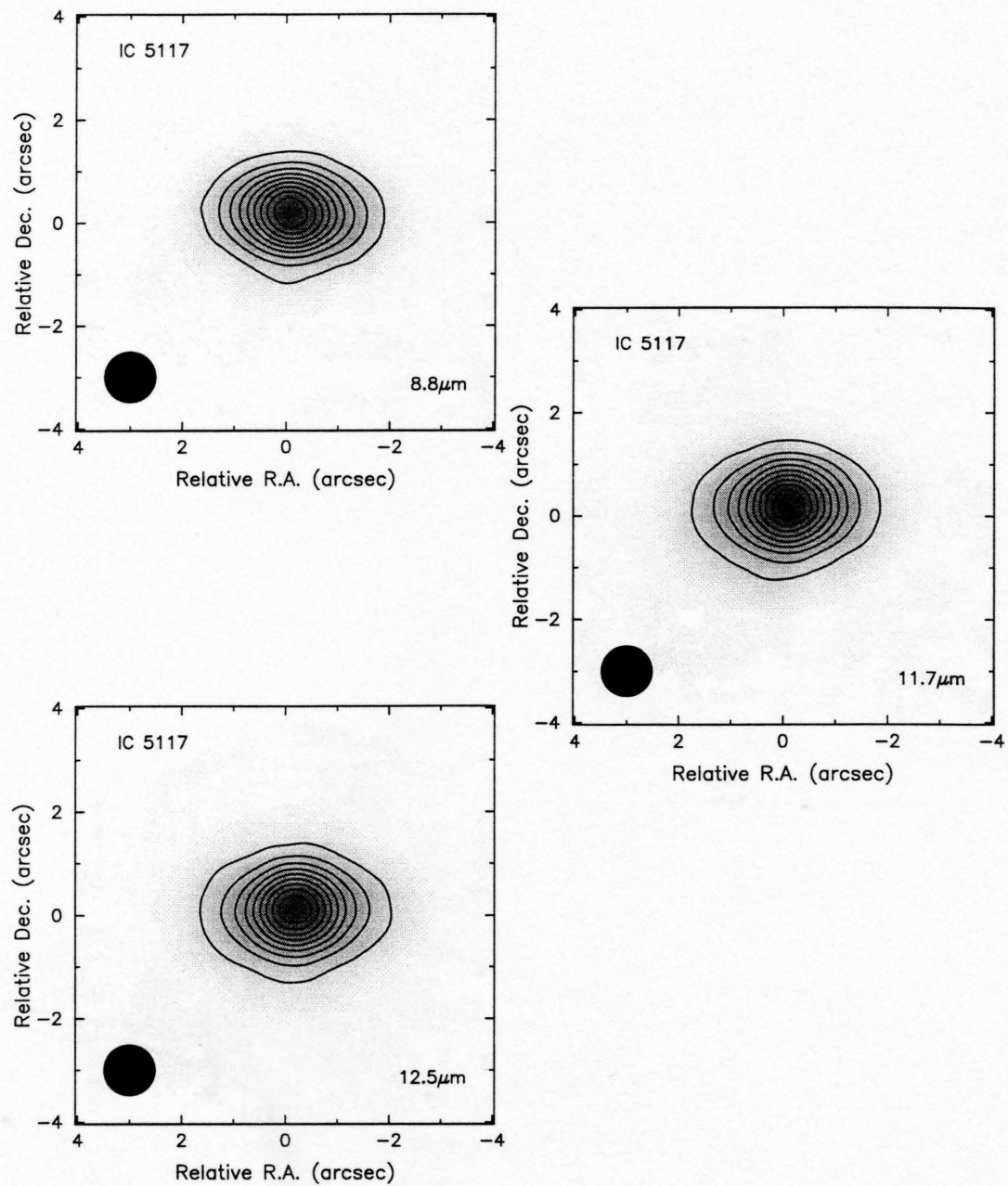


Figure 3.14 IC 5117 MIRAC2 Images taken at the IRTF. The contour interval is 10% of the peak. Peak emission is $2.27 \text{ Jy arcsec}^{-2}$ at $8.8\mu\text{m}$, $4.6 \text{ Jy arcsec}^{-2}$ at $11.7\mu\text{m}$ and $4.2 \text{ Jy arcsec}^{-2}$ at $12.5\mu\text{m}$.

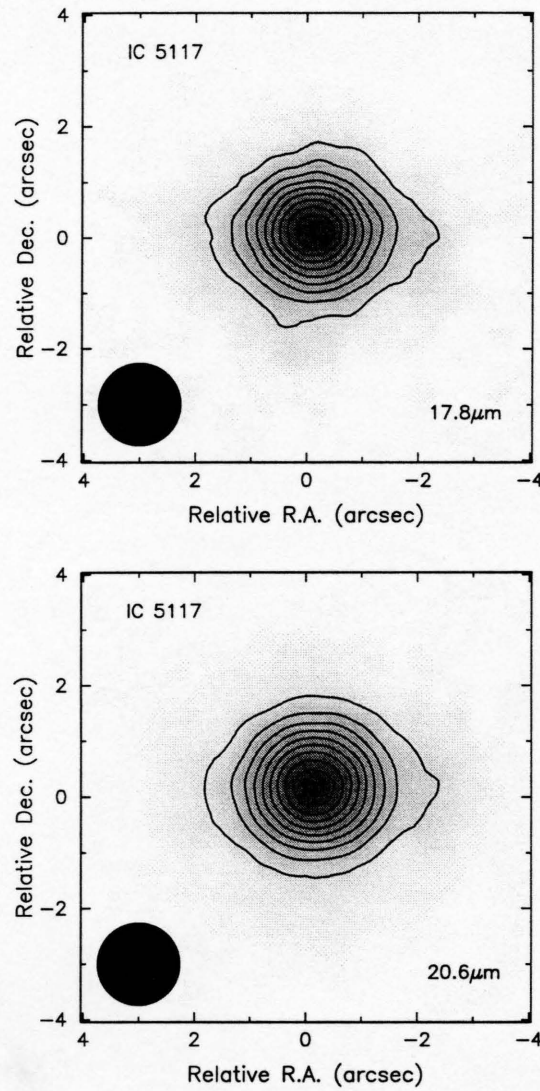


Figure 3.15 IC 5117 MIRAC2 images taken at the IRTF. The contour interval is 10% of the peak emission, which is $9.6 \text{ Jy arcsec}^{-2}$ at $17.8\mu\text{m}$ and $10.2 \text{ Jy arcsec}^{-2}$ at $20.6\mu\text{m}$.

Discussion

IC 5117 is compact and has a high radio surface-brightness. It has a medium excitation central star, $T_{star} \approx 80,000$ K (Sabbadin 1986). High resolution ($\theta_{res} \sim 0.1''$) radio continuum images of Aaquist and Kwok (1991) show that the structure of the nebula is very similar to the shape and structure seen in the mid-IR images; it is elliptical, with a extent of $\sim 4'' \times 2.5''$ (PA 100°) at the 10% contour level (see Figure 3.16). The radio continuum image shows a well-resolved inner core with bipolar lobes along the minor axis of the nebula.

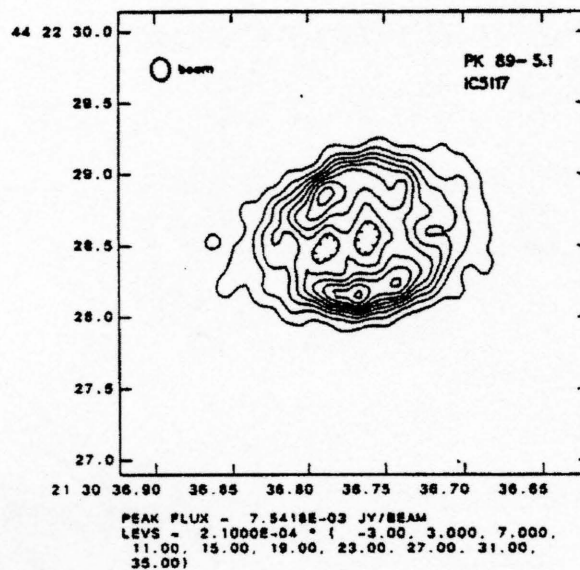


Figure 3.16 VLA 15 GHz radio continuum map of IC 5117 (Aaquist and Kwok 1991).

The temperature map suggests that the warmest dust lies within the equatorial plane (i.e. along the major axis). However, the lobes (rather than a central peak) suggest that there is a central cavity, which though unresolved in our images, contains relatively few hot dust grains. The position of the temperature lobes is complementary to the lobes of ionized gas traced in the radio continuum image of

Aaquist and Kwok (1991). We suggest that IC 5117 can also be modeled with the simple cylindrical shell model proposed for M 4–18, where the elliptical dust shell traces an enhancement of dust density in the equatorial plane, and the ionized gas lobes correspond to the lower density polar caps. However, for IC 5117, the inner radius of the dust shell is clearly unresolved.

The CO emission lines towards IC 5117 are strong and double-peaked (refer to Dayal and Bieging 1996). They suggest that the emission is either bipolar or resolved (in the 28'' 12-m J=2–1 HPBW). Since the dust shell is quite compact, however, we expect the molecular envelope also to be unresolved. Our CO J=2–1 map at 15'' spacing shows that the CO emission is extended towards the N and E and that the red- and blue-shifted line peaks have different relative intensities at different positions on the source. This structure may be real but given the pointing uncertainties ($\sim 5''$), needs to be confirmed with higher resolution imaging. Using equation 3.8 we estimate a total dust mass of $\sim 10^{-4} M_{\odot}$ at a distance of 3.0 kpc (Gathier et al. 1986). However, since IC 5117 has a mixed C/O chemistry, any assumptions about homogenous composition (and constant temperature) are clearly over-simplifications.

Our 11.7 μm image samples UIR and SiC emission (Fig 3.13) and the 12.5 μm image samples mostly continuum emission (with *some* contamination from the broad 11 μm feature). We construct a difference image (11.7–12.5 μm) after registering and convolving the 11.7 μm image to match the 12.5 μm image, and scaling it so that both images have the same (central) peak value. A difference image constructed in this way shows the *relative* excess (feature – continuum) over the surface of the nebula. (If, for example, the feature-to-continuum ratio is constant over the surface of the nebula, this difference image would be of zero

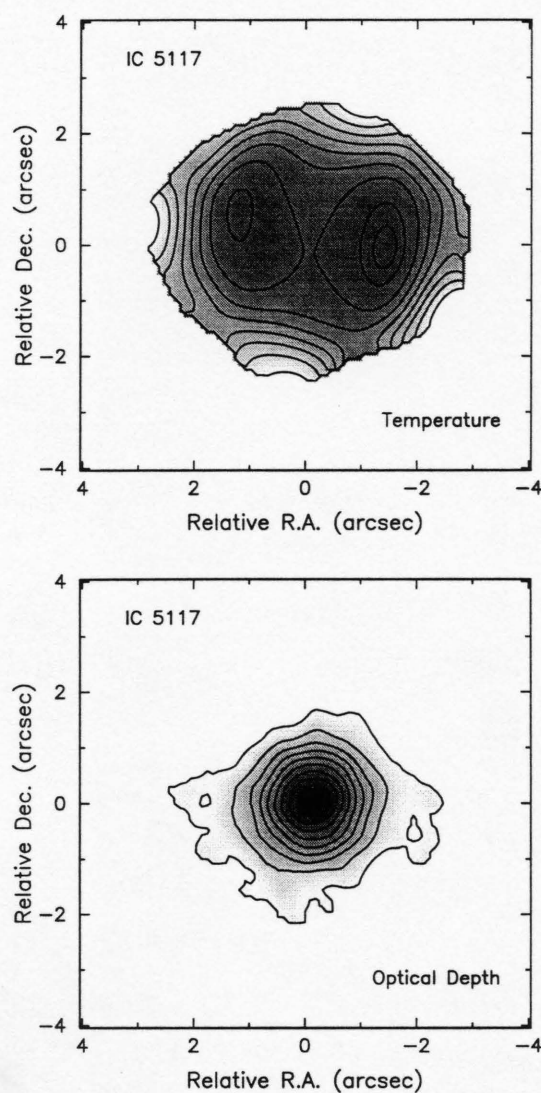


Figure 3.17 *Top*: Temperature Map of IC 5117 derived from the 8.8 μm and 11.7 μm images. The contour levels go from 190 K to 225 K in steps of 5 K. *Bottom*: Optical Depth map at 11.7 μm . The optical depth contours are 10% of the peak, which is 0.0035.

brightness all over). Dark areas in these images correspond to regions where the feature to continuum ratio is larger, relative to this ratio at map center.

The dark areas in Figure 3.18 (top), indicate regions where the proportion of UIR and/or SiC emitters relative to the dust continuum is largest. The peaks are displaced about $1''$ N-S from the nebula center; their positions agree rather closely with the bipolar peaks in the radio continuum map (Figure 3.16). This correlation is not surprising, as we would expect the excitation of PAH molecules to be enhanced in regions where UV extinction is lower. A similar difference map ($17.8\mu\text{m} - 20.6\mu\text{m}$) which isolates the silicate emission in IC 5117 (Fig 3.18 bottom) illustrates that the silicates-to-continuum difference peaks at radius of $\sim 1.7''$, and lies further out than the UIR/dust peak emission.

Evidence for changing chemistry? – In 1986, Willems and De Jong (1986) presented IRAS Low Resolution Spectra (LRS) of a number of carbon stars which appeared to show evidence for oxygen-rich grains (silicates) in their mid-IR spectra. They proposed that these stars were undergoing a transition from an oxygen-rich to carbon-rich chemistry. De Jong (1989) pointed out that the production of carbon is enhanced during helium shell thermal pulses, and the carbon rich material can be transported to the photosphere via convection. In this scenario a star which starts out being oxygen rich (just like the interstellar medium) becomes carbon rich as it evolves on the AGB. If the evolutionary scenario proposed by De Jong (1989) is responsible for a mixed population of grains, we would expect evidence for stratification i.e. the carbon rich grains would be located closer in to the star than the “fossil” silicate dust shell. Zhang and Kwok (1990) found that a number of young PNe, including IC 5117, show evidence for a mixed carbon-oxygen chemistry, i.e. their mid-IR spectra show both unidentified infrared

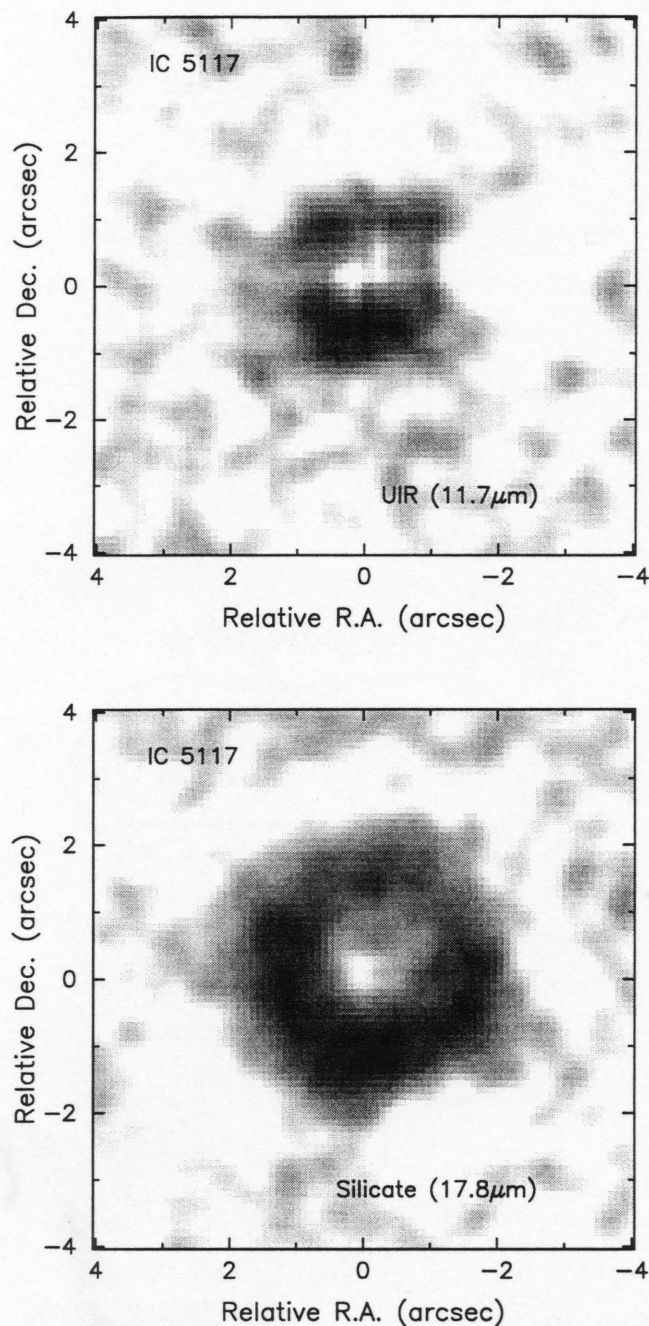


Figure 3.18 (*Top*): IC 5117 difference image ($11.7\mu\text{m} - 12.5\mu\text{m}$) showing the UIR emission over the continuum relative to the map center. Darker regions correspond to areas of higher UIR emission relative to continuum emission. (*Bottom*): IC 5117 difference image ($17.8\mu\text{m} - 20.6\mu\text{m}$) showing the silicate emission over the continuum relative to the map center. Darker regions correspond to areas of higher silicate emission relative to continuum emission.

(UIR) features as well as silicate features. Our difference images (Figure 3.18) show clear evidence for the stratification of carbon-rich and oxygen-rich dust grains. The carbon-rich (UIR and SiC) grains appear to peak (relative to the continuum emitters) at a significantly smaller radius than the silicate grains. The spatial difference between the two grain populations ($\sim 0.5\text{--}1''$) suggests that they trace mass loss episodes separated temporally, by $\sim 400\text{--}800$ yrs, based on a distance of 3 kpc and a CO expansion velocity of 17 km s^{-1} . However, if the expansion velocities closer to the dust photosphere (where the outflow is accelerated) are larger than those observed in CO, this evolutionary timescale of chemical transition may be significantly shorter.

3.6.4. OH 231.8+4.2

Images and analysis

OH 231.8+4.2 (which is also called the Rotten Egg Nebula because of a large abundance of sulphur compounds) is a well studied PPN with unusually high velocity molecular outflows ($100\text{--}300\text{ km s}^{-1}$; Alcolea, Bujarrabal and Sanchez Contreras (1996); Morris et al. 1987). Strong OH maser emission at 1667 MHz (Bowers and Morris 1984), the detection of sulphur bearing molecules such as SO_2 (Jackson and Nguyen-Q-Rieu 1988) and a very strong silicate feature at $9.8\mu\text{m}$ (Gillett and Soifer 1976; IRAS Science Team 1986) indicate an oxygen-rich circumstellar envelope. This object shows a well-defined common axial symmetry in the visible (Reipurth 1987), the near-IR (Kastner 1992; Kastner and Weintraub 1995) as well as at millimeter emission lines (Alcolea, Bujarrabal and Sanchez Contreras (1996)). Our mid-IR images show that the warm dust photosphere follows the near-IR and molecular emission axis of symmetry, though it is far less extended. In the $11.7\mu\text{m}$ image, the nebula extends about $4''\times 3.5''$. The major

axis is along PA $\sim 25^\circ$ and appears to be identical to the polar axis identified by the near-IR images. Both the $8.8\mu\text{m}$ and the $11.7\mu\text{m}$ images also show a bulge along the minor axis and appear to suggest an almost quadrupolar distribution. In sharp contrast to the $8.8\mu\text{m}$ and $11.7\mu\text{m}$ images, the $9.8\mu\text{m}$ image, which samples the deep silicate absorption feature, shows a significantly more extended emission region. We interpret this emission to arise from a cooler population of silicate grains which lie further out than the continuum emitters. The $18\mu\text{m}$ and $20.6\mu\text{m}$ images show more extended emission, with a nebular size of $\sim 5'' \times 3.5''$ (at the 10% contour level). Also, the emission here appears to extend further south along the axis of the nebula and the maps suggest that the southern lobe contains a larger fraction of cooler dust than the northern lobe.

Discussion

The $2.2\mu\text{m}$ images of Kastner (1992) show an elongated (NE–SW) bipolar source (Figure 3.23) and are consistent with a simple model where the axis of the nebula defines the polar axis of the PPN. In this model the observed near-IR emission lobes are created by scattered starlight, which escapes preferentially along the lower density polar axis. The axis of the nebula is inclined with respect to the plane of the sky by $\sim 40^\circ$ such that the northern lobe is closer to us, the southern lobe further away. CO J=2–1 line maps by Alcolea et al. (1996) show a strong velocity gradient and an emission region that extends $40\text{--}50''$ along the nebular axis. The kinematical structure shows that emission is concentrated into two clumps; the southern clump is redshifted about 200 km s^{-1} with respect to the center. The northern clump is blue-shifted, about 80 km s^{-1} relative to the center.

Our mid-IR images show that the warm dust photosphere does *not* lie

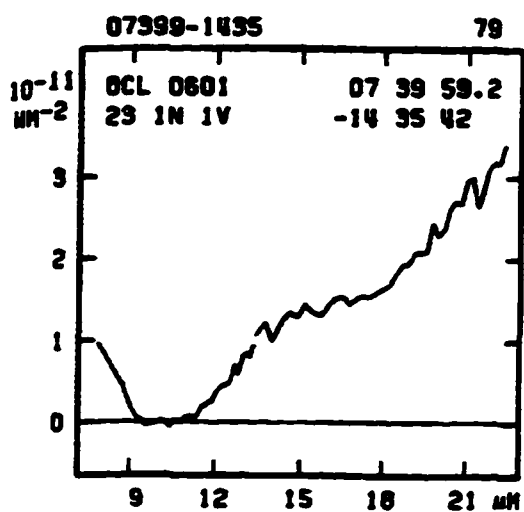


Figure 3.19 IRAS Low Resolution Spectra of OH 231.8 (IRAS 07399) – The spectrum is dominated by a strong silicate absorption feature from 9–12 μ m (IRAS Science Team 1986).

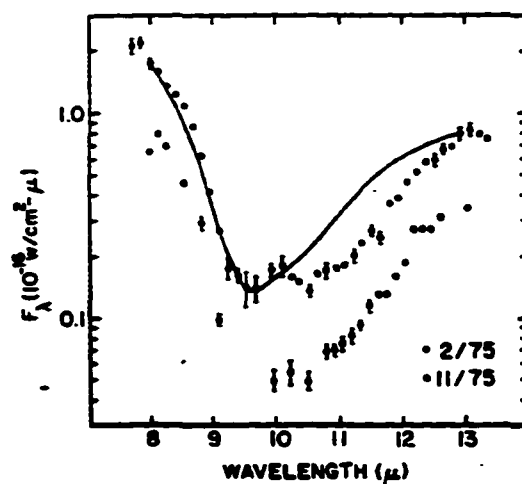


Figure 3.20 Ground-based 8–13 μ m spectra of OH 231.8, which also clearly shows the strong silicate absorption feature. (Gillett and Soifer 1976).

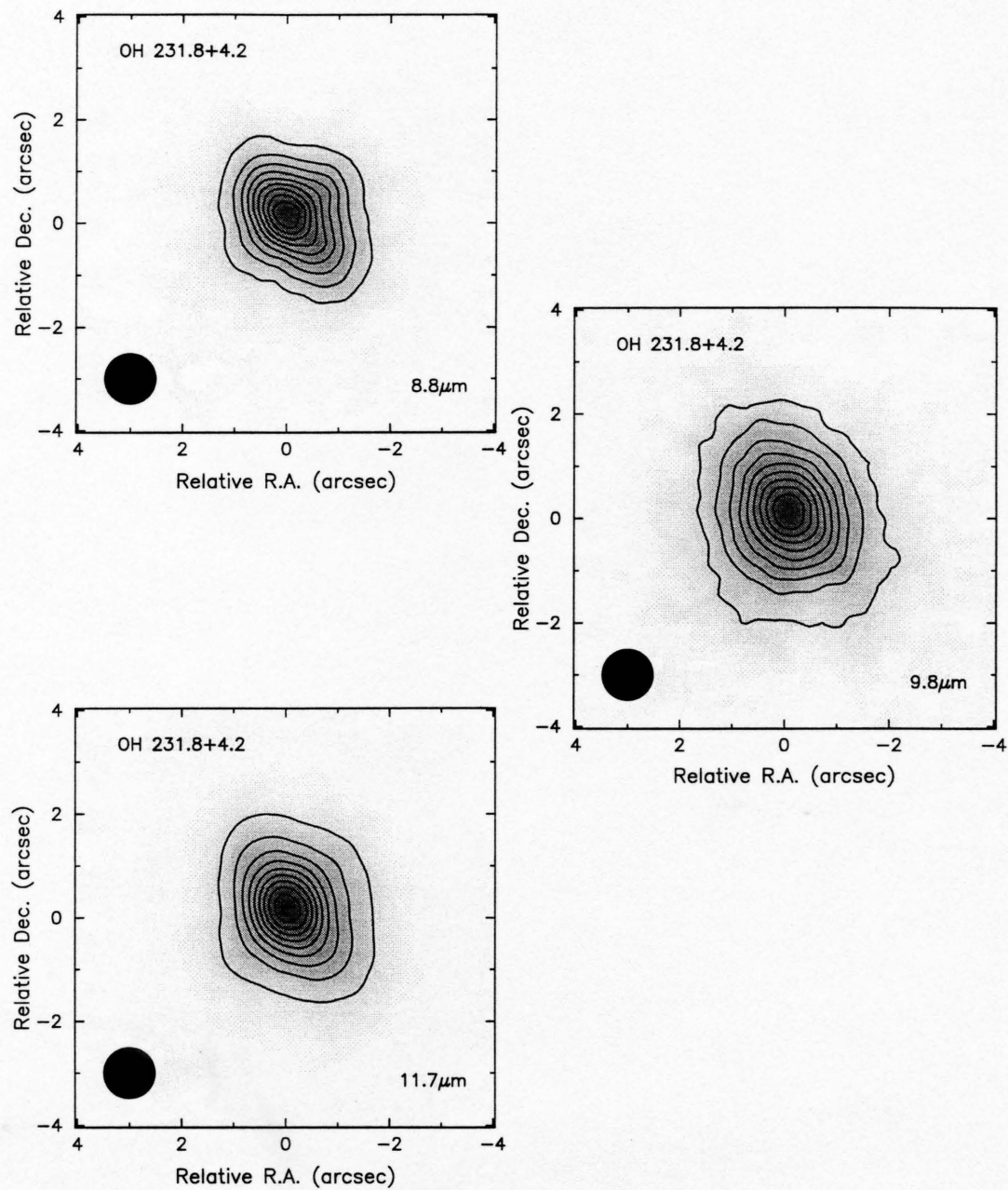


Figure 3.21 OH 231.8+4.2 MIRAC2 images taken at the IRTF. The contour interval is 10% of the peak. Peak emission is $8.0 \text{ Jy arcsec}^{-2}$ at $8.8\mu\text{m}$, $4.2 \text{ Jy arcsec}^{-2}$ at $9.8\mu\text{m}$ and $8.9 \text{ Jy arcsec}^{-2}$ at $11.7\mu\text{m}$.

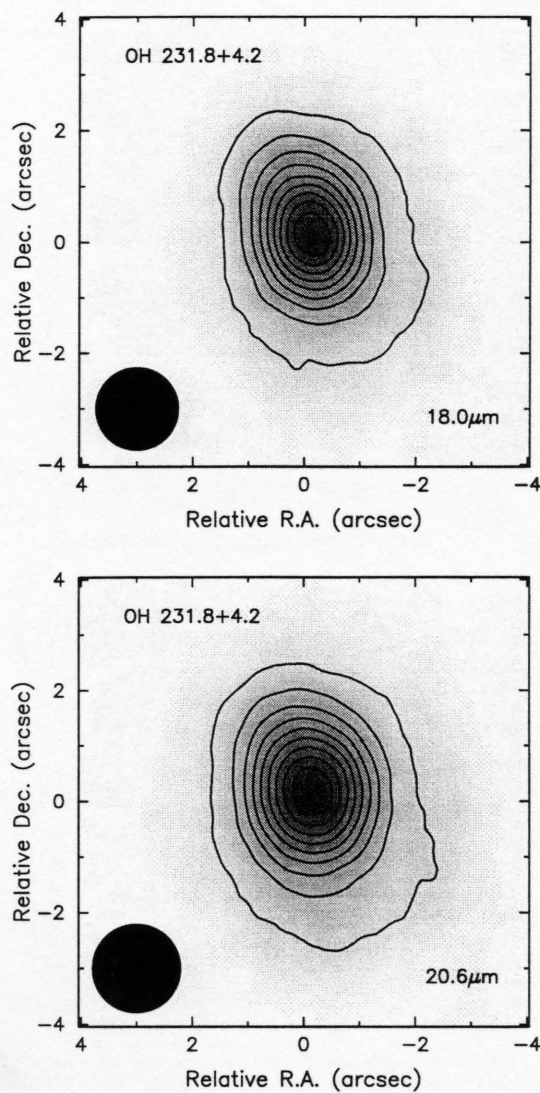


Figure 3.22 OH 231.8+4.2 18 μ m and 20.6 μ m MIRAC2 images taken at the IRTF. The contour interval is 10% of the peak which is 38 Jy arcsec⁻² at 18 μ m and 49 Jy arcsec⁻² at 20.6 μ m.

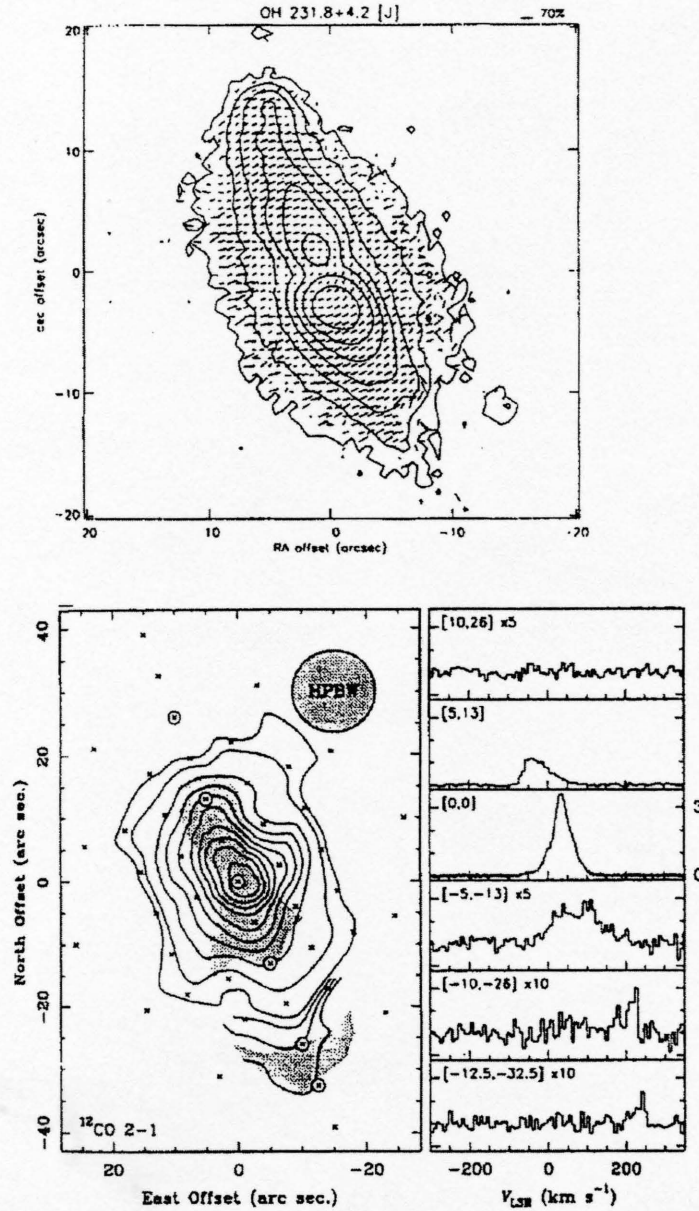


Figure 3.23 *Top*: $2.2\mu\text{m}$ polarization map of OH 231.8 superposed on the unpolarized $2.2\mu\text{m}$ image (Kastner and Weintraub 1995). *Bottom*: CO $J=2-1$ integrated intensity map and spectra of OH 231.8. The shaded region is a sketch of the optical source (Alcolea, Bujarrabal and Sanchez Contreras (1996)).

perpendicular to the polar axis as we may expect from the simple model proposed by Kastner (1992); instead it follows the near-IR axis of symmetry. The morphology seen in the mid-IR images is also similar to the CO maps of Alcolea et al. (1996): however the CO emission is considerably more extended. The similarity between the near-IR/optical/CO emission and our mid-IR images is not unique to OH 231.8. Hora et al. (1996) observed 3 well-studied PPNe, AFGL 618, AFGL 2688 (The Egg Nebula) and AFGL 915 (Red Rectangle) with the MIRAC camera. They found that in all cases the mid-IR extension was *along* the major axis defined by optical or near-IR images. Clearly, the mid-IR images appear to trace the material in bipolar outflows and not the emission from the equatorial (high density) dust shell that collimates the outflows.

Though the abundance of sulphur-bearing molecules as well as the large outflow velocities observed in OH 231.8 suggest that sulphur-producing chemical reactions are enhanced by the outflows, the dust in this nebula appears to be quite cold (≤ 100 K) as shown by detections of ice bands (Omont et al. 1990; Gillett and Soifer 1976). Furthermore there is no significant ionized gas in this nebula; Taylor and Morris (1993) detected no radio continuum emission associated with OH 231.8, and merely obtained an upper limit on the emission measure. We have constructed two color temperature maps (shown in Figure 3.24), using our $8.8\mu\text{m}$ and $18\mu\text{m}$ images and using the $11.7\mu\text{m}$ and $18\mu\text{m}$ images. Since both the $8.8\mu\text{m}$ and $11.7\mu\text{m}$ images are contaminated by feature emission (by different amounts), both maps yield different absolute color temperatures. However, they do show similar variations of temperature over the nebula. In both maps, the temperature peaks are bipolar and appear to lie along a NE-SW axis. The position of the peaks support our argument that the warmest dust (which biases the $10\mu\text{m}$ emission as well) lies along (or close to) the polar axis. It is worth noting that the temperature

map for AFGL 915 in Hora et al. (1996) is also not centrally peaked, but shows bright peaks displaced north and south of the center of the nebula.

Our $9.8\mu\text{m}$ image, which samples emission in the strong silicate absorption feature, indicates a somewhat more extended source morphology than either the $8.8\mu\text{m}$ or $11.7\mu\text{m}$ images. The $8.8\mu\text{m}$ and $11.7\mu\text{m}$ images lie near the wings of the silicate feature (refer to Figures 3.19, 3.20); hence although they are dominated by the continuum emission, they probably include contributions from the silicates as well. The mid-IR spectra together with $9.8\mu\text{m}$ image suggests that the silicate grains are cooler than the dust continuum, and also more extended spatially. The dust continuum emitters which are more concentrated towards the center of the nebula *may* be carbonaceous grains. Towards the center of the $9.8\mu\text{m}$ image we observe the dust photosphere through the cooler silicate grains. This is what produces the strong absorption feature. Towards the edges of the nebula we see the silicate grains in emission, hence the silicate image appears more extended than in the continuum. To verify the spatial distribution of the silicate grains we construct a scaled/difference map ($9.8\mu\text{m} - 11.7\mu\text{m}$) similar to those constructed for IC 5117 (Section 3.6.3). This map (Figure 3.25) shows that the difference between the silicate grains and continuum emitters peaks in two lobes, which are located symmetrically about the axis of symmetry defined by our mid-IR (and the near-IR/optical) images. There appear to be less silicate grains relative to the continuum along the polar regions suggesting that there may be destruction of silicate grains in the shocks associated with the strong bipolar outflows (e.g. Alcolea, Bujarrabal and Sanchez Contreras (1996)). Alternatively, the lack of silicates relative to continuum emitters at the center could also suggest that the continuum emitters may be carbon based, and that the difference map is indicative of a temporally changing chemistry, oxygen-rich to carbon-rich, as seen IC 5117.

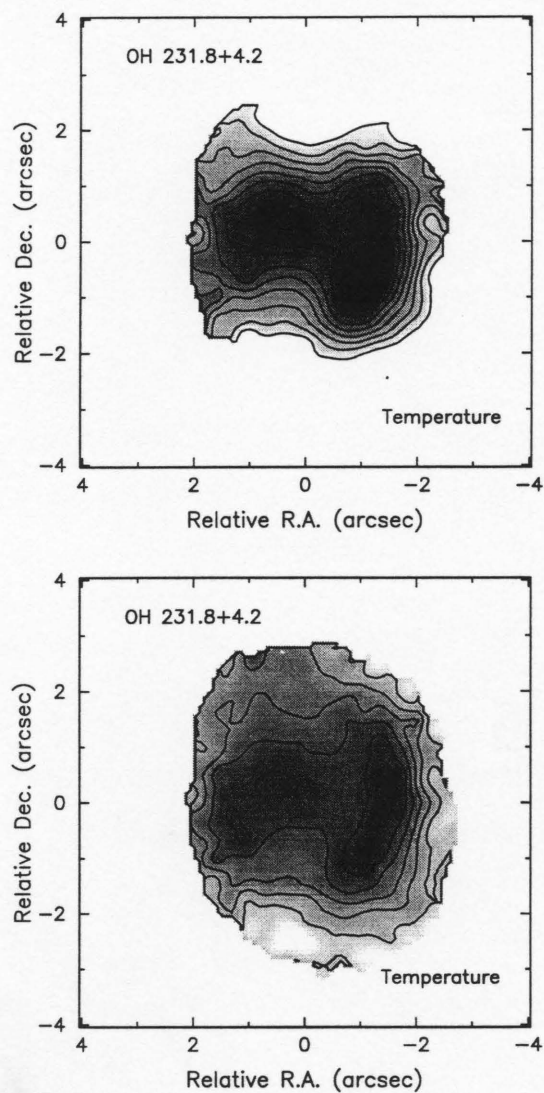


Figure 3.24 OH 231.8+4.2 color temperature maps. (*Top*): Color temperature map derived from $8.8\mu\text{m}$ and $18.0\mu\text{m}$ images. Contour levels are 170, 175, 180, 185, 190, 195, 200, 205, 210, 215 K. (*Bottom*): Color temperature map derived from $11.7\mu\text{m}$ and $18\mu\text{m}$ images. Contour levels are 115, 120, 125, 125, 130, 135, 140, 145 K.

The relative lack of cool silicate grains along the polar regions also supports our argument that the mid-IR morphology is biased by a few hot grains which lie along the poles.

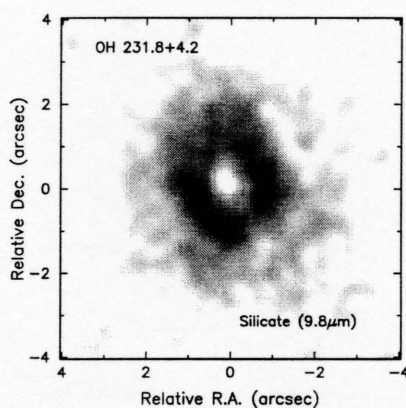


Figure 3.25 OH 231.8+4.2 difference image ($9.8\mu\text{m} - 11.7\mu\text{m}$), illustrating the relative silicate emission over the continuum emission. The dark regions correspond to higher silicate emission regions.

Table 3.2. Summary of MIRAC2 observations

Object	λ (μm)	$\Delta\lambda/\lambda$	Noise ($1-\sigma$) (Jy arcsec $^{-2}$)	Peak (Jy arcsec $^{-2}$)	Flux Density (Janskys)
IRAS 07134+1005 ^a	8.8	10%	0.02	0.9	7.8
	11.7	10%	0.03	3.0	30
	12.8	1.8%	0.08	3.3	33
	13.1	1.8%	0.08	3.6	35
	17.4	2.6%	1.00	7.5	50
	20.6	6.8%	0.14	14.6	145
IRAS 22272+5435 ^a	8.8	10%	0.01	8.2	27
	11.7	10%	0.02	26	102
	12.5	10%	0.02	26	105
	13.1	1.8%	0.07	24	98
	17.8	2.6%	0.13	31	163
	20.6	6.8%	0.08	40	234
IC 5117	8.8	10%	0.007	2.27	6.8
	11.7	10%	0.014	4.6	11.7
	12.5	10%	0.013	4.2	10.8
	17.8	2.6%	0.115	9.56	35
	20.6	6.8%	0.064	10.2	49
M 4-18	8.8	10%	0.02	0.32	1.9
	9.8	10%	0.07	0.40	2.1
	11.7	10%	0.016	0.61	4.8
	12.5	10%	0.025	0.67	5.0
OH 231.8+4.2	8.8	10%	0.042	8.13	26
	9.8	10%	0.047	4.23	20
	11.7	10%	0.03	8.85	30
	18.0	10%	0.37	38	197
	20.6	6.8%	0.45	49	280

^aA detailed study of IRAS 22272 and IRAS 07134 is presented in Appendix D.

Note. — Observations of IRAS 07134 were made at the 3.8-meter United Kingdom Infrared Telescope (UKIRT). All the other sources were observed at the 3-meter Infrared Telescope Facility (NASA/IRTF).

3.7. Summary of Chapter 3

We present mid-IR images (8–21 μ m) of 3 PPNe (IRAS 22272+5435, IRAS 07134+1005 and OH 231.8+4.2) and two young PNe (M 4–18 and IC 5117). All the sources show non-spherical structure. The bipolar morphologies of IRAS 07134+1005 and M 4–18 are clearly resolved. Our results show that the warm dust shells are not spherically symmetric, but can be modeled quite accurately as simple, axially symmetric (cylindrical) shells. In most objects there is evidence for an enhancement of density in the equatorial plane, i.e. the mass loss process is not spherically symmetric at spatial scales of 1''–2''.

1. We model the dust emission from IRAS 07134 and IRAS 22272 using simple axially symmetric shells. We calculate feature-to-continuum ratios in the 11–13 μ m feature and the 21 μ m feature, and estimate abundances for the feature carriers. The abundance and/or excitation of the carriers is found to vary significantly over the surface of the nebulae.

2. The mid-IR emission from M 4–18 shows a clear bipolar structure. Our mm-wave observations (and dust) indicate that this nebula is created by a low mass central star ($\leq 1M_{\odot}$).

3. The dust shell of IC 5117 is elliptical; the central core is unresolved but the temperature map is bipolar and suggests that the warmest dust lies in two lobes along the equatorial plane. Difference maps show that the 11.3 μ m UIR feature (relative to the continuum) peaks in bipolar N–S lobes (which closely match the radio continuum lobes), about 1'' from the center. The silicate emission at 18 μ m peaks (relative to the dust) in a shell of radius $\sim 2''$. These results are consistent with temporal changes in the circumstellar chemistry (oxygen-rich \rightarrow carbon-rich) in the last ~ 500 yr.

4. The mid-IR images of OH 231.8 are extended along the polar axis defined by the near-IR and optical images; the mid-IR emission is probably biased by hot dust in the polar regions. The $9.8\mu\text{m}$ silicate emission is more extended than the $8.8\mu\text{m}$ and $11.7\mu\text{m}$ continuum maps. A difference map between the silicate emission and the $11.7\mu\text{m}$ emission suggests that the ratio of silicate grains to continuum emitters peaks in bipolar lobes.

CHAPTER 4

CONCLUSIONS

4.1. Summary of Results

We have obtained high angular resolution ($0.7\text{--}1.5''$) mid-IR images of warm dust emission from two carbon-rich PPNe (IRAS 07134+1005 and IRAS 22272+5435), one oxygen-rich PPN (OH 231.8+4.2), and two young carbon-rich PNe (IC 5117 and M 4-18). All the sources are resolved and appear to show significant departures from spherical symmetry. IRAS 07134 and M 4-18 both show a resolved bipolar structure which suggests that both sources can be modeled using a similar axially symmetric geometry, where the warm dust is confined to the equatorial plane of the nebula, i.e. there is a large equator-to-pole density ratio. Both IRAS 07134 and M 4-18 appear to have asymmetric lobes, where one lobe is brighter than the other. Though our optically thin models do not explain the reasons for this asymmetry, we suggest that a slightly modified geometrical model, in which there is absorption of mid-IR emission radiation by cooler foreground dust, could produce lobes of unequal brightness. This hypothesis will be tested in future versions of our models. IRAS 22272 also shows a non-spherical structure, but we do not resolve

the emission into lobes here. We construct axially symmetric shell models for IRAS 07134 and IRAS 22272 and find that the morphologies of these sources can be well matched with cylindrical dust shells, though the model parameters of IRAS 22272 are not as well constrained as those of IRAS 07134. However to fit the mid-IR and far-IR spectra (our observations and IRAS measurements) our models require that 80–90% of the total dust mass be in the form of a cooler ($T \sim 90$ K) dust component, which has little emission at $10\mu\text{m}$ but contributes significantly to the far-IR and submillimeter fluxes. IRAS 07134, which has a more evolved central star than IRAS 22272, also has a larger fraction of cooler dust. This agrees with the general trend seen in PPNe and PNe, whereby the dust cools with expansion of the nebula. We construct difference maps which isolate feature emission, and measure the line-to-continuum ratios across the surface of the nebulae. We find that in IRAS 22272, the carriers of the unidentified $11\text{--}12\mu\text{m}$ feature are less abundant in the hottest regions of the nebulae; this observation is consistent with an evolutionary scenario where the feature carriers (possibly clusters of PAHs) are destroyed by the stellar radiation field.

Our analysis of the unidentified infrared (UIR) and/or SiC emission in IC 5117 shows that the carriers of the $11.3\mu\text{m}$ feature peak (relative to the continuum) in two lobes which appear to closely follow the lobes of ionized gas. The silicate emission at $18\mu\text{m}$ is more extended than the continuum emission. In our scaled difference image ($17.8\mu\text{m} - 20.6\mu\text{m}$), the peak of the excess silicate emission (over the continuum) forms a ring around the position of a similar image of the excess UIR emission. We believe that these results indicate a stratification of carbon- and oxygen-rich grains in the photosphere, and strongly suggest that IC 5117 has evolved from an O-rich phase to a C-rich phase over a period of ~ 500 yr.

A similar analysis of the silicate emission feature in OH 231.8 indicates that the silicate grains are more extended (by $\sim 1''$) than the continuum emitters, and that the abundance (or excitation) of silicates relative to the continuum emitters is greatest along two lobes which follow the axis of the nebula.

We have compared our images of M 4-18 and IC 5117 with radio continuum images and find that in both cases, the major axis of the dust shell lies orthogonal to the axis of the radio continuum lobes. For IC 5117, though the general shape of the warm dust resembles the radio continuum images, the dust appears to be somewhat more extended. In M 4-18, the radio continuum image suggests a slightly more spherical distribution of ionized gas than our images of warm dust imply. However for both these sources the comparisons show that while the warm dust defines the equatorial plane of the nebula, the ionized gas appears to peak along the polar regions. This is different from mid-IR images of OH 231.8 (and also AFGL 915 and AFGL 2688; Hora et al. 1996), which appear to *trace the dust along the polar axis*, as defined by optical/near-IR images. Our results suggest that in OH 231.8, AFGL 915 and AFGL 2688, which are all PPNe (or very young PNe), the polar regions may have a significant proportion of warm dust ($T \sim 200$ K) which radiates strongly at $10\mu\text{m}$, while in young PNe the polar cavities are more (warm) dust-free. Alternatively, it is possible that while most of the warm dust lies in a plane orthogonal to the polar axis, a small fraction of hot dust ($T \geq 500$ K) lies *along* the polar axis and dominates the mid-IR morphology. There is a bulge (or broadening) along the minor axis that is evident in the mid-IR maps of OH 231.8 (Figure 3.21). This bulge hints at a quadrupolar structure and suggests that even though the warm dust emission may be concentrated in the equatorial plane of the nebula, there is likely a smaller, hotter dust component along the polar regions. For these sources, we expect that as the fast, ionized wind turns on,

grains in the polar regions will be destroyed rapidly; thus, as these sources evolve, we might expect that the mid-IR emission will begin to trace the equatorial region (orthogonal to the optical/near-IR axis) rather than the polar regions, just as we see in M 4-18 and IC 5117.

It is interesting that M 4-18 has a bipolar dust shell (Figure 3.10), yet shows no sign of molecular gas. The presence of molecular gas is generally well-correlated with bipolar CSEs, and high mass progenitor stars (e.g. Kastner et al. 1996, Huggins 1995, Corradi and Schwarz 1995). Higher mass stars have higher mass loss rates and denser CSEs; therefore the CO molecules are better shielded from the stellar radiation. A deficiency of molecular gas could mean either that the star has a small (low mass) molecular envelope ($\leq 1 M_{\odot}$), or that it is in a relatively advanced state of evolution and the molecular material has already been destroyed by the stellar ionizing radiation. M 4-18 is clearly a low excitation PNe; therefore the observations favour the low-mass star argument. Thus, M 4-18 provides evidence that *low mass stars can also develop bipolar nebulae*. Dorfi and Höfner 1996 have generated models of winds from slowly rotating AGB stars. They find that even small deviations from spherical symmetry, introduced by slow rotations ($V \leq 5 \text{ km s}^{-1}$), can be amplified in the regions of dust formation. Their calculations show that a rotational velocity of $\leq 7 \text{ km s}^{-1}$ can produce an equator-to-pole mass loss ratio of ~ 25 .

From its galactic latitude ($b = 7.6^{\circ}$) and estimated distance of 3.5 kpc, we calculate a height (z) of 470 pc above the Galactic plane, for M 4-18. Such a large z also suggests that M 4-18 has evolved from a low-mass, late-type star, even though we keep in mind that the distance measurements are often uncertain by a factor of 2.

The interferometer images of CO emission in the oxygen-rich PPN source AFGL 2343 and the carbon-rich PPN IRAS 22272 suggest *some* deviations from spherical symmetry. The emission line towards the center of AFGL 2343 is remarkably asymmetric (Figure 2.12); the line profile suggests that the molecular outflow may be bipolar and clumpy, rather than spherically symmetric and smooth. We find no evidence of any spatial separation between the line peaks and conclude that if the outflow is indeed bipolar, then the axis of the outflow must be aligned closely with the line of sight to the nebula. We have modeled both IRAS 22272 and AFGL 2343 using a spherically symmetric radiative transfer code and find that our model fits appear to be quite good. From our models we determine that both IRAS 22272 and AFGL 2343 have “normal” CO abundances ($\sim 7 \times 10^{-4}$ w.r.t. H_2) but high rates of mass loss. AFGL 2343 has a molecular mass loss rate that is *an order of magnitude* higher than the observed mass loss in IRC+10216 ($2 \times 10^{-5} M_{\odot} \text{ yr}^{-1}$) or IRAS 22272 ($4.5 \times 10^{-5} M_{\odot} \text{ yr}^{-1}$). Our model results probe the mass loss rates in the extended molecular envelope; however closer into the dust photosphere (i.e. on shorter dynamical timescales) the mass loss rates may be significantly higher, 10^{-4} – $10^{-3} M_{\odot} \text{ yr}^{-1}$. We have constrained our models further by calculating the intensity of the J=2–1 transition as well, and comparing these results with other observations. The J=2–1 transition probes a smaller, inner region of the CSE than the J=1–0 line. If indeed our model assumptions of a single-power kinetic temperature law and/or the assumption of a constant mass loss rate were grossly incorrect, then we would expect to have difficulty fitting both (J=2–1, J=1–0) CO lines profiles (for example see Justtanont, Skinner and Tielens 1994). Since this is not the case, we believe that our spherically symmetric models of CSEs adequately reproduce the observed emission, at least to within our spatial resolution.

For IRAS 22272+5435 we calculated a total envelope mass of $\sim 0.4 M_{\odot}$ from

our optically thin models, assuming $M_{gas}/M_{dust} = 200$. If this is the amount of material ejected over a mass loss period of $\sim 10^4$ yr, we get an average $\dot{M} \approx 4 \times 10^{-5} M_{\odot} \text{ yr}^{-1}$, which is consistent with our model result.

4.2. Future Work

Many of the results presented in this study have benefited directly from the high spatial resolution afforded by millimeter interferometers (for molecular line observations), and the combination of 3–4 meter class telescopes and large format thermal-IR arrays. However as our images illustrate, even though the general morphology of compact PPNe and PNe is resolved at these resolutions ($\sim 1''$), we are unable to resolve the core for many sources which *probably* have a bipolar structure. For example, the evidence for bipolarity in unresolved-core images of IC 5117 or OH 231.8 comes from near-IR and/or VLA radio continuum maps, or even from our temperature maps, but the mid-IR images simply show elongated morphologies.

Since AGB stars, PPNe and young PNe are inherently compact objects, detailed information on their morphologies requires high spatial resolution. The future of imaging studies at optical and IR wavelengths clearly lies in space-based (diffraction limited) instruments such as the Hubble Space Telescope (WFPC2/NICMOS) or alternatively with ground based adaptive optics (AO) systems. The advent of routine imaging on 6–10 meter class telescopes (e.g. Keck, Gemini, MMT) will allow us to resolve compact sources, with sub-arcsecond resolution. We currently plan to use MIRAC2 at the Keck. We also have pending an HST/NICMOS proposal to image the hot dust, scattered starlight, and molecular gas in a variety of PPNe and young PNe. Space-based observations

in the thermal-IR (e.g. ISO, SIRTf) have unique advantages over ground-based studies in that: (1) they do not have to contend with the high background emission and (2) they do not have to worry about the atmospheric opacity. Preliminary results from ISO already show that the mid- and far-IR spectra of PPN and PN are rich with spectral lines (e.g. Beintema et al. 1996) that cannot be observed from the ground. The Infrared Array Camera (IRAC) on SIRTf, with a sensitivity of $\sim 10^{-5}$ Jy arcsec $^{-2}$ in a few minutes of integration time, will perhaps provide the most dramatic improvement in sensitivity ($\sim 10^3$), over current ground-based cameras like MIRAC2. We expect SIRTf to provide significant advances in any astronomical studies involving thermal-IR dust emission, including those that involve high resolution imaging of PPNe and PNe.

On the millimeter-wave front there is an urgent need to expand the capabilities of existing interferometers, to observe higher transitions of CO (and other molecules). Such observations ($J=2-1$, $J=3-2$) will not only provide better resolution than the $J=1-0$ line, but also allow us to map the inner, higher excitation regions of the nebulae which lie closer to the dust photosphere. However, the Millimeter Array (MMA) promises the single biggest boost to millimeter-wave interferometry, if it is approved and completed. The MMA would consist of 40 8-m diameter dishes with antenna separations of ~ 3 km (Brown 1994) and would provide sub-arcsecond ($\sim 0.1''$) resolution at 115 GHz. Such an instrument would easily resolve disks and/or bipolar outflows in PPNe and PNe whose presence is currently only inferred from kinematical information.

REFERENCES

- Aaquist, O. B., and Kwok, S. 1990, *A&AS*, 84, 229
- Aaquist, O. B., and Kwok, S. 1991, *ApJ*, 378, 599
- Aaquist, O. B., and Kwok, S. 1996, *ApJ*, 462, 813
- Aitken, D. K., and Roche, P. F. 1982, *MNRAS*, 200, 217
- Alcolea, J., Bujarrabal, V., and Sanchez Contreras, C. 1996, *A&A*, 312, 560
- Allamandola, L. J., Tielens, A. G. G. M., and Barker, J. R. 1989, *ApJS*, 71, 733
- Bachiller, R., Huggins, P. J., Cox, P., and Forveille, T. 1993, *A&A*, 267, 177
- Bachiller, R., Fuente, A., Bujarrabal, V., Colomer, F., Loup, C., Omont, A., and de Jong, T. 1997, *A&A*, 319, 235
- Bakker, E. J., Waters, L. B. F. M., Lamers, H. J. G. L. M., Trams, N. R., and Van der Wolf, F. L. A. 1996, *A&A*, 310, 893
- Balick, B. 1987, *AJ*, 94, 671
- Balick, B., Preston, H. L., and Icke, V. 1987, *AJ*, 94, 1641
- Bedijn, P. I. 1987, *A&A*, 186, 136
- Beintema, D. A. et al. 1996, *A&A*, 315, L369
- Bentley, A. F., Hackwell, J. A., Grasdalen, G. L. and Gehrz, R. D. 1984, *ApJ*, 278, 665
- Bieging, J. H., Chapman, B., and Welch, W. J. 1984, *ApJ*, 285, 656
- Bieging, J. H., Wilner, D., and Thronson, H. A. 1991, *ApJ*, 379, 271
-

- Bieging J. H., and Tafalla, M. 1993, AJ, 105, 576
- Bond, H. E., Ciardullo, R., Fullton, L. and Schaefer, K. 1996. in *IAU Symposium 180 Planetary Nebulae*, eds. H. Habing and H. Lamers. Kluwer Academic Publishers, in press
- Bowers, P. F., and Morris, M. 1984, ApJ, 276, 646
- Brown, R. L. 1994, in *Astronomy with Millimeter and Sub-millimeter Interferometry*, eds. M. Ishiguro and J. Welch, ASP Conference Series, Vol 59, 398
- Bujarrabal, V., Alcolea, J. and Planesas, P. 1992, A&A, 257, 701
- Buss, R. H., Jr., Cohen, M., Tielens, A. G. G. M., Werner, M. W., Bregman, J. D., Witteborn, F. C., Rank, D., and Sandford, S. A. 1990, ApJ, 365, L23
- Cabrit, S. and Bertout, C. 1986, ApJ, 307, 313
- Chan, J., and Kwok, S. 1990, A&A, 237, 354
- Cherchneff, I., Glassgold, A. E., and Mamon, G. A. 1993, ApJ, 410, 188
- Cherchneff, I., and Barker, J. R. 1992, ApJ, 394, 703
- Chevalier, R. 1994, in *Circumstellar Media in the Late Stages of Stellar Evolution*, Eds. R. Clegg, I. Stevens and W. Meikle (University Press:Cambridge), 308
- Clark, B. G., 1988, in *Synthesis Imaging in Radio Astronomy: A collection of lectures from the Third NRAO Synthesis Imaging Summer School*, eds. R. Perley, F. Schwab and A. Bridle, ASP Conference Series Vol 6
- Cohen, M., Walker, R. G., Barlow, M. J., and Deacon, J. R. 1992, AJ, 104, 1650
-

- Cohen, M., Witteborn, F. C., Walker, R. G., Bregman, J. D., and Wooden, D. H.
1995, AJ, 110, 275
- Corradi, R. L. M., and Schwarz, H. E. 1995, A&A, 293, 871
- Dayal, A., and Bieging, J. H. 1995, ApJ, 439, 996
- Dayal, A., and Bieging, J. H. 1993, ApJ, 407, L37
- Dayal, A., and Bieging, J. H. 1996, ApJ, 472, 703
- Dayal, A., Hoffmann, W. F., Bieging, J. H., Hora, J. L., Deutsch, L. K., and Fazio,
G. G. 1997, submitted to the ApJ
- De Jong, T., 1989, in *From Miras to Planetary Nebulae: Which Path for Stellar
Evolution*, Eds. M. Mennessier and A. Omont, Editions Frontieres, 289
- Dorfi, E. A., and Höfner, S. 1996, A&A, 313, 605
- Draine, B. T., and Lee, H. M. 1984, ApJ, 285, 89
- Duley, W. W., and Williams, D. A. 1981, MNRAS, 196, 269
- Dyck, H. M., Zuckerman, B., Howell, R. R., and Beckwith, S. 1987, PASP, 99, 99
- Forveille, T., and Huggins, P. J. 1991, A&A, 248, 599
- Garcia-Lario, P., Manchado, A., Sahu, K. C., and Pottasch, S. R. 1993, A&A, 267,
L11
- Garay, G., Gathier, R., and Rodriguez, L. F. 1989, A&A, 215, 101
- Gathier, R., Pottasch, S. R., and Goss, W. M. 1986, A&A, 157, 191
- Gillett, F. C., and Soifer, B. T. 1976, ApJ, 207, 780
-

- Glassgold, A. E. 1996, *ARA&A*, 34, 241
- Goebel, J. H. 1993, *A&A*, 278, 226
- Goldreich, P., and Scoville, N. Z. 1976, *ApJ*, 205, 144
- Goodrich, R. W. and Dahari, O. 1985, *ApJ*, 289, 342
- Guélin, M., Lucas, R., and Cernicharo, J. 1993, *A&A*, 280, L19
- Guillois, O., Nenner, I., Papoular, R., and Reynaud, C. 1996, *ApJ*, 464, 810
- Habing, H. 1996, *A&A Rev.*, 7, 97
- Han, Z., Podsiadlowski, P., and Eggleton, P. P. 1995, *MNRAS*, 272, 800
- Hawkins, G. W., Skinner, C. J., Meixner, M. M., Jernigan, J. G., Arens, J. F.,
Keto, E., and Graham, J. R. 1995, *ApJ*, 452, 314
- Hildebrand, R. H. 1983, *QJRAS*, 24, 267
- Hoffmann, W. F., Fazio, G. G., Shivanandan, K., Hora, J. L., and Deutsch, L. K.
1993, *Proc. SPIE*, 1946, 449
- Hora, J. L., Deutsch, L. K., Hoffmann, W. F., and Fazio, G. G. 1996, *AJ*, 112, 2064
- Hora, J. L., Deutsch, L. K., Hoffmann, W. F., and Fazio, G. G. 1993, *ApJ*, 413, 304
- Hora, J. L. 1991, PhD. Thesis, University of Arizona
- Hora, J. L., Deutsch, L. K., Hoffmann, W. F., and Fazio, G. G. 1990, *ApJ*, 353, 549
- Howe, D. A., and Millar, T. J. 1990, *MNRAS*, 244, 444
- Hrivnak, B. J., Kwok, S., and Volk, K. 1989, *ApJ*, 346, 265
-

- Hrivnak, B. J., and Kwok, S. 1991, *ApJ*, 371, 631
- Hrivnak, B. J. 1995, *ApJ*, 438, 341
- Huggins, P. J., and Glassgold, A. E. 1982, *ApJ*, 252, 201
- Huggins, P. J., and Healy, A. P. 1989, *ApJ*, 346, 201
- Huggins, P. J. 1995, *Ap&SS*, 224, 281
- Huggins, P. J., Bachiller, R., Cox, P., and Forveille, T. 1996, *A&A*, 315, 284
- Iben, I. 1990, in *Evolution of Stars: The Photospheric Abundance Connection*, eds. G. Michaud and A. Tutukov, (Kluwer:Dordrecht), 257
- Iben, I., and Renzini, A. 1983, *ARA&A*, 21, 271
- Iben, I. Jr., and Livio, M. 1993, *PASP*, 105, 1373
- Icke, V., Balick, B., and Frank, A. 1992, *A&A*, 253, 224
- IRAS Science Team, 1986, *A&AS*, 65, 607
- Jackson, J. M., and Nguyen-Q-Rieu, 1988, *ApJ*, 335, L83
- Jamiet, P. A., Danchi, W. C., Sandell, G., and Sutton, E. C. 1992, *ApJ*, 400, 535
- Jura, M., Balm, S. P., and Kahane, C. 1995, *ApJ*, 453, 721
- Jura, M. 1996, *ApJ*, 472, 806
- Jura, M., Turner, J., and Balm, S. P. 1997, *ApJ*, 474, 741
- Justtanont, K., Skinner, C. J., and Tielens, A. G. G. M. 1994, *ApJ*, 435, 852.
- Justtanont, K., Barlow, M. J., Skinner, C. J., Roche, P. F., Aitken, D. K., and Smith, C. H. 1996, *A&A*, 309, 612
-

- Kahn, F., and West, K. A. 1985, MNRAS, 212, 837
- Kastner, J. H. 1992, ApJ, 398, 552
- Kastner, J. H., and Weintraub, D. A. 1994, ApJ, 434, 719
- Kastner, J. H., and Weintraub, D. A., 1995, AJ, 109, 1211
- Kastner, J. H., Weintraub, D. A., Gatley, I., Merrill, K. M., and Probst, R. G.
1996, ApJ, 462, 777
- Knapp, G. R., Phillips, T. G., Leighton, R. B., Lo, K. Y., Wannier, P. G., Wootten,
H. A., and Huggins, P. J. 1982, ApJ, 252, 616
- Knapp, G. 1986, ApJ, 311, 731
- Krisciunas et al. 1987, PASP, 99, 887
- Kutner, M. L., and Ulich, B. L. 1981, ApJ, 250, 341
- Kwok, S., Purton, C. R., and Fitzgerald, P. M. 1978, ApJ, 219, L125
- Kwok, S., Volk, K. M., and Hrivnak, B. J. 1989, ApJ, 345, L51
- Kwok, S. 1993, ARA&A, 31, 63
- Lafon, J. -P. J., and Berruyer, N. 1991, A&A Rev., 2, 249
- Lafont, S., Lucas, R., and Omont, A. 1982, A&A, 106, 201
- Latter, W. B., Hora, J. L., Kelly, D. M., Deutsch, L. K. and Maloney, P. R. 1993,
AJ, 106, 260
- Latter, W. B., Kelly, D. M., Hora, J. L. and Deutsch, L. K. 1995, ApJS, 100, 159
- Léger, A., and Puget, J. L. 1984, A&A, 137, L5
-

- Léger, A., d'Hendecourt, L., and Défourneau, D. 1989, A&A, 216, 148
- Likkel, L., Omont, A., Morris, M., and Forveille, T., 1987, A&A, 173, L11
- Likkel, L. 1989, ApJ, 344, 350
- Likkel, L., Forveille, T., Omont, A., and Morris, M. 1991, A&A, 246, 153
- Lindqvist, M., Nyman, L. -Å., and Winnberg, A. 1988, A&A, 205, L15
- Livio, M. 1994, in *Circumstellar Media in the Late Stages of Stellar Evolution*. Eds. R. Clegg, I. Stevens and W. Meikle (University Press:Cambridge), 35
- Lucas, R. 1993, in *Astronomy with Millimeter and Sub-millimeter Interferometry*, eds. M. Ishiguro and J. Welch ASP Conference Series, Vol 59, 135
- Mamon, G. A., Glassgold, A. E., and Huggins, P. J. 1988, ApJ, 328, 797
- Masson, C. R. 1990, ApJ, 346, 243
- Mathis, J. 1990, ARA&A, 28, 37
- Meixner, M. 1993, PhD. Thesis, University of California at Berkeley.
- Meixner, M., Skinner, C. J., Graham, J. R., Keto, E., Jernigan, J. G., and Arens, J. F. 1997, ApJ, 482, 897
- Millar, T. J. and Herbst, E. 1994, A&A, 288, 561
- Montou, C., Léger, A., and d'Hendecourt, L. 1996, A&A, 310, 297
- Morris, M. 1975, ApJ, 197, 603
- Morris, M., and Jura, M. 1983, ApJ, 264, 546
- Morris, M., Guilloteau, S., Lucas, R., and Omont, A. 1987, ApJ, 321, 888
-

- Nejad, L., and Millar, T. 1987, *A&A*, 183, 279
- Noel, R. A. 1992, in *Infrared Detectors and Focal Plane Arrays II*, eds. E. L. Dereniak & R. E. Sampson, *Proc. SPIE* 1685, 250
- Omont, A., Moseley, S. H., Forveille, T., Glaccum, W. J., Harvey, P. M., Likkell, L., Loewenstein, R. F., and Lisse, C. M. 1990, *ApJ*, 355, L27
- Omont, A., Loup, C., Forveille, T., Lintel Hekkert, P. te, Habing, H., and Sivagnanam, P. 1993, *A&A*, 267, 515
- Omont, A., Lucas, R., Morris, M., and Guilloteau, S. 1993, *A&A*, 267, 490
- Omont, A., Moseley, S. H., Cox, P., Glaccum, W., Casey, S., Forveille, T., Chan, K-W., Szczerba, R., Loewenstein, R. F., Harvey, P. M., and Kwok, S. 1995, *ApJ*, 454, 819
- Parthasarathy, M., and Pottasch, S. R. 1986, *A&A*, 154, L16
- Pasquali, A., and Perinotto, M. 1993, *A&A*, 280, 581
- Puget, J. L., and Léger, A. 1989, *ARA&A*, 27, 161
- Rasio, F. A., and Livio, M. 1996, *ApJ*, 471, 366
- Reimers, D. 1975, in *Problems in Stellar Atmospheres and Envelopes*, eds. D. Bascheck, W. H. Kegel and G. Traving, (Springer:Berlin), p. 229
- Reipurth, B. 1987, *Nature*, 327, 787
- Rieke, G. H. 1994, in *Detection of Light from the Ultraviolet to the Submillimeter*, (University Press:Cambridge)
- Sabbadin, F. 1986, *A&AS*, 65, 301
-

- Sahai, R., and Trauger, J. 1996, BAAS, (189th meeting of the AAS), in press
- Sault, R. J., Teuben, P. J., and Wright, M. C. H. 1995, in *Astronomical Data Analysis Software and Systems IV*, eds. R. Shaw, H. Payne and J. Hayes. ASP Conference Series, 77, 433
- Savage, B. D., and Mathis, J. S. 1979, ARA&A, 17, 73
- Schönberner, D. 1989, in *From Miras to Planetary Nebulae: Which Path for Stellar Evolution*, Eds. M. Mennessier and A. Omont, Editions Frontieres, 355
- Schutte, W. A., Tielens, A. G. G. M., and Allamandola, L. J., 1993, ApJ, 415, 397
- Scoville, N. et al. 1993, PASP, 105, 1482
- Sedlmayr, E. 1989, in *From Miras to Planetary Nebulae: Which Path for Stellar Evolution*, Eds. M. Mennessier and A. Omont, Editions Frontieres, 179
- Shibata, K. M., Tamura, S., Deguchi, S., Hirano, N., Kameya, O., and Kasuga, T. 1989, ApJ, 345, L55
- Skinner, C. J., Meixner, M. M., Hawkins, G. W., Keto, E., Jernigan, J. G., and Arens, J. F. 1994, ApJ, 423, L135
- Skinner, C. J., Griffin, I. P., and Cohen, R. J. 1989, in *From Miras to Planetary Nebulae: Which Path for Stellar Evolution*, Eds. M. Mennessier and A. Omont, Editions Frontieres, 335
- Soker, N., and Livio, M. 1989, ApJ, 339, 268
- Sourisseau, C., Coddens, G., and Papoular, R. 1992, A&A, 254, L1
- Spitzer, L. 1978, *Physical Processes in the Interstellar Medium*, (NY:Wiley)
-

- Surendiranath, R., and Kameswara Rao, N. 1995, MNRAS, 275, 685
- Szmulowicz, F., and Madarsz, F. L. 1987, Journal of Applied Physics, 62, 2533
- Takano, S., Saito, S., and Tsuji, T. 1992, PASJ, 44, 469
- Taylor, G. B., and Morris, M. 1993, ApJ, 409, 720
- Thompson, A. R., Moran, J. M., and Swenson, G. W., Jr. 1986, in *Interferometry and Synthesis in Radio Astronomy*, John Wiley & Sons, New York
- Tielens, A. G. G. M. and Allamandola, L. J. 1987, in *Interstellar Processes*, eds. D. Hollenbach and H. Thronson, Jr. (Dordrecht:Reidel), 397
- Traub, W. A., and Stier, M. T. 1976, Applied Optics, Vol 15 No. 2, 364
- Truong-Bach, Graham, D., and Nguyen-Q-Rieu 1996, A&A, 312, 565
- Tsuji, T. 1973, A&A, 23, 411
- Van der Veen, W. E. C. J., Trams, N. R., and Waters, L. B. F. M. 1993, A&A, 269, 231
- van der Veen, W. E. C. J., Habing, H. J., and Geballe, T. R. 1989, A&A, 226, 108
- Vassiliadis, E. and Wood, P. R. 1993, ApJ, 413, 641
- Vogel, S. N., Wright, M. C. H., Plambeck, R. L., and Welch, W. J. 1984, ApJ, 283, 655
- Volk, K., and Kwok, S. 1988, ApJ, 331, 435
- Walmsley, C. M., Chini, R., Kreysa, E., Steppe, H., Forveille, T., and Omont, A. 1991, A&A, 248, 555
-

- Whittet, D. C. B. 1993, in *Dust and Chemistry in Astronomy*, eds. T. J. Millar and D. A. Williams, (Institute of Physics Publishing : London). 9
- Willems, F. J. and De Jong, T. 1986, ApJ, 309, L39
- Woodsworth, A. W., Kwok, S., and Chan, S. J. 1990, A&A, 228, 503
- Začs, L., Klochkova, V. G., and Panchuk, V. E. 1995, MNRAS. 275, 764
- Začs, L., Klochkova, V. G., Panchuk, V. E., and Spēlmanis, R. 1996, MNRAS, 282, 1171
- Zavagno, A., Cox, P., and Baluteau, J. -P. 1992, A&A, 259, 241
- Zhang, C. Y., and Kwok, S. 1990
- Zuckerman, B., and Aller, J. H. 1986, ApJ, 301, 772
- Zuckerman, B., Dyck, H. M., and Claussen, M. J. 1986, ApJ, 304, 401
- Zuckerman, B., and Dyck, H. M. 1986, ApJ, 311, 345
- Zuckerman, B., and Gatley, I. 1988, ApJ, 324, 501